

**Surface properties of silver-gold alloys
– a quantum mechanics-based approach
combining theory and experiment**

**Vom Promotionsausschuss der
Technischen Universität Hamburg**

zur Erlangung des akademischen Grades

Doktor-Ingenieurin (Dr.-Ing.)

genehmigte Dissertation

von
Sandra Hoppe

aus
Höxter

2020

Betreuer: Prof. Dr. Stefan Müller

Erstgutachter: Prof. Dr. rer. nat. Stefan Müller

Zweitgutachter: Prof. Dr.-Ing. Robert Meißner

Tag der mündlichen Prüfung: 24. Juli 2020

DOI 10.15480/882.2939

ORCID iD 0000-0001-6635-1901

Abstract

A prominent tool in computational materials modeling is density functional theory (DFT), which allows one to calculate macroscopic material properties from the atomic scale and based solely upon physical principles. The cluster expansion (CE), a statistical physics-based method, makes it possible to match those properties to atomic arrangements, and thus identify the most favorable structures within the whole configuration space.

Local properties at the material's surface are also influenced by the atomic arrangement within a small number of surface layers. A typical example is surface segregation, where the atomic order at the surface differs from that of the bulk because of a difference in chemical potential. In this thesis, CE fits were performed to predict the most favorable surface configurations and analyze the segregation behavior at flat and stepped Ag-Au surfaces. The Ag-Au system was of particular interest here, since small amounts of silver that remain after the fabrication process may explain the origin of the high catalytic reactivity of the sponge-like nanoporous gold.

Interestingly, gold segregation to the topmost layer of the adsorbate-free Ag-Au surfaces was obtained in this work, whereas numerous experimental and theoretical studies from the past report silver surface segregation. It is shown here by means of an analysis of Bader charges and the partial density of states that gold is stabilized in the topmost layer by a charge transfer from silver to the more electronegative gold. In a next step, it is revealed that for

oxygen-covered Ag-Au surfaces, silver impurities are drawn to the surface layer. The special case of an infinite oxide chain on the stepped Au(321) surface with Ag impurities is characterized by an analysis of the bonding characters and the electronic surface structure.

Furthermore, the electromechanical coupling behavior at the Ag-Au (111) surface is studied. This can be evaluated by calculating the response of the electronic work function to in-plane strain. The resulting coupling parameter was then expanded in a CE fit to examine the influence of the silver surface concentration and the atomic arrangement at the surface. In summary, a strong influence of the surface layer composition on the coupling parameter is found for the Ag-Au alloy surface.

Finally, the atomic structure composition of the adsorbate-free Ag-Au (111) surface is characterized experimentally via low-energy electron diffraction (LEED). The LEED structure analysis indicates good agreement with the calculated segregation behavior, namely slight gold enrichment in the surface layer and silver enrichment in the subsurface layer. The obtained silver concentrations in the first layers match those of a ground state obtained in the surface CE.

The first-principles results from this thesis combined with the cluster expansion technique help to shed new light on surface phenomena in the Ag-Au alloy. Such data are very difficult to acquire experimentally, as they take into consideration hundreds of thousands of atomic configurations. Here, we verify our calculations by performing a LEED structure analysis, which yields fairly good agreement with the first principles data.

Abstract (deutsch)

Mittels Dichtefunktionaltheorie (DFT), einer beliebten Methode der Materialmodellierung, lassen sich makroskopische Materialeigenschaften auf atomarer Ebene berechnen. Mithilfe der Clusterentwicklung (CE), einer Methode basierend auf statistischer Physik, können diese Eigenschaften atomaren Anordnungen zugeordnet werden. Dadurch können die energetisch günstigsten Strukturen im gesamten Konfigurationsraum identifiziert werden.

Lokale Materialeigenschaften an der Oberfläche werden unter anderem durch die atomare Anordnung in einigen wenigen Oberflächenschichten beeinflusst. Ein typisches Beispiel dafür ist Oberflächensegregation, bei der die atomare Anordnung an der Oberfläche sich von der im Bulk unterscheidet. In dieser Arbeit wurden mittels CE-Fits energetisch günstige Oberflächenstrukturen und das Segregationsverhalten an flachen und gestuften Ag-Au-Oberflächen analysiert. Das Ag-Au-System wurde dafür ausgewählt, da nach dem Herstellungsprozess des schwammartigen nanoporösen Goldes kleine Mengen Silber im Material verbleiben, die dessen hohe katalytische Reaktivität erklären könnten.

Interessanterweise wurde in dieser Arbeit Gold-Segregation zur Oberflächenschicht gefunden, während zahlreiche experimentelle und theoretische Studien von früher Silber-Segregation an die Oberfläche berichten. Es wird hier durch eine Bader-Analyse und die partielle Zustandsdichte gezeigt, dass Gold in der Oberflächenschicht durch einen Ladungstransfer von Silber zum stärker elek-

tronegativen Gold stabilisiert wird. In einem nächsten Schritt wird gezeigt, dass im Falle von Sauerstoff-bedeckten Ag-Au-Oberflächen Silber-Atome an die Oberfläche gezogen werden. Hier wird der Spezialfall einer gestuften Au(321)-Oberfläche mit Ag-Fremdatomen bezüglich des Bindungscharakters und der elektronischen Struktur an der Oberfläche untersucht.

Außerdem wird die elektromechanische Kopplung an der Ag-Au (111)-Oberfläche untersucht. Dies kann durch die Abhängigkeit der Austrittsarbeit von einer Flächen-Dehnung berechnet werden. Die resultierenden Kopplungsparameter wurden dann mittels CE gefittet, um den Einfluss der Silber-Oberflächenkonzentration und der atomaren Anordnung zu untersuchen. Zusammenfassend wurde ein starker Einfluss der Oberflächenlagenzusammensetzung auf den Kopplungsparameter von Ag-Au-Legierungen gefunden.

Abschließend wurde die atomare Zusammensetzung der Adsorbat-freien Ag-Au (111)-Oberfläche mittels Low-Energy Electron Diffraction (LEED) untersucht. Die LEED-Struktur-Analyse weist sehr gute Übereinstimmung mit dem berechneten Segregationsverhalten auf, nämlich geringe Gold-Anreicherung in der Oberflächenlage und Silber-Anreicherung in der zweiten Lage.

Die ab initio Ergebnisse dieser Arbeit kombiniert mit der Clusterentwicklungsmethode erlauben die Aufklärung von Oberflächenphänomenen an der Ag-Au-Oberfläche. Solche Daten lassen sich nur schwierig experimentell erhalten, da tausende atomare Anordnungen in Erwägung gezogen werden müssen. Hier werden die Berechnungen durch eine LEED-Struktur-Analyse verifiziert, die gute Übereinstimmung mit den theoretischen Ergebnissen zeigt.

Contents

Abstract	i
Abstract (deutsch)	iii
Contents	v
List of Figures	ix
List of Tables	xiii
1. Introduction	1
2. Nanoporous gold - a novel catalyst material	5
2.1. History and applications	5
2.2. Why does npAu exhibit high catalytic activity?	9
2.3. Motivation for the present work	13
3. Surface segregation in Ag-Au in the literature	15
3.1. Basic concepts in surface segregation	15
3.2. Surface segregation in Ag-Au	17
4. Methodology	25
4.1. Density Functional theory	25
4.1.1. The Schrödinger equation	25

4.1.2.	Historic and physical background of density functional theory	28
4.1.3.	The exchange-correlation functional	32
4.1.4.	Important concepts for the practical implementation of DFT	35
4.1.5.	Initial geometry and geometry optimization	38
4.2.	Cluster expansion	42
4.2.1.	Theoretical background	43
4.2.2.	Genetic algorithm	46
4.2.3.	Ground-state search	48
4.2.4.	Surface cluster expansions	51
4.2.5.	Monte Carlo simulations	51
4.3.	Low-energy electron diffraction (LEED)	53
4.3.1.	Theoretical background	53
4.3.2.	Tensor LEED	60
5.	Surface segregation at Ag-Au surfaces	65
5.1.	Bulk reference	65
5.1.1.	Pure elements	66
5.1.2.	Ag-Au alloy	67
5.2.	Selection of suitable surface orientations	68
5.3.	Surfaces of pure elements	71
5.3.1.	Surface energy	71
5.3.2.	Surface relaxation	73
5.4.	Results on surface segregation	74
5.4.1.	Clean Ag-Au (111) surface	75
5.4.2.	O-covered Ag-Au (111) surface	84
5.4.3.	Influence of configurational entropy on the surface segregation at Ag-Au (111) surfaces	90
5.4.4.	Clean Ag-Au (321) surface	93
5.4.5.	O-covered Ag-Au (321) surface	100
6.	Electromechanical coupling at the Ag-Au (111) surface	115
6.1.	Theoretical background	115
6.2.	Computational details	120
6.3.	Results on electromechanical coupling	125

7. LEED structure analysis and results	131
8. Summary	141
Appendix A. VASP input parameters	145
Appendix B. Segregation results for pure Au bulk and pure Ag bulk	149
Appendix C. LEED intensity vs. energy spectra	153
Acknowledgements	155
Bibliography	156
Curriculum vitae	175

List of Figures

1.1. Fields of expertise and research methods in the Research Group FOR 2213	2
2.1. Morphology of nanoporous gold	7
2.2. Catalytic cycle for self- and cross-coupling of primary alcohols	10
4.1. Perdew's "Jacob's ladder" of exchange-correlation functionals	34
4.2. Illustration of pseudopotential approach	39
4.3. DFT flow chart	41
4.4. Illustration of the surface slab	42
4.5. Illustration of the CE figures	43
4.6. Degeneracies of three clusters on the fcc lattice	44
4.7. Illustration of the genetic algorithm	48
4.8. Illustration of the outer loop of the CE	49
4.9. Illustration of a ground-state diagram	50
4.10. Layer-dependent effective interactions close to the surface . .	51
4.11. Experimental LEED setup	55
4.12. Construction of the Ewald sphere	57
4.13. Angular dependence of the scattering factor	59
4.14. Flow chart of the structure analysis process in TensErLEED .	62
5.1. Ag-Au ground-state diagram	69

5.2. Illustration of the Au (111) and (321) surfaces	70
5.3. Top and side view of the Ag-Au surface slab with L1 ₂ bulk structure	76
5.4. Surface stability diagram for the clean Ag-Au (111) surface with L1 ₂ bulk structure	78
5.5. Surface segregation profile for the clean Ag-Au (111) surface .	80
5.6. Charge density difference plots for a Au-terminated and a Ag-terminated surface	84
5.7. Side and top views of the Ag-Au (111) surface with adsorbed atomic O on the fcc hollow site	86
5.8. Surface stability diagram for the Ag-Au (111) surface with L1 ₂ bulk structure adsorbed O	89
5.9. Surface segregation profile for the Ag-Au (111) surface with adsorbed oxygen and L1 ₂ bulk structure	90
5.10. Partial density of states (DOS) of two selected ground states	91
5.11. Atomic configuration within the surface layers as obtained from the MC simulation	93
5.12. Silver concentration within the four surface layers for the adsorbate-free and the oxygen-covered Ag-Au (111) surface with L1 ₂ bulk	94
5.13. Top view and side view of the adsorbate-free Au (321) surface	96
5.14. Surface stability diagram for the clean Au (321) surface with Ag impurities	97
5.15. Charge density difference plots for selected ground states . .	99
5.16. Side view and top view of the Au (321) surface slab with infinite oxide chain	101
5.17. Reconstruction of the adsorbate-free Au (321) surface upon formation of the infinite oxide chain	102
5.18. Surface stability diagram for the Au (321) surface with Ag impurities and an infinite oxide chain	104
5.19. Ag layer concentration in the surface and subsurface layer for the ground states at all Ag surface concentrations	106
5.20. Partial density of states (DOS) of four selected configurations	109
5.21. Electronic localization function (ELF) for two surface configurations	110
5.22. Partial DOS and COHP analysis for two selected structures .	112
5.23. AIMD simulation of Ag diffusion to an oxide chain fragment .	114

6.1.	Illustration of electron spill-out	117
6.2.	Illustration of the strain applied to the surface slabs	122
6.3.	Equilibrium layer distances determined from deformed bulk cells subjected to in-plane strain	123
6.4.	Illustration of the plane-averaged local electrostatic potential of a surface slab and the necessary quantities to determine its work function	124
6.5.	Surface stability diagram with electromagnetic coupling coefficients for pure in-plane strain included	126
6.6.	Surface stability diagram with electromagnetic coupling coefficients for in-plane strain with transverse contraction and surface relaxation	128
7.1.	Simulation of STM pictures at a bias voltage of -500 meV for the $L1_2$ ordered structure (a) and the obtained ground state at a silver surface concentration of 25% (b). The color coding indicates the tip height.	132
7.2.	$I(E)$ spectra of the (10) beam for different annealing temperatures of the sample	133
7.3.	LEED pattern	134
7.4.	Comparison between experimental and theoretical $I(E)$ curves for eight investigated beams	136
7.5.	Pendry R-factor R_P for different silver concentrations in the surface layer (a) and the subsurface layer (b). The black line indicates the sum of the best-fit Pendry R-factor $P_{R,min}$ and the variation of the latter. The error in silver concentration can then be determined from the intersection points of the two curves.	137
7.6.	Comparison of the silver and gold content (depicted in silver and gold, respectively) within the four surface layers for the two sets of LEED data	138
7.7.	Absolute layer distances as obtained from the two LEED fits in comparison to DFT results	139
B.1.	Surface stability diagram for the clean Ag-Au (111) surface with pure Ag bulk	150

B.2. Surface stability diagram for the clean Ag-Au (111) surface with pure Au bulk	151
C.1. Comparison between experimental and theoretical $I(E)$ curves for eight investigated beams	154

List of Tables

5.1.	Equilibrium lattice parameters for the pure elements	67
5.2.	Surface energies of the Ag and Au (111) surfaces	72
5.3.	Surface relaxation for the Au (111) and (321) surfaces	74
5.4.	Number of DFT input structures and cross-validation score for the clean Ag-Au (111) surfaces	77
5.5.	Bader charges of the surface and subsurface layer of the clean Ag-Au (111) surface with L1 ₂ bulk structure	83
5.6.	Adsorption energy for chemisorbed oxygen on the fcc hollow site at the pure Au (111) surface and Ag-Au (111) surfaces	87
5.7.	Surface formation enthalpies of selected structures at constant Ag surface concentration for PBE and PBE+D3	105
6.1.	Work function ϕ of the unstrained Ag-Au (111) surface	123
6.2.	Response of the work function, the surface dipole potential and the bulk Fermi energy to strain	129
7.1.	Best fit results for the vibrational amplitudes for both LEED data sets	139
A.1.	VASP input parameters for static calculations	146
A.2.	VASP input parameters for dipole corrections and relaxation	147

Introduction

Ever since mankind started to build things and use tools, exploring the available materials and developing new ones has been a crucial issue. For more than three million years, during the Stone Age, stone tools were employed as cutting tools or weapons by early human species. The fabrication of bronze by smelting copper and alloying it with tin and other metals led to harder and more durable tools and technological development in the Bronze Age, which was followed by the discovery of iron and steel production in the Iron Age. Nowadays, new materials are still necessary to meet the requirements for lightweight applications in the automotive and aircraft industry, or to fulfill a certain functionality in nanotechnology and semiconductor technology.

Throughout history, however, the discovery and development of new materials has usually been accompanied by a tedious trial and error process demanding high experimental effort, without being able to produce and test all possible parameter combinations. Modern materials research therefore focuses on systematical and thorough approaches to obtain properties tailored for a specific application. These properties may include the macroscopic structure, the atomic configuration and the chemical composition.

In this context, the Research Group 2213, "Nanoporous Gold: A prototype for a rational design of catalysts" (short: NaGoact), unites different fields of expertise to develop, understand and optimize a relatively new and promising material for catalytic applications: nanoporous gold (npAu). By combining experimental and theoretical know-how, a detailed study compris-

ing the fabrication process, a structural characterization and the application of the sponge-like material in gas phase and liquid phase catalysis was carried out (see Figure 1.1). Within this framework, the present work employs modern materials simulation methods to investigate the configuration and properties of silver-gold surfaces. The motivation behind this lies in understanding the high catalytic activity of nanoporous gold, which may originate in the presence of residual silver atoms in the surface left from the fabrication process.

Preparation	<ul style="list-style-type: none">▪ dealloying of the Ag-Au alloy<ul style="list-style-type: none">➢ free corrosion➢ electrochemical corrosion▪ tailoring of properties
Characterization	<ul style="list-style-type: none">▪ x-ray photoelectron spectroscopy (XPS)▪ temperature programmed desorption (TPD)▪ transmission electron microscopy (TEM)▪ scanning tunneling microscopy (STM)
Experiment	<ul style="list-style-type: none">▪ gas phase catalysis▪ liquid phase catalysis▪ electrocatalysis▪ strain effects on catalysis
Simulation	<ul style="list-style-type: none">▪ density functional theory (DFT)▪ cluster expansion (CE)▪ molecular dynamics (MD)

Figure 1.1.: Fields of expertise and research methods combined in the Research Group FOR 2213 (NaGoCat).

Modern simulation techniques like the ones presented in this work have gained popularity with the progressive development of high performance computers. These are able to cope with the computational effort posed by complex physical problems at different scales. For many phenomena, it is necessary to analyze a material at the atomic scale to be able to make reliable predictions. This may be efficiently assessed with density functional theory (DFT), which has been widely applied throughout computational physics and chemistry since its introduction by Hohenberg and Kohn in the 1960s [1,

2]. Today, properties of interest like the energy, elastic constants or surface characteristics may be calculated for a few hundred atoms with good accuracy and in user-friendly program codes like the Vienna ab initio simulation package (VASP) [3–5]. Still, the creation of a suitable model for the problem at hand and the choice of the right parameters remains a challenging task for the user. While a numerical result may be obtained easily, it requires a carefully chosen input and a thorough analysis of the outcome to perform reliable calculations. Consequently, the DFT input geometries, important parameters and employed functionals will be presented in detail here.

The present work is organized as follows. First, nanoporous gold as catalyst material is described and discussed regarding its fabrication, properties and potential use in gas phase and liquid catalysis (Chapter 2). Resulting from this, the motivation to investigate the surface segregation behavior at Ag-Au surfaces is obtained and presented to the reader. In the following Chapter 3, a detailed review of experimental and theoretical studies from the literature dealing with segregation at Ag-Au surfaces is given. A thorough description of the methodology employed in the present work, including density functional theory, the cluster expansion (CE) method and low-energy electron diffraction (LEED), is provided in Chapter 4. Chapter 5 presents the results obtained for the segregation behavior at selected Ag-Au surfaces. To carry out a comprehensive investigation, both flat and stepped surfaces without and with adsorbed oxygen were considered. In a further step, the electromechanical coupling behavior at a flat Ag-Au surface is discussed in Chapter 6 to analyze the influence of mechanical strain on the surface reactivity. Finally, the present results on segregation are verified experimentally by a low-energy electron diffraction (LEED) structure analysis in Chapter 7. This thesis then concludes with a brief summary in Chapter 8.

Nanoporous gold - a novel catalyst material

“But what’s worth more than gold?”

"Practically everything. You, for example. Gold is heavy. Your weight in gold is not very much gold at all. Aren't you worth more than that?"

- Terry Pratchett, *Making Money*

2.1. History and applications

Gold is generally considered the noblest of all metals [6] and has fascinated mankind since ancient times [7]. The reason for this fascination certainly lies in gold’s unique properties, combined with its low concentration of gold in the earth crust of only 2-5 parts per billion (ppb, weight), making it a rare and precious material. It is speculated that most of these small amounts reached the earth in meteorites about 3.9 million years ago [8]. Even though gold had been discovered before the handling of other metals and alloys, such as iron and bronze [9], its application remained restricted to monetary assets and jewelry for a long time [10, 11]. Still nowadays, these two areas claim about 90% of the world’s gold production, while only 10% goes into technological applications like electrically conductive coatings for electronics or optical coatings [7, 9, 12].

For a long time, gold was considered chemically inert and therefore unattractive for catalysis. By definition, a catalyst is a substance that causes or

accelerates a chemical reaction and is both a reactant and product of the reaction. More specifically, it provides an alternative reaction mechanism and energy pathway that is characterized by a lower activation barrier than the original one. This leads to a higher turnover at lower temperatures, increasing the effectiveness of a chemical process. A catalytic cycle usually begins with the chemisorption of one or multiple reactants on the catalyst surface, followed by its desorption and the formation of the desired (intermediate) product. In order to achieve a high turnover, the educt may not remain on the catalyst surface for too long, as that would slow down the whole reaction. Consequently, too strong bonding of the educts with the catalyst surface is unfavorable [7]. The enthalpy of adsorption, which describes the amount of heat evolved when an adsorbate gets adsorbed on a surface, should therefore have an intermediate value. For transition metals, the enthalpy of adsorption generally decreases when increasing the atomic number, it is to say, moving from left to right in the periodic table. As a matter of fact, typically very active metal catalysts are located in groups 8-10 of the transition metals, such as platinum, palladium or cobalt [13]. Gold, even though it is next to platinum in the periodic table, represents an exception to this rule. As discussed by Hammer and Nørskov [14], typical adsorbates like oxygen, carbon and hydrogen will bond weakly with flat gold surfaces.

Interestingly, gold becomes chemically and thereby catalytically active when nanostructured. First experiments on olefin hydrogenation by Bond et al. [15, 16] in the 1970s were followed by studies on olefin chlorination and CO oxidation by Hutchings [17] and Haruta et al. [18] in the 1980s. The former groups and successive research revealed the promising catalytic potential of fine Au nanoparticles dispersed on a suitable oxidic support, such as TiO_2 , CeO_2 or Fe_2O_3 [18–22]. Compared to conventional catalyst materials, gold offers several advantages. On the one hand, gold catalysts are very selective, meaning they do not attack C–C single or C–H bonds in organic compounds [23]. On the other hand, they provide high catalytic activity for certain reactions, such as partial oxidations [24], and they even stay active at low temperatures [11, 24, 25]. In contrast to that, typical catalyst materials, such as platinum or palladium, drastically decrease in catalytic activity at room temperature, which makes them unsuitable for applications like automotive emission control [25]. Finally, using gold for catalysis is also reasonable for economic reasons, as it is considerably less expensive than

platinum or rhodium [11]. All these characteristics mark gold as an attractive material for the "green chemical industry", which has emerged from the need for sustainability in the production of commodity chemicals [26, 27]. Green chemistry aims at establishing efficient chemical processing under ambient pressure and temperature relying on abundant resources, without the need of toxic materials.

Several recent studies on bimetallic Ag-Au nanoparticles supported on aluminosilicate [26, 28–30] or titania [31] for low temperature CO oxidation report higher catalytic activity as compared to monometallic Au nanoparticle catalysts [32, 33]. As pure silver nanoparticles are not highly catalytically active at low temperatures [26], this beneficial effect of additional Ag can probably be ascribed to a synergy between the two metals [26, 34]. However, the support material may interact with the nanoparticles and thereby influence the catalytic performance, or even affect the catalytic reaction directly [35, 36]. This makes it difficult to understand the reaction mechanisms of such catalysts in detail [37]. Furthermore, sintering of the nanoparticles under reaction conditions may impair the catalytic activity and result in bad long-term stability [24, 38].

In view of these problems, the catalytic community has developed a growing interest in the sponge-like nanoporous gold (npAu) within the last decades. Its microstructure is characterized by a highly porous network of interconnected Au nano ligaments with a diameter that can range between about 10 nm to 1 μm [39] (see Figure 2.1. At an atomic level, the curved surface consists of close-packed terraces which are separated by atomic steps [37].

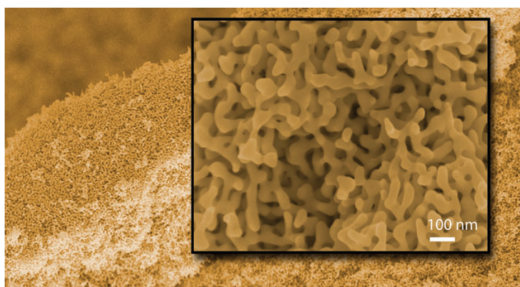


Figure 2.1.: SEM micrograph showing the sponge-like morphology with open porosity of nanoporous gold [7].

Due to the very high specific surface area of 10-15 m^2/g and a large surface

to volume ratio, the properties of npAu are mainly governed by its surface. In theory, the open porosity in npAu makes the entire surface accessible to reactants, but the mass transport may be hindered by a small ligament and pore size. Therefore, it is necessary to find a compromise between small ligaments for a large fraction of surface atoms and larger pores for a good mass transport [40]. At the same time, the homogeneous bulk nanoporous structure provides good electrical and thermal conductivity, making it an ideal material for electrocatalytic applications [11]. Furthermore, the noble and predictable surface chemistry of gold leads to a minimal sticking of undesired adsorbates [7].

To a certain extent, the morphology and the properties of npAu may be tailored during its synthesis. The fine ligament structure is generated by a wet chemical corrosion process of an Au parent alloy containing one or several less noble metals, typically Ag [41, 42], Cu [43] or Al [44, 45]. The Ag-Au system, however, offers certain advantages over alternative parent alloys. Due to the formation of a homogeneous solid solution across all compositions, it can be dealloyed to a residual Ag concentration of < 1 at.% [9, 24]. In addition, the two elements have similar mechanical properties and corrosion techniques exist with a high selectivity for Ag [46].

During this so-called dealloying, the less noble element (Ag, in this case) is removed from the parent alloy and the atoms of the nobler element (Au) are redistributed on the crystal lattice by surface diffusion [47]. This diffusion is accompanied by a coarsening of the ligaments and pores. Basically, there exist two types of dealloying: the free corrosion in an electrolyte, typically done in nitric acid, and the corrosion in an electrochemical cell under the application of an anodic potential, for example in perchloric acid [7, 46]. Essentially, two parameters determine the success of the dealloying. First, a critical potential marks the onset of corrosion [48–50]. Second, only parent alloys containing less than 45 at.% of Au can be dealloyed, as for higher concentrations, the less noble element is passivated by Au. This concentration threshold is called parting limit [51, 52]. While the fabrication and structure is very similar to Raney type metal catalysts [8, 53, 54], such as Raney nickel and Raney copper, each grain in npAu retains its original orientation after dealloying, resulting in a porous single crystal.

As a matter of fact, already the Incan civilization applied the dealloying process to etch and subsequently polish the surface of copper-rich gold-copper

alloys some hundred years ago. This ancient technique of creating the illusion of shiny bulk gold is called depletion gilding or "mise en couleur" and it was also used in Europe by medieval artisans [41, 42, 55]. The emerging porous morphology or the mechanisms of the process, however, remained unknown for a long time. In the 1960s, Pickering and Swann [56, 57] studied the corrosion of gold alloys and obtained the first transmission electron micrographs showing the porous structure of npAu. Almost 20 years later, Forty and Durkin [42, 58] analyzed and explained the dealloying mechanism of a Ag-Au alloy in nitric acid and presented transmission electron micrographs of the monolithic npAu structure.

The catalytic potential of npAu for CO oxidation was first investigated experimentally in the 2000s by Zielasek et al. [38] and Xu et al. [59]. Both authors reported high catalytic activity at low temperatures below 0 °C. From then on, numerous groups have investigated the application of npAu for CO oxidation (see, for example, Ref. [40, 43, 60–63]). Their observations made npAu catalysts an attractive candidate to solve the cold start-up period of the automotive converter and for exhaust gas treatment, where the harmful CO is oxidized to the nonhazardous CO₂ [11, 25].

Another industrially relevant application of npAu catalysts is the selective oxidation of alcohols, in particular methanol [24, 64, 65]. The latter represents the starting point for a large variety of useful bulk chemicals, such as formamide and methyl formate, which is an intermediate for the production of formic acid. The worldwide production of those two products is in the range of several hundred thousand tons per year [66, 67]. The catalytic cycle for the self- and cross-coupling of primary alcohols on the npAu surface can be seen in Figure 2.2.

2.2. Why does npAu exhibit high catalytic activity?

The origin of the high catalytic activity of npAu is still an ongoing debate. One potential reason is speculated to be the abundance of low-coordinated Au atoms on the rough surface of the npAu curved ligaments [59, 61, 68]. It is hypothesized that these atoms may interact more strongly with molecules due to their altered electronic structure, especially a local upshift and narrowing of the *d*-band [68, 69]. As a consequence, the reaction barriers at these active centers would be decreased, as compared to the flat Au (111) surface [70–72].

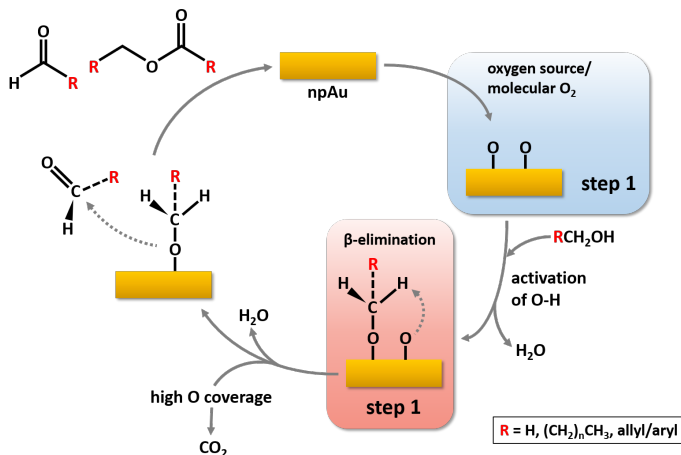


Figure 2.2.: Schematic representation of the catalytic cycle for the self- and cross-coupling of primary alcohols on the npAu surface (adapted from Ref. [64]).

Indeed, transmission electron microscopy (TEM) analysis [37] of the curved npAu surface revealed low- and high-index surfaces with a high density of atomic steps and kinks, which would correspond to nanoparticles of 3-5 nm size. In TEM and SEM pictures of the npAu surface, the high number of low-coordinated Au atoms was observed to remain nearly constant even during catalytic reaction and coarsening of the ligaments, resulting in a reduced surface curvature [69]. Following this line of thought, the a stepped Au surface should theoretically be more active towards O_2 dissociation and CO adsorption than the flat Au (111) surface. In an experimental study, however, Kim et al. [73] found that even under elevated pressure and temperature, O_2 was not activated and dissociated on the Au (211) surface.

Interestingly, recent experimental results indicate that extremely pure npAu did not dissociate O_2 and showed very low catalytic activity toward CO oxidation [34, 74, 75]. This observation suggests that the presence of residual impurities remaining in the npAu after the dealloying plays a decisive role in the dissociation of O_2 and thus in its catalytic performance [34, 36, 38, 43, 60, 61]. As mentioned above, the favorable characteristics of a bimetallic catalyst were already observed for supported nanoparticles [26, 32, 33].

This hypothesis about the importance of residual impurities in the npAu

was corroborated by several experimental studies. Noteworthy, npAu samples used for CO oxidation by Wittstock et al. [40] had to be activated, meaning exposed to ambient air for some time, before catalytic activity could be detected. This activation may have induced segregation of Ag impurities to the surface or it may have changed the chemical state of Ag surface atoms, thereby promoting O₂ dissociation. Wang et al. [36, 76] found a linear correlation between the oxygen storage capacity of npAu leached from an Ag-Au alloy and the residual Ag surface content. They also stated that structural parameters, such as the total surface area or the ligament size have only a minor effect on catalytic activity. Shortly afterwards, Déronzier et al. [34] synthesized npAu from Ag-Au alloys with controlled amounts of residual Ag and analyzed its catalytic activity. They were able to show that already very small silver concentrations of 2-6 at.% sufficed to increase the activity toward CO oxidation by several orders of magnitude as compared to extremely pure npAu.

Nevertheless, the effect of residual Ag is not only beneficial, but it can be detrimental as well. Experiments conducted by Wittstock et al. [12] showed that the selectivity for the partial oxidation product methyl formate decreased for a higher residual Ag content, up to a point where no methyl formate was formed at all. This is due to the fact that as the activity in CO oxidation and thereby the yield of CO₂ increases, the oxidation of methanol is hindered [77]. The literature also suggests an undesired build-up of inactive intermediates at the catalyst surface, such as surface bonded formate [24]. Hence, the ideal amount of residual Ag depends on the type of reaction and controls the oxidation power of the catalyst material [24, 75, 77].

To fully understand the influence that residual Ag has on the catalytic properties of npAu, it is crucial to elucidate where the Ag atoms are located in the gold ligaments. X-ray photoelectron spectroscopy (XPS) measurements [34, 40] suggest strong Ag enrichment within the npAu ligament surface. The authors explain this by the lower surface tension of silver and mention that the presence of adsorbed oxygen should also promote Ag surface segregation, as its oxygen affinity is larger than that of Au [34].

Two very recent studies aimed at displaying and analyzing the Ag distribution within npAu samples. In transmission electron micrographs (TEM), Krekeler et al. [78] found discrete, three-dimensional regions of Ag within a Au matrix for the as-delloyed state. An annealing treatment resulted in

coarsening of the npAu ligaments and a homogeneous Ag distribution. Based on kinetic Monte Carlo simulations, they concluded that these Ag regions were a relics from the master alloy which had not yet been reached by the corrosion front during dealloying.

Shortly after, an X-ray tomography by Mahr et al. [77] revealed irregularly distributed Ag clusters, both inside the npAu ligaments and on the surface. Comparing their findings to the Ag distribution in the parent alloy, they could exclude the possibility that the Ag clusters were already present in the parent alloy. Instead, they are speculated to form during the dealloying process [77].

These results indicate that Ag is not distributed homogeneously within npAu, but is present in the form of clusters. Naturally, the catalyst surface will most probably not remain static in reactive conditions. In fact, *in situ* electron microscopy and XPS measurements demonstrated bimetallic nanoporous catalysts undergo highly dynamic geometrical and compositional changes during selective alcohol oxidation [79].

Until now, the exact mechanism of how npAu catalyzes O₂ activation has been much discussed in the literature, however it is still not entirely understood. While experimental results on the matter are still lacking, several theoretical studies dealt with possible mechanistic scenarios [63, 80]. As O₂ neither adsorbs nor dissociates on extended gold surfaces, it seemed rather unlikely that O₂ molecules adsorb dissociatively on the npAu surface and form atomic oxygen atoms that interact with adsorbed molecules on the surface [81]. Already Zielasek et al. [38] hinted at the potential assisting role of Ag impurities in the activation of molecular oxygen. Employing first principles calculations, Moskaleva et al. [63] and Fajin et al. [80] have reported that O₂ adsorption and dissociation is facilitated at steps and kinks at the npAu surface. Furthermore, they obtained lower activation barriers for O₂ dissociation and larger O₂ adsorption energies at Ag-rich sites. Interestingly, adsorbed oxygen was also shown to trigger Ag surface enrichment by theory and experiment [82, 83]. Thus, the reaction mechanisms at the npAu surface may be affected by both Ag impurities and adsorbed atomic oxygen, which may result from O₂ dissociation or be present in the as-prepared samples already. Recent theoretical studies [84, 85] presented an alternative associative adsorption mechanism, where O₂ reacts directly with molecules like CO, water or methanol instead of dissociating first.

2.3. Motivation for the present work

As described above, it is known that residual silver plays an important role for the catalytic activity of npAu and potentially influences the reaction mechanisms at the surface. Even though experimental and theoretical work on the distribution of Ag in the npAu ligaments exists [34, 40, 77–79], a detailed knowledge of the chemical and crystallographic properties of the Ag-Au alloy surface as a function of the individual environment (e.g. temperature, bulk concentration) is crucial to obtain a basic understanding of the underlying phenomena. Therefore, the present work focuses on the investigation of Ag-Au surfaces via first principles, meaning without any empirical input and solely based on physical laws. To gain information on the exact composition and configuration of the alloy surface, the segregation behavior at selected Ag-Au surfaces is analyzed and discussed. Flat as well as stepped surfaces are modeled to provide a realistic model for the rough npAu surface. In this context, it is also important to consider the influence of adsorbed species, which are always present at the surface during catalytic processes. This is realized here by adsorbing atomic oxygen at the surface and observing the changes this induces for the segregation profile. As nanoporous gold ligaments are often subject to inherent strains, the electromechanical coupling behavior, i.e. the dependence of the surface reactivity on mechanical strain, is also addressed in the following. Finally, a low energy-electron diffraction (LEED) analysis is carried out in a cooperation with an experimental group to verify the theoretical results.

Surface segregation in Ag-Au in the literature

“If we knew what it was we were doing, it would not be called research, would it?”

- *Albert Einstein*

3.1. Basic concepts in surface segregation

The fact that alloys contain distinguishable atoms leads to interesting phenomena. On the one hand, different bulk phases may form, depending on the concentration, temperature and fabrication process. On the other hand, the surface region may undergo surface segregation. Thus, a concentration gradient is created at the surface of a material consisting of at least two elements, caused by diffusion of one constituent to the surface. The driving force for this process is a difference in chemical potential between bulk and surface. As a consequence, even a small bulk concentration of a solute species may result in strong enrichment of that species at the surface which may cause a completely different atomic ordering in the surface region compared to the bulk structure. This rearrangement is also accompanied by locally altered physical and chemical properties at the surface. Therefore, analyzing and predicting surface segregation represents a crucial issue in many technologies involving surface properties, such as heterogeneous catalysis, corrosion resistance, adsorption or magnetic, electronic and optical materials [86, 87]. Over

the last decades, numerous theoretical models have been developed, relating surface segregation to different material parameters to make qualitatively as well as quantitatively valid predictions [88–92].

In a first rigorous description of the phenomenology behind surface segregation, Gibbs linked the driving force of segregation to the decrease in total free energy of the system [93]. His theory was followed by various models targeting a system’s heat of segregation, which describes the energy change when an atom of type A originally in the bulk changes position with a B atom originally at the surface. One approach represents the so-called bond-breaking models, which account for the energy cost resulting from the atomic bonds that are broken when a surface is created [94]. The total energy of the crystal is calculated as the sum of pair-bond energies between first and second neighbors [89]. If an ideal solution is assumed, there is no enthalpy of mixing, while the regular solution model allows for a non-zero energy mixing. Depending on the chosen complexity and parameters, the segregation may be limited to the topmost surface layer only or include multiple layers. Within the framework of bond-breaking models, the element that possesses the lowest bond strength will preferably diffuse to the surface to keep the energy cost as low as possible. Ordering alloys with a negative enthalpy of mixing usually exhibit an oscillatory segregation profile, meaning that the enriched element varies with each layer. While the element with the lowest bond strength is located in the topmost layer, the following alternating layers result from the preferably mixed bonds. As the heat of segregation is difficult to obtain experimentally, a link to the surface energy has been established, yielding the surface segregation of the element with the lower surface energy [91].

Not only the difference in bond strengths, but also a potential atomic size mismatch may play an important role in surface segregation. The number of broken bonds can be minimized by locating the element with the larger atomic radius at the surface, such that less atoms are needed to populate the surface. This corresponds to a locally larger lattice parameter than in the bulk and the reduction of the energy cost due to the surface creation. As a consequence, this consideration predicts enrichment of the larger atomic species in the topmost layer. In addition, a solute atom residing in a significantly smaller or larger host crystal lattice is always surrounded by an elastic strain field. This results in an elastic strain contribution to the free energy

of the material. Within this model of continuum elastic theory, the diffusion of this solute atom to the surface thus leads to a relief of lattice strain in the bulk and is energetically favorable [89, 91, 94–96].

While the latter approach will always predict surface segregation of the larger element, bond-breaking models may lead to contradicting results [95]. Therefore, a combined approach of the two models can be applied to yield more realistic surface segregation profiles. An example for such a combination is given in pair-potential approximation methods, where the total energy of a material is calculated as the sum of pairwise interactions. Unlike the bond-breaking model, however, relaxation of the atoms to their equilibrium positions is included, thereby also considering strain energy contributions. However, a correct description of the background electron gas of the metals remains a challenge for pair-potential methods. This problem has motivated the construction of electronic models for surface segregation. Among them is the embedded-atom technique, where the total electron density in the vicinity of an atom is considered to be the atomic density of this atom, plus an electronic density from the surrounding atoms. Lattice strain effects may be included by varying the atomic positions while deriving the minimum free energy [94].

3.2. Surface segregation in Ag-Au

This work deals with the prediction of surface segregation in the Ag-Au system from first principles. Based on the concepts presented above, the following assumption can be made: First, Ag and Au have nearly the same equilibrium lattice constant [97], with Au being slightly smaller. Strain contributions should therefore be negligible for surface segregation. If there was, however, any size effect causing diffusion, Ag would preferably be located at the surface to reduce the number of broken bonds. Second, the surface energy of Ag is smaller than that of Au [98], which should lead to an enrichment of Ag in the topmost layer. Previous experimental studies from the literature targeting surface segregation in Ag-Au report conflicting results. While several results show qualitative agreement, quantitative agreement is hardly found. These discrepancies may originate from different experimental sources, such as different sample preparation methodologies, the calibration of instruments, or even the choice of the experimental techniques employed.

Some examples are explained below.

Even before the actual measurement is carried out, a thorough sample preparation represents an essential step in surface science experiments. The single crystalline material must be carefully cut and cleaned from contaminants that may severely change the segregation profile, such as oxygen, carbon monoxide and other gases. After the cleaning procedure, the degree of contamination should always be checked to ensure that the surface is indeed clean. While sputter cleaning is an efficient technique to clean the surface, it may cause depletion of the element with the higher ion bombardment efficiency, making an additional annealing step necessary. One way to avoid this tedious cleaning procedure is to fabricate the surface under UHV conditions, but a defect-free structure and chemical or thermodynamic equilibrium may not be achieved easily [94].

In their review on surface segregation in gold-containing alloys, Dowben et al. [94] pointed out two advantages gold offers for segregation studies: a simple cleaning procedure and low sticking coefficients for several gases, such as CO, O₂, N₂, CO₂ and CH₄, resulting in a low contamination level even after a longer time. According to them, this leads to more reliable results for segregation studies on gold compared to other materials. Typical contaminants at the Ag-Au surface, which have been identified as S, Cl, O and N [99, 100], are most commonly removed by successive Ar⁺ sputtering and annealing procedures [94]. Still, the preferential sputtering of the other constituent is a critical issue for gold-containing alloys, which requires a thorough annealing of the surface to ensure thermodynamic equilibrium.

Even after careful sample preparation, different measurement techniques or calibration methods may lead to inconsistent results. Bouwman et al. [101] studied surface segregation on annealed polycrystalline Ag-Au bulk samples with varying Ag concentration by means of Auger Electron Spectroscopy (AES). In addition to the experimental measurements, they carried out model calculations employing the regular solution model and thereby predicted Ag enrichment in the topmost surface layer. Yet, their AES results suggested a bulk-like surface composition independent of temperature. They found their results to agree well with those of a previous AES study by Fain and McDavid [102] on epitaxially grown Ag-Au thin films, who also reported the absence of surface segregation. Another AES investigation by Somorjai and Overbury [103], however, yielded Ag surface enrichment and thereby

stands in contrast to the results by Bouwman et al. This ambiguity may have been caused by different calibration methods. Bouwman et al. applied a so-called "internal calibration", meaning they recorded AES spectra of the freshly cut, homogeneous Ag-Au surface as a reference. On the opposite, Somorjai and Overbury used the AES spectra of the pure elements as an external calibration of the system.

With regard to the Ag-Au system, it is also worth mentioning that Ag and Au possess different backscattering factors, which influences the AES outcome. This effect was observed in an AES study on polycrystalline Ag-Au foils with varying Ag bulk content by Overbury and Somorjai [99]. Without including the different backscattering factors of Ag and Au signals in their calculations, they obtained pronounced Ag surface enrichment in accordance with theoretical predictions applying the regular solution model. Only when they accounted for the difference in backscattering, the resulting Ag surface segregation was much less pronounced than predicted before and the regular solution model was no longer applicable. The authors therefore concluded that the experimental scatter and the mentioned impact of backscattering factors impeded quantitatively accurate measurements of the surface composition. During sample preparation, they furthermore observed the effect of preferential sputtering of Ag: After cleaning the surface by Ar⁺ sputtering, the surface was enriched in Au, making an additional annealing step necessary to achieve thermodynamic equilibrium. Even after careful sample preparation, they detected small amounts (<0.1 ML) of carbon and oxygen adsorbates at the surface, which may as well have affected their measured Auger spectra. Their results of moderate Ag surface segregation were corroborated by a comparable AES study by Yabumoto et al. [100] on polycrystalline Ag-Au surfaces. The latter also reported the depletion of Ag in the surface region upon Ar⁺ sputtering.

Assuming a perfectly clean Ag-Au surface in thermodynamic equilibrium, the goal of experiments investigating surface segregation is to achieve monolayer sensitivity. The most interesting result is the atomic composition of the very topmost surface layer, instead of an averaged value over a certain number of atomic layers. According to Nelson [104], AES is accompanied by a number of drawbacks, including the uncertainty about backscattering effects and the need to know the exact escape depth of the Auger electrons to assess the surface sensitivity of this technique. Due to its monolayer sensi-

tivity as well as the possibility to clean and anneal the sample in situ, Nelson therefore chose to employ ion scattering spectroscopy (ISS) instead of AES to study surface segregation in thoroughly polished Ag-Au samples. His results suggested an Ag-enriched surface, though the segregation was slightly less pronounced than predicted by the regular solution model. An additional ISS study by Kelley et al. [105] on surface segregation in Ag-Au and Pt-Cu corroborated the observations made by Nelson.

None of the experimental studies mentioned until now addressed the influence of the surface orientation on the resulting segregation. Based on the bond-breaking theory, surface segregation is expected to be most pronounced for the loosely packed surfaces, meaning segregation to the (100) surface in an fcc-based alloy will be stronger than to the (111) surface. To tackle this problem, King and Donnelly [106] applied low energy electron diffraction (LEED) and selected area channeling pattern (SACP) to identify (111), (110) and (100) planes on surface domains or grains on their polycrystalline Ag-Au samples. By means of AES, they measured the composition of the topmost two surface layers for a varying crystallographic orientation, temperature and Ag bulk content. Their results and accompanying Monte Carlo simulations are in good agreement with predictions from the bond-breaking theory, as they obtained strong Ag surface enrichment in the (100) domains, while it is weaker for the (110) domains and even less pronounced for the (111) planes. Epitaxially grown Ag-Au films with (111) orientation were analyzed via AES by Meinel et al. [107], who achieved quantitative agreement with the ISS studies from Nelson [104] and Kelley et al. [105] rather than with the results by King and Donnelly, which they suggest to be inaccurate. Concluding from their measurements, Monte Carlo simulations and the regular solution model fail to predict the correct amount of Ag segregation in small and high Ag bulk concentrations, respectively.

Several years later, Derry and Wan [108] conducted the first surface structural measurement on a Ag-Au surface via a LEED analysis of the (100) surface of an alloy containing 50% Ag. Noisy LEED measurements caused them to repeat the analysis many times and to report an average value as a result. While they measured an Ag-enriched topmost surface layer and slight Ag depletion in the second topmost layer, they did not achieve quantitative agreement with previous segregation studies.

Summing up, most experimental investigations pointed towards Ag en-

richment in the topmost layer and explained this result by the lower surface energy of Ag. The various discrepancies arising from these studies, however, call for a theoretical approach to predict the surface segregation profile in the absence of experimental error sources. Fortunately, the large variety of simulation methods that have been developed over the last decades offers a promising way to verify or explain the experimental outcome of surface segregation studies. Nevertheless, studies employing simulation methods to model surface segregation at Ag-Au surfaces are scarce, with the exception of the work of Bozzolo et al. [109]. The latter applied a quantum approximate approach, the so-called Bozzolo–Ferrante–Smith (BFS) method, where the energy of a certain atomic configuration is represented as the sum of a strain energy and a chemical energy. The required single elements for their method were determined via first-principles linearized augmented plane wave (LAPW) calculations. Generally, they obtained Ag enrichment in the topmost surface layer and Ag depletion in the subsurface layer. Interestingly, their simulations yielded a strong dependence of the amount of segregation on temperature and Ag bulk concentration. For the Ag₃₀Au₇₀ (100) surface, they reported a perfectly ordered topmost layer followed by a pure Au subsurface layer for temperatures close to 0 K. A sudden change in the segregation profile at 100 K led to a pure Ag topmost surface layer. Between 100 K and 600 K, the Ag surface layer concentration decreased monotonically until it attained an approximately constant value. This behavior was explained by the authors by two competing effects: On the one hand, the favorable heterogeneous Ag-Au bonds cause ordering at low temperatures, on the other hand, the lower surface energy of Ag leads to Ag enrichment in the topmost layer at higher temperatures.

Quantitative agreement can be found between the results for the Ag-Au (100) surface at a Ag bulk concentration of 50% obtained by Bozzolo et al. [109] and the LEED analysis by Derry and Wan [108], though the latter reported values with relatively large uncertainties: a Ag concentration within the surface layer of $76\% \pm 16\%$ and a practically bulk-like subsurface layer with a Ag concentration of $45\% \pm 18\%$ at 300 K. At this temperature, the BFS method predicted a surface layer Ag concentration of about 90%, while the subsurface layer is depleted of Ag and has a Ag concentration of only about 33%.

As mentioned earlier in Chapter 2, gold catalysis has long focused on sup-

ported nanoparticles, where bimetallic Ag-Au nanoparticles exhibited superior properties and catalytic activity as compared to monometallic Au nanoparticle catalysts. Based on this interest, various theoretic studies analyzing the structure and composition of such Ag-Au clusters of different sizes exist in the literature. Depending on the chosen simulation method and input parameters, conflicting result from these investigations.

Cheng et al. [110] performed Monte Carlo simulations to study the segregation in trimetallic Ag-Cu-Au clusters. Their calculations predicted that particles with a Ag surface, a Cu core and Au located mainly in the middle shell were thermodynamically most stable. Simple bond-breaking models are in good agreement with their results, as Cu has the highest surface energy, followed by Au and then Ag. In a further theoretical study, Curley et al. [111] modeled bimetallic Ag-Au particles consisting of 38 atoms. They employed an empirical potential, the so-called "Gupta potential", which is based on tight binding theory. In a combination with a genetic algorithm, they identified energetically favorable particle compositions and observed Ag enrichment in the surface layer. Like Cheng et al., they rationalized their findings by the lower surface energy of Ag and the strong Au-Au bonds that stabilize Au in the particle core. Still, in their discussions, they mentioned a possible electron transfer from Ag to the more electronegative Au, which would promote heterometallic Ag-Au bonds. According to them, the fact that Ag-Au is a random alloy without long-range order, however, indicates that charger transfer is negligible in Ag-Au.

More recently, Deng et al. [112] conducted a thorough study on surface segregation in Ag-Au nanoparticles, where they analyzed the influence of composition, particle size and temperature by means of the modified analytic embedded-atom method (MAEAM). Higher Ag bulk concentration, larger particle size and lower temperature all led to more pronounced Ag enrichment in the topmost layer. While also mentioning a possible effect of a charge transfer from Ag to Au, Deng et al. suggested that this influence was only important for small particles, and negligible for large particles and bulk materials. As a matter of fact, both experimental and theoretical studies found this charge transfer to promote heterometallic Ag-Au bonds and to stabilize Au in the surface layer of small Ag-Au nanoparticles containing less than eight until up to 20 atoms. While most of the investigations of larger particles employed empirical or semi-empirical potentials, it is worth noting

that the aforementioned studies on small Ag-Au particles were carried out with DFT calculations.

An interesting study by Paz-Borbon et al. [113] illustrated how the choice of the simulation method may change the outcome. They studied the surface segregation behavior of 38-atom binary clusters composed of various transition metals. Energetically favorable structures were identified via an empirical Gupta potential combined with a genetic algorithm. Those structures were subsequently calculated via means of DFT. In order to make a quantitative prediction of the driving force to surface segregation at the DFT level, the atomic positions of the two species were additionally inverted for clusters containing 19 atoms of each element. For Pd-Pt, Ag-Pt, and Pd-Au particles, the DFT calculations confirmed the low-energy structures predicted by the Gupta potential. Interestingly, the two methods led to conflicting results for Ag-Au. While the Gupta potential yielded Ag surface segregation and Au located at the particle core, DFT optimization and calculation of the inverted particle predicted a structure with an Au topmost layer to be energetically more favorable.

Whereas models taking into account surface energies and bonding interactions would not predict Au to segregate to the surface, Paz-Borbon et al. [113] explained this discrepancy with a charging effect from the less electronegative Ag to Au, which is not captured by standard empirical potential methods. It is, however, questionable, whether their findings can be transferred to clean Ag-Au surfaces, as their calculations were limited to 38-atom nanoparticles. Interestingly, a DFT study by Dianat et al. [114] revealed the influence of charge transfer on the segregation at the clean and O-covered Pt-Pd surface. Their work was motivated by a discrepancy between experimental studies reporting a Pt-enriched surface and simulations using the embedded-atom model and empirical potentials, respectively, indicating Pd surface segregation. The surface segregation behavior they observed for the Pt-Pd (111) surface depended on the underlying bulk composition. For a Pd-rich bulk, Pd was preferably located at the surface, as it has a lower surface energy than Pt. For a Pt-rich bulk, however, the energetically most favorable configuration featured a Pt surface and a Pd subsurface layer. By means of a Bader analysis [115–118], they showed that for all surface structures, there is a charge transfer from Pd to the more electronegative Pt. Thereby, the *d*-band filling of the surface Pt atoms is increased and the *d*-bands of the sub-

surface Pd atoms are depleted. Dianat et al. hypothesized that according to a model proposed by Friedel et al. [119], the surface energy of metals with more than half-filled *d*-bands decreased upon increasing *d*-band filling. Thus, the calculated charge transfer may stabilize Pt at the surface, even though Pt has the higher surface energy. Upon oxygen adsorption, the strong affinity of Pd towards O led to Pd segregation to the surface layer in all calculated structures [114].

The results by Dianat et al. indicate that for Pt-Pd, the charge transfer due to the difference in electronegativity of both elements (2.28 and 2.20 on the Pauling scale, respectively) is a decisive factor for segregation. As this difference is even larger for Au and Ag (2.54 and 1.93, respectively), the charger transfer effect may be even more pronounced for those two elements.

Methodology

In this chapter, the theoretical background, important parameters and the practical implementation of the simulation methods and experimental procedures employed in this work will be presented. The main goal is to introduce the reader to the main concepts and calculation steps without going into too much detail.

4.1. Density Functional theory

"Where did we get that from? It's not possible to derive it from anything you know. It came out of the mind of Schrödinger."

- *Richard Feynman, The Feynman Lectures on Physics*

4.1.1. The Schrödinger equation

The quotation above refers to the fundamental equation of quantum mechanics, the Schrödinger equation, which was proposed by the Austrian physicist Erwin Schrödinger in his paper "Quantisierung als Eigenwertproblem" [120] in 1926. This linear partial differential equation describes the time-evolution of a system's wave function and can be regarded as the analogue in quantum mechanics to Newton's law from classical mechanics. In its time-independent, nonrelativistic form, the Schrödinger equation for n electrons at positions $\vec{r}_1, \dots, \vec{r}_n$ and N nuclei at $\vec{R}_1, \dots, \vec{R}_N$ with the total

wave function $\Psi(\vec{r}_1, \dots, \vec{r}_n, \vec{R}_1, \dots, \vec{R}_N)$ is the following eigenvalue problem:

$$\hat{H} \cdot \Psi(\vec{r}_1, \dots, \vec{r}_n, \vec{R}_1, \dots, \vec{R}_N) = E \cdot \Psi(\vec{r}_1, \dots, \vec{r}_n, \vec{R}_1, \dots, \vec{R}_N). \quad (4.1)$$

Here, the wave functions Ψ are eigenfunctions, E is the numerical value of the energy of the state described by Ψ and \hat{H} is the Hamiltonian.

The wave function represents the mathematical description of a quantum state and it contains all the information about the quantum system at hand. To qualify as wave function, it must, however, meet certain requirements: As the electron that it describes has to be located somewhere in space, the wave function must fulfill the normalization condition:

$$\int_{-\infty}^{\infty} |\Psi(x, t)| dx = 1 \quad (4.2)$$

In addition, a wave function, whose output changes sign upon the interchange of electron coordinates is called antisymmetric. Since electrons are fermions and obey the Pauli exclusion principle, any wave function describing multiple electrons must be antisymmetric with respect to permutation of the electrons. Schrödinger's interpretation of Ψ suggested that the physical existence of matter consists only of waves, which makes E in equation 4.1 the eigenfrequencies instead of energy values. In contrast to that, Born's probabilistic interpretation focuses on the existence probability of electrons, which behaves in a classical way. He claimed that the wave function did not indicate a physical system, but only provided information on the latter. Born's theory was eventually favored by the Copenhagen school [121], led by Bohr, Heisenberg and Pauli, and has thus become the mainstream interpretation for the wave function.

The Hamilton operator \hat{H} , which acts on the wave functions, includes the following contributions for a physical system with multiple interacting nuclei and electrons:

$$\hat{H} = \hat{T}_I + \hat{T}_e + \hat{V}_{II} + \hat{V}_{ee} + \hat{V}_{eI}, \quad (4.3)$$

where in the SI unit system

$$\begin{aligned}
\hat{T}_I &= -\sum_Q \frac{\hbar^2}{2M_I} \nabla_Q^2 & : & \text{Kinetic energy of the nuclei} \\
\hat{T}_e &= -\sum_i \frac{\hbar^2}{2m_e} \nabla_i^2 & : & \text{Kinetic energy of the electrons} \\
\hat{V}_{II} &= \frac{1}{8\pi\epsilon_0} \sum_{Q \neq J} \frac{Z_Q Z_J e^2}{|\vec{R}_Q - \vec{R}_J|} & : & \text{Interaction between the nuclei} \\
\hat{V}_{ee} &= \frac{1}{8\pi\epsilon_0} \sum_{i \neq j} \frac{e^2}{|\vec{r}_i - \vec{r}_j|} & : & \text{Interaction between the electrons} \\
\hat{V}_{eI} &= -\frac{1}{4\pi\epsilon_0} \sum_{i,Q} \frac{Z_Q e^2}{|\vec{r}_i - \vec{R}_Q|} & : & \text{Interaction between electrons and nuclei}
\end{aligned}$$

The Hamiltonian \hat{H} can be further simplified if one takes into account the different masses of nuclei and electrons. Due to a typical mass ratio of $\frac{M_I}{m_e} \approx 10^3 \dots 10^5$, the electrons experience a much larger acceleration by the Coulomb interaction forces than the nuclei. Therefore, the electronic system follows the nuclear motions instantaneously and is in thermodynamic equilibrium at all times (*adiabatic theorem*). This approach is called Born-Oppenheimer approximation [122] or clamped-nuclei approach.

Thus, it is possible to break up the wave function into electronic and nuclear components:

$$\Psi(\vec{r}_1, \dots, \vec{r}_n, \vec{R}_1, \dots, \vec{R}_N) = \Psi_{\text{el}}^{\vec{R}_1, \dots, \vec{R}_N}(\vec{r}_1, \dots, \vec{r}_n) \cdot \Psi_I(\vec{R}_1, \dots, \vec{R}_N). \quad (4.4)$$

Consequently, the electron wave function is independent of the ionic components \hat{T}_I and \hat{V}_{II} and the atom positions appear only as fixed parameters. The former \hat{V}_{eI} now corresponds to an external potential \hat{V}_{ext} defined by the nuclear coordinates. In reality, however, this external potential may also include external magnetic and electric fields in addition to the nuclear field. These assumptions finally result in the following Hamiltonian for the electron system:

$$\hat{H}_{\text{el}} = \hat{T}_e + \hat{V}_{ee} + \hat{V}_{\text{ext}}. \quad (4.5)$$

Unfortunately, the Schrödinger equation remains a many-body problem that can only be solved analytically for a few special cases, such as the hydrogen atom or hydrogen-like atoms. The full electronic wave function

contains three dimensions for each of the electrons, making it a challenge even for the computation capacity available nowadays.

The information given in this chapter about the history, principles and application of density functional theory has mostly been taken from fundamental books on the topic by Sholl and Steckel [123], Koch and Holthausen [124] and Tsuneda [125]. The reader is encouraged to consult these books for a more detailed description.

4.1.2. Historic and physical background of density functional theory

One year after the Schrödinger equation had been published—in 1927—Llewellyn Thomas [126, 127] and Enrico Fermi independently developed the Thomas-Fermi-Model. The model was formulated in terms of an electron density distribution and may thus be regarded as an early predecessor of modern density functional theory. In their theory, Thomas and Fermi assumed a uniform electron gas for small volume elements and a variation of the electron density over different volume elements. Although this model was useful to obtain qualitative trends, it failed to give reliable numerical results and could not even reproduce chemical binding [128].

In 1928, Douglas Hartree [129] lay the foundation for a well-known wave-function based method: the Hartree-Fock method. He represented the wave function as the product of single electron wave functions and applied a self-consistent field (SCF) method to solve the single electron Schrödinger equation for the one-electron eigenvalue, also called orbital energy. Though atomic orbital shapes could be reproduced very well within the Hartree method, the resulting energy values were too inaccurate due to the lack of electron-electron exchange interactions. The latter resulted from the fact that the Hartree product of one-electron wave functions did not satisfy the principle of antisymmetry of the wave function, which was proposed by Heisenberg and Dirac in 1926. This drawback was overcome independently by Vladimir Fock [130] and John C. Slater [131] in 1930, who both replaced the Hartree product by a Slater determinant. This normalized determinant represents the exact wave function of non-interacting electrons within an external potential. Thereby, the Hartree-Fock method theoretically yielded the exact electron exchange, provided that an infinitely large wave function basis set was used for the calculation. However, solving the Hartree-Fock equations with the SCF

method, even with a restricted basis set, was not possible until the appearance of computers. Also with the help of computers, chemical accuracy with errors of about 0.1 Å could not be achieved with the Hartree-Fock method. The difference between the exact solution and Hartree-Fock energies was defined as electron correlation by Peer-Olov Löwdin [132] in 1955. Physically speaking, electron correlation can be understood as an instantaneous repulsion of the moving electrons. More sophisticated techniques to handle the electron correlation contribution to the total energy include Møller-Plesset perturbation theory (MP2, MP4...) and methods based on configuration interaction (CI), quadratic CI (QCI) or couples cluster approaches (CC), which will not be explained here in further detail.

In 1964, Pierre Hohenberg and Walter Kohn published a landmark paper [1] with two prominent theorems that lay the foundation for density functional theory as we know it today. Their first theorem can be stated as follows:

Theorem 1 *The ground-state energy E_0 of a many-body system of fermions subjected to an external potential is a unique functional¹ of the electron density $\rho_0(\vec{r})$: $E_0 = E[\rho_0(\vec{r})]$.*

Following the probabilistic interpretation of the wave function of the Copenhagen school, the electron density $\rho(\vec{r})$ actually represents a probability density of finding one of n electrons within a volume element $d\vec{r}_1$:

$$\rho_0(\vec{r}) = n \int_{\vec{r}_2} \dots \int_{\vec{r}_n} |\Psi_{\text{el}}^{\vec{R}_1, \dots, \vec{R}_N}(\vec{r}, \vec{r}_2, \dots, \vec{r}_n)|^2 d^3r_2 \dots d^3r_n. \quad (4.6)$$

As a consequence to this definition, $\rho(\vec{r})$ must vanish in infinity and integrate to the total number of electrons. As Walter Kohn emphasized in his Nobel lecture [128] after sharing the Nobel Price with John A. Pople in 1998, one benefit of DFT was the use of the electron density, a quantity in the real, three dimensional coordinate space. In contrast to the wave function, the electron density is an observable that can be measured in experiment. While providing a physical understanding of the multiparticle system, $\rho(\vec{r})$ contains the same information about the ground-state observables as the total wave function. Proving Hohenberg's and Kohn's first theorem is relatively straightforward and is based on *reductio ad absurdum*.

¹A functional maps from a vector space into its underlying scalar field. It is often considered a "function of a function".

However, the question of how a certain electron density may be identified as the true ground-state density remains unresolved. The second theorem of Hohenberg and Kohn provides the strategy to tackle this problem:

Theorem 2 *The electron density $\rho_0(\vec{r})$ that minimizes the energy functional $E[\rho_0(\vec{r})]$ under the condition $\int \rho_0(\vec{r}) d\vec{r} = n$ is the ground-state electron density corresponding to the solution of the Schrödinger equation.*

Simply put, any trial electron density, which satisfies the boundary conditions, will yield an energy from the functional $E[\rho_0(\vec{r})]$ that represents an upper bound to the true ground-state energy. The ground-state energy $E[\rho_0(\vec{r}, \{\vec{R}\})]$ then includes the following contributions:

$$E[\rho_0(\vec{r}, \{\vec{R}\})] = T_e[\rho_0(\vec{r})] + E_{ee}[\rho_0(\vec{r})] + E_{el}[\rho_0(\vec{r})] + E_{II}[\{\vec{R}\}]. \quad (4.7)$$

The first three summands in equation (4.7) are functionals of the electron density, while the interaction between the nuclei directly depends on the nuclear coordinates.

Hence, the two theorems of Hohenberg and Kohn provide a unique mapping between the ground-state electron density and the ground-state energy. However, they do not give any instructions on how this energy functional can be constructed and how to obtain the ground-state density. Shortly afterwards, in 1965, Walter Kohn and Lu J. Sham [2] proposed a strategy to overcome this problem: Instead of considering a system of interacting electrons, they introduced a formal transition to a non-interacting reference system built from a set of one-electron functions. Similar to the Hartree-Fock method, they replaced the total wave function by a combination of the individual single electron wave functions $\Psi_i(\vec{r})$ within a Slater determinant. Thus, a major part of the system's kinetic energy can be calculated accurately and the ground-state energy from equation (4.7) can be written in the following way:

$$E[\rho_0(\vec{r}, \{\vec{R}\})] = T_s[\rho_0(\vec{r})] + E_H[\rho_0(\vec{r})] + E_{eI}[\rho_0(\vec{r})] + E_{II}[\{\vec{R}\}] + E_{xc}[\rho_0(\vec{r})] \quad (4.8)$$

with the three new terms T_s , E_H and E_{xc} . T_s is the kinetic energy of the non-interacting system, which can be determined analytically. The second term E_H represents the Coulomb repulsion between one electron and the

total electron density and it is called Hartree energy:

$$E_{\text{H}}[\rho(\vec{r})] = \frac{e^2}{2} \int \frac{\rho(\vec{r})\rho(\vec{r}')}{|\vec{r} - \vec{r}'|} d\vec{r}d\vec{r}'. \quad (4.9)$$

As the electron considered in equation (4.9) is also part of the total electron density, the Hartree potential contains an interaction between the electron and itself. The third new term in equation (4.8), the exchange-correlation energy E_{xc} , accounts for this error and other phenomena, like the missing part of the kinetic energy and the interaction between the electron and its exchange hole². Thus, one important contribution by Kohn and Sham was to separate all terms that must be determined by an approximate functional and include them in the exchange-correlation energy. Fortunately, the latter makes only a small fraction of the total energy and the major part may be computed exactly.

The form of the final Kohn-Sham equations is very similar to the Schrödinger equation (4.1), but the single-electron wave functions $\Psi_i(\vec{r})$ depend on only three spatial variables and there are no summations:

$$\left[\frac{\hbar^2}{2m_e} \nabla^2 + V_{\text{ext}}(\vec{r}) + e^2 \int \frac{\rho(\vec{r}')}{|\vec{r} - \vec{r}'|} d^3\vec{r}' + V_{\text{xc}}(\vec{r}) \right] \Psi_i(\vec{r}) = \epsilon_i \Psi_i(\vec{r}), \quad (4.10)$$

where the Hartree potential V_{H} is the functional derivative of the Hartree energy E_{H} and the exchange-correlation potential V_{xc} is the functional derivative of the exchange-correlation energy E_{xc} . If E_{xc} was known exactly, the Kohn-Sham equations would provide an exact solution to the Schrödinger equation. It should be noted here that $V_{\text{ext}}(\vec{r})$ in equation (4.10) corresponds to the fictitious external potential, leading to the exact same electron density for non-interacting particles as that for the interacting electrons in the real external potential.

Similar to the Hartree-Fock method, the Kohn-Sham equations cannot be solved directly. This becomes evident in equation (4.9), where the electron density is needed to obtain the Hartree energy. To determine the electron density, one needs the single-electron wave functions, which again may be calculated with the Kohn-Sham equations. To solve those, however, the

²Electrons obey the Pauli exclusion principle, stating that no two fermions may occupy the same quantum state at the same time. In a system with multiple nuclei and electrons, every electron with a given spin is surrounded by a region with a decreased density of electrons with the same spin. This phenomenon is called *exchange hole* or *Fermi hole* [133]

Hartree energy is required. Thus, the calculation is a self-consistent cycle.

Once the ground-state electron density is obtained, it is in theory possible to extract the ground-state wave function from it. However, numerous antisymmetric wave functions lead to the same electron density and it is in practice impossible to identify the true ground-state wave function that minimizes the energy. Therefore, it is important to realize that DFT does not provide access to any real wave function.

4.1.3. The exchange-correlation functional

As already mentioned above, the exchange-correlation functional is the only term in DFT that needs to be approximated. Finding a suitable functional is by itself a formidable task, which has occupied scientists for decades until nowadays. This is mainly due to the fact that nothing is known about the explicit form of the functional. Therefore, existing functionals cannot be improved systematically to approach the exact solution, and developing new functionals always has a "trial and error" character.

According to Tsuneda [125], potential candidates must fulfill the following five conditions:

1. They must satisfy certain fundamental physical conditions.
2. They should reproduce reactions and properties for numerous molecules to great accuracy.
3. They should be kept simple by including as few parameters as possible.
4. No artificial terms should be added only to meet specific requirements.
5. They must be versatile and account for all kinds of physical corrections without having to change parameters.

The easiest and most straightforward approximation for the exchange-correlation energy is given within the local density approximation (LDA). The basic concept behind LDA is a hypothetical uniform electron gas, for which the exchange-correlation energy may be determined exactly. LDA calculates this value at each position ϵ_{xc}^{LDA} and then integrates over all positions:

$$E_{xc}^{LDA}[\rho(\vec{r})] = \int \rho(\vec{r}) \epsilon_{xc}^{LDA}(\rho(\vec{r})) d\vec{r}. \quad (4.11)$$

This idea of valence electrons on a positive background charge distribution represents a suitable physical model for simple metals, such as sodium. LDA has proven to yield good results for the determination of structure, vibrational frequencies, elastic moduli and phase stability [134–137], though an overbinding usually leads to too small lattice parameters [138].

For materials with a strongly varying electron density, it is useful to account for this inhomogeneity by including the gradient of the electron density in the exchange-correlation energy. This approach is called generalized gradient approximation (GGA) [139–141]:

$$E_{\text{xc}}^{\text{GGA}} = \int f(\rho(\vec{r}), \nabla\rho(\vec{r})) \, d\vec{r}. \quad (4.12)$$

The functional of the electron density and density gradient can be expressed in many ways and every method leads to slightly different results. Among the vast number of available GGA functionals, two very popular ones are the *Perdew-Wang functional* (PW91) [139] and the *Perdew-Burke-Ernzerhof functional* (PBE) [141].

So-called meta-GGA functionals, such as the TPSS functional by Tao, Perdew and co-workers [142, 143], additionally consider the kinetic energy density $\nabla^2\rho$ to improve the approximation of the GGA functionals. Attempting to reach even higher accuracies, hybrid or hyper-GGA functionals mix the GGA exchange functional with the Hartree-Fock exact exchange. Examples for this method are the Becke, three-parameter, Lee-Yang-Parr (B3LYP) [144–146] and the Heyd-Scuseria-Ernzerhof (HSE) [147, 148] screened Coulomb hybrid functional.

In 2001, John Perdew, who was involved in the development of many exchange-correlation functionals, created the image of a "Jacob's ladder" [149] with increasing accuracy at increasing complexity (see figure 4.1). Still, it should be noted that not all applications require the highest accuracy and that selecting the appropriate functional for the task at hand is an important process in DFT calculations. It is therefore crucial to test the performance of different functionals and name the chosen one with the results upon publication.

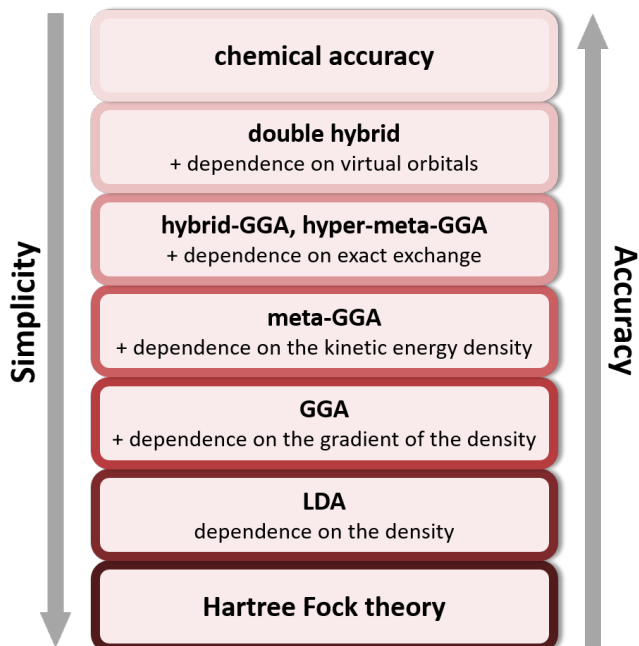


Figure 4.1.: Illustration of Perde's "Jacob's ladder" [149] with exchange-correlation functionals and their corresponding parameters ranging between the Hartree-Fock method and chemical accuracy.

4.1.4. Important concepts for the practical implementation of DFT

The appearance and development of computers in the 1950s brought new possibilities for many research fields, including quantum physics and chemistry. Since then, numerous DFT program codes have emerged, for example the local orbital basis codes SIESTA and CRYSTAL and the plane wave basis codes VASP, ABINIT and CASTEP. This distinction refers to whether the Kohn-Sham orbitals are expanded with spatially localized or spatially periodic functions. While a local orbital basis set is useful for calculations of isolated molecules, as they reproduce the decay to zero of the wave function far away from the molecule, plane waves imply periodic boundary conditions and thus enjoy great popularity for bulk calculations in solid state physics. In this work, all calculations were carried out with the plane-wave based program code VASP (Vienna Ab Initio Simulation Package). Input parameter or file names, which are given throughout this work, are therefore specific to VASP.

When the Kohn-Sham equations are to be solved numerically, reasonable approximations are necessary to increase computational efficiency. It is important to keep in mind that even without those approximations, the Kohn-Sham equations would not yield an exact solution for the Schrödinger equation, since the exchange-correlation energy is not known. In the following, important concepts and parameters for the practical implementation of DFT will be briefly explained. The goal should always be to aim for maximum required accuracy at minimal computational cost, and parameters should be chosen accordingly.

Cutoff energy

Computational effort may be reduced drastically by taking advantage of a system's symmetries and periodicities. Bloch's theorem states that the solutions of the Schrödinger equation for a periodic solid can be represented as a sum of plane waves modulated by a function $u(\vec{r})$, which is periodic in space with the same periodicity as the lattice vectors:

$$\Psi_{\vec{k}} = e^{i\vec{k}\cdot\vec{r}} u_{\vec{k}}(\vec{r}). \quad (4.13)$$

The function $u(\vec{r})$ can furthermore be written as a set of plane waves summed up over all reciprocal lattice vectors \vec{G} :

$$u(\vec{r}) = \sum_{\vec{G}} c_{\vec{G}} e^{i\vec{G}\cdot\vec{r}}. \quad (4.14)$$

Combining equations (4.13) and (4.14) gives for the solutions of the Schrödinger equation

$$\Psi_{\vec{k}} = \sum_{\vec{G}} c_{\vec{k}+\vec{G}} e^{i(\vec{k}+\vec{G})\vec{r}}, \quad (4.15)$$

which have the kinetic energy

$$E_{\text{kin}} = \frac{\hbar^2}{2m} |\vec{k} + \vec{G}|^2. \quad (4.16)$$

The valence electrons, which are relevant for chemical bonding, possess a lower kinetic energy than the ones close to the atomic core. It is therefore reasonable to truncate the sum in equation (4.15) to include only certain kinetic energy values lower than a so-called cutoff energy E_{cut} with a finite number of reciprocal lattice vectors with $|\vec{k} + \vec{G}| < |\vec{G}_{\text{cut}}|$. The appropriate value of E_{cut} has to be determined in convergence tests for each system, as it depends on the element, the calculated quantity and the required accuracy.

K-point grid

Calculating various properties of a system, such as its energy, forces or density of states, requires integration over all occupied electronic states. Taking advantage of the translational symmetry through Bloch's theorem, these calculations are much more convenient to solve in reciprocal space than in real space. Due to the periodicity, it is sufficient to perform integrations within the first Brillouin zone³. In addition, integrals may be approximated by performing a discrete integration over a finite number i of special k-points with an assigned weighing factor $\omega_{\mathbf{k}_i}$ [150]:

$$\frac{1}{\Omega_{\text{BZ}}} \int_{\text{BZ}} f(\vec{k}) d\vec{k} \Rightarrow \sum_{\mathbf{k}_i} \omega_{\mathbf{k}_i} f(\vec{k}). \quad (4.17)$$

³By definition, the Brillouin zone is the primitive cell of the reciprocal lattice, analogue to the Wigner-Seitz cell of the Bravais lattice.

A possible strategy to choose these points is the method proposed by Monkhorst and Pack [151], which was used throughout this work. First, a grid of equally spaced points is spread along the reciprocal lattice vectors. The translational and rotational symmetries are subsequently used to identify equivalent points and reduce the total number of k-points by erasing those equivalent points. For a fcc (face-centered cubic) bulk material and eleven k-points in all three directions x, y and z, for instance, the number of necessary k-points is thereby reduced from 1331 to only 56. The remaining k-points are called *irreducible k-points* and lie in the *irreducible Brillouin zone (IBZ)*. This way, the numerical effort as well as the calculation times are decreased. It is reported that for a small number of k-points, a better convergence can be expected for an even number of k-points than for an odd one [123]. However, choosing an odd number is physically reasonable, as the high-symmetry Γ -point is included in the integration. In addition to that, the number of irreducible k-points is much smaller if the Γ -point is included.

The function $f(\vec{k})$ in equation (4.17) is continuous with \vec{k} for systems with a finite band gap, meaning insulators and semiconductors. Therefore, already a small number of k-points is mostly sufficient to accurately approximate the integral. For metals, though, the integrand is discontinuous at the Fermi energy and many k-points are necessary to replace the integral with a finite k-point sampling. So-called smearing methods replace the step function in the integral with a smooth function, by introducing a finite unphysical temperature. This occupation of nominally unoccupied states above the Fermi energy causes an error in the resulting energy. It is important to find a balance between keeping the error small and reducing the number of k-points to a feasible number.

Pseudopotentials

DFT calculations may be further simplified regarding the electrons close to the core. Within the framework of *all-electron* methods, the ground-state energy of all electrons in the system is determined. Consequently, a large plane wave basis has to be included, even though the tightly bound core electrons are unimportant for many properties like chemical bonding. Pseudopotential methods do not consider the core electrons explicitly in the calculations (*frozen core approximation*). Instead, the Coulomb interaction between the nuclei and the core electrons are combined in an effective potential, which

is “seen” by the valence electrons. This pseudopotential is applied within a certain cutoff radius r_c . A crucial condition for this approach is that this smoothed potential must match important mathematical and physical properties of the real ion core, such as the scatter properties. Due to the softer potential instead of the steep $\frac{1}{r}$ -potential, the pseudo one-particle wave functions possess less nodes and the size of the plane wave basis can be reduced considerably. Pseudopotentials for certain types of atoms are associated with a minimum cutoff energy that should be applied in calculations. High required cutoff energies characterize so-called hard pseudopotentials, while those with low necessary cutoff energies are said to be soft. Special *ultrasoft pseudopotentials* (USPP) [152, 153] offer very smooth potential characteristics, even though the charge conservation is not guaranteed. The *projector augmented-wave method* (PAW) [154, 155] – which was used throughout this work – combines the accuracy of all electron methods and the efficiency of USPPs. All nodes of the valence electrons’ eigenfunctions are included, while the frozen core approximation is applied. Figure 4.2 shows the difference between the real potential V and wave function Ψ and the pseudopotential V_{pseudo} and resulting pseudo one-particle wave function Ψ_{pseudo} .

4.1.5. Initial geometry and geometry optimization

VASP offers the possibility of geometry optimization of a predefined starting configuration. Applying the Hellmann-Feynman theorem⁴, forces acting on the ions are calculated by the expectation value of the gradient of the electronic Hamiltonian in the ground-state. The atoms are subsequently moved along the direction of the forces and the forces are again calculated. This procedure, which is called relaxation, is repeated until the forces fall below a selectable threshold value.

The geometry of any system is specified via a lattice parameter, three lattice vectors and the atomic positions within the lattice in VASP. Determining an initial geometry represents an important step in every DFT calculation. Even though the atomic positions may be relaxed, the starting configuration should be as close to the actual ground-state configuration as possible. If two atoms are much too close, for instance, the numerical optimization algorithm will recognize that the two atoms want to move away from each other. The

⁴The Hellmann-Feynman theorem [156, 157] states that the derivative of the total energy with respect to a parameter (here the position vector \vec{r}) equals the expectation value of the derivative of the Hamiltonian with respect to that parameter.

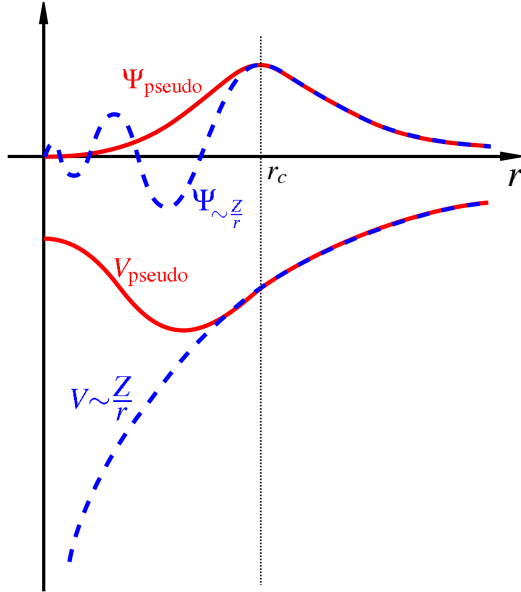


Figure 4.2.: Illustration of pseudopotential approach. Within the cutoff radius r_c the real potential $V \propto \frac{1}{r}$ is replaced by the pseudopotential V_{pseudo} . This results in a smoother one-particle wave function. Outside r_c the potentials and wave functions are identical.

size of this initial step may then be so large that the true minimum energy state is never found by the calculation. It is also possible to reach a local minimum in the energy landscape instead of the global energy minimum, which represents the true ground state. Thus, developing an idea of where the final positions will be – for example by comparing to experimental values – helps to obtain useful results.

Figure 4.3 illustrates the self-consistent DFT calculation process including the relaxation. Starting from a trial electron density $\rho(\vec{r})$, the Kohn-Sham equations are solved to obtain the Kohn-Sham orbitals $\psi_i(\vec{r})$ and calculate the new Kohn-Sham electron density $\rho_{\text{KS}}(\vec{r})$. The two densities are compared and if they are not equal, they are mixed into a new trial density and the procedure is repeated until the input density equals the calculated one. With this ground-state electron density, the total energy and the forces on the ions are computed. When the relaxation threshold force is reached, the obtained

total energy corresponds to the ground-state energy E_{tot} for this specific configuration.

Surface calculations with VASP

The characteristics of surfaces and interfaces dominate many technologically relevant processes, such as catalysis or photovoltaics. The possibility to calculate and predict their behavior at an atomic scale has shed new light on numerous phenomena in surface science.

In order to model a solid surface in VASP, several adjustments have to be made to the input data, as compared to bulk calculations. While the latter require periodic boundary conditions in all three directions, surfaces are only periodic in two dimensions. To meet the periodicity in three dimensions dictated by the plane waves used in VASP, a supercell is constructed. The latter is also called surface slab and it contains a certain number of atomic layers and a vacuum region (see Figure 4.4). This way, an infinite number of surfaces is created. At this point, it is important to include a sufficiently large vacuum region to ensure that the electron density decreases to zero in the vacuum and two adjacent surfaces do not interact.

Furthermore, the atomic layers may be either symmetric (with the surface of interest at both sides of the layers) or asymmetric (with the surface of interest at one side and fixed bulk layers at the other side). Employing symmetric surface slabs requires more atomic layers and thereby increases calculation time, but it also offers certain advantages. First, VASP may exploit the higher symmetry and thus increase the efficiency of the calculations. Second, asymmetric slabs may cause an electric dipole within the vacuum region between the upper and lower surface, leading to a very slow convergence of the total energy with increasing thickness of the vacuum. A so-called dipole correction [158, 159] in the direction of the surface normal helps to overcome this problem by placing a charge within the vacuum that compensates for the dipole generated by the two surfaces.

Analogous to bulk calculations, the supercell is defined by three lattice vectors and fractional or Cartesian coordinates for each atom it contains. Ideally, the equilibrium bulk lattice constant obtained from well-converged bulk calculations is employed in the surface slab to avoid internal stresses. The long dimension along the surface normal in real space corresponds to a very short dimension in the reciprocal space. Therefore, only one k-point is

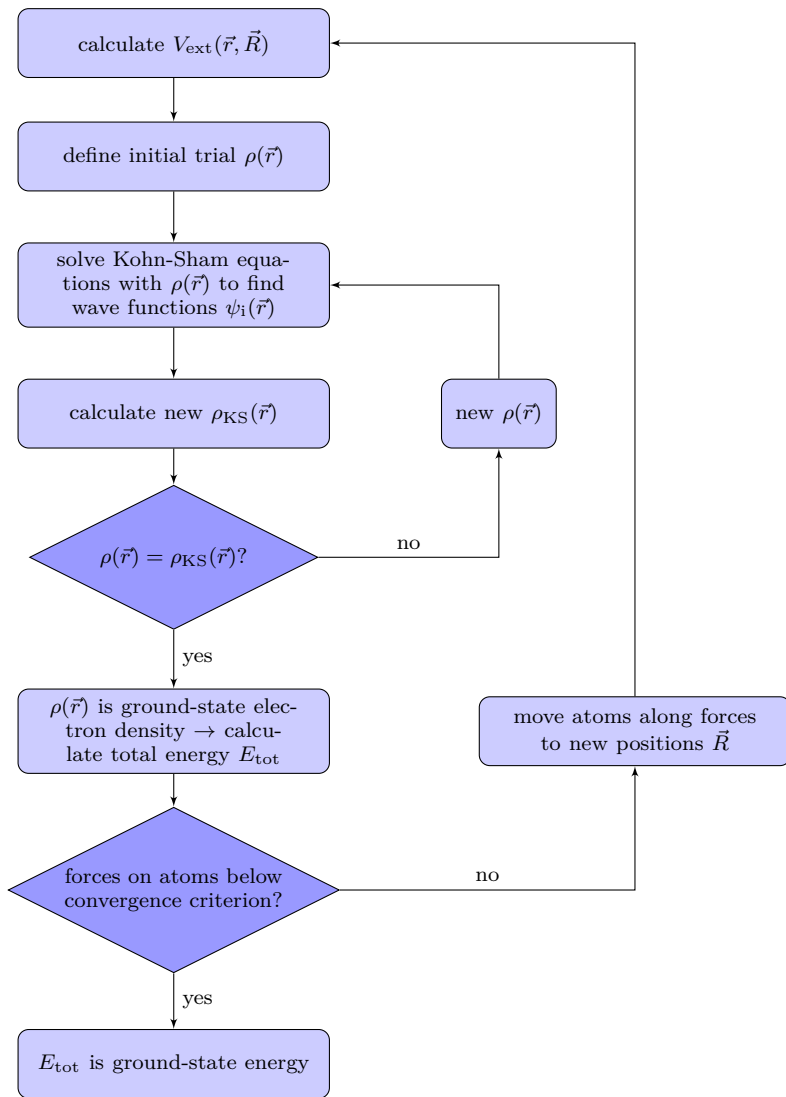


Figure 4.3.: Flow chart of a self-consistent DFT calculation. The ground state electron density is determined in a self-consistent loop starting from a trial electron density, for which the Kohn-Sham equations are solved. For the case of additional relaxation another self-consistent calculation loop is entered, which stops when the forces on the atoms are below a convergence criterion stated in the INCAR file.

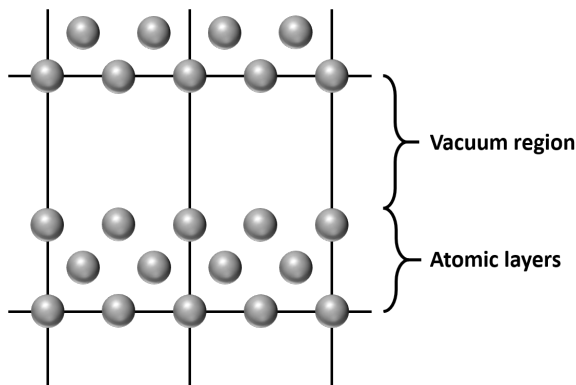


Figure 4.4.: Illustration of the surface slab employed in VASP. Atomic layers are separated by a vacuum region to realize the periodicity in two dimensions of the surface.

usually sufficient in the direction.

Since any surface represents a discontinuity in the crystal lattice and the coordination of the surface atoms is reduced, the first few atomic layers usually undergo inward or outward surface relaxation. In many cases, the atoms rearrange drastically to minimize the total energy and the surface reconstructs, leading to a different structure than in the bulk.

4.2. Cluster expansion

"In all chaos there is a cosmos, in all disorder a secret order."

- Carl Gustav Jung

Two types of atoms crystallizing on a common lattice may either order or cluster, depending on whether mixed or mono-atomic bonds are energetically favored. Numerous problems in materials science aim at characterizing the order or the lack of such in multi-component systems. These so-called configurational problems include the search for ground states of crystalline metal alloys or semiconductor systems, surface segregation, segregation of defects at interfaces, and adsorption of atoms or molecules on surfaces [160, 161].

Considering a binary system with N atoms, the configuration space comprises 2^N possible configurations. Calculating the relaxed structures and

energies for all of those structures is hardly feasible by means of DFT, especially if relatively large unit cells containing up to 20 atoms or more are to be included. Several modern approaches try to circumvent this problem by employing a simplified electric Hamiltonian or by using empirical potentials, such as the embedded atom method (EAM) [162–164] or the coherent potential approximation (CPA) [165, 166]. However, the latter generally exclude symmetry-lowering geometric relaxations and thus yield accurate results only for bulk systems with a small lattice mismatch. Regarding surfaces and segregation phenomena, changes in the interlayer distances within the first few surface layers are very common and may influence the segregation profile [160, 167]. Therefore, neglecting surface relaxation possibly leads to incorrect results and an alternative approach becomes necessary.

4.2.1. Theoretical background

A very powerful tool to assess the whole configuration space is the combination of DFT calculations with a method from statistical physics, the cluster expansion (CE) [168]. The latter was based on the Cluster Variation Method proposed by Kikuchi [169, 170] and the Connolly-Williams-method [171]. The underlying idea of the CE is to perform a transition from real space coordinates to the configuration space. Any given observable, such as the total energy, which solely depends on the atomic configuration, can then be represented as the linear sum of characteristic energies of geometric figures or clusters. Figure 4.5 shows the division of a simple cubic lattice in the empty cluster⁵, the on-site cluster, a nearest-neighbor pair and the smallest triplet and quadruplet cluster, respectively. The mathematical framework for this theory was provided by Sanchez et al. in the early 1980s [172, 173].

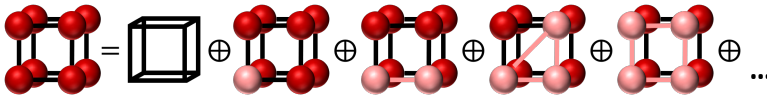


Figure 4.5.: Schematic illustration of the figures that a simple cubic crystal lattice is divided into for the CE. Depicted is the empty cluster, the on-site cluster, a nearest-neighbor pair, the smallest triplet cluster and and smallest quadruplet cluster.

⁵The empty cluster always has the value +1. Analogous to $x^0 = 1$ in an expansion in powers of x , this term of the CE is always a constant and together with the on-site cluster represents the contribution of the disordered system with zero mutual interaction.

In practice, a spin value S_i is assigned to each atom i , so that in the binary case the problem resembles an Ising-like [174] model with spins of $S_i = +1$ if the site is occupied by an A atom and $S_i = -1$ if it is occupied by a B atom of an $A_{1-x}B_x$ alloy. A particular configuration is then given by a vector σ , each component of which corresponds to an atomic site. The energy of this configuration is expressed as a linear combination of characteristic energies J of the clusters illustrated in Figure 4.5:

$$E(\sigma) = J_0 + \sum_i J_i S_i(\sigma) + \sum_{j < i} J_{ij} S_i(\sigma) S_j(\sigma) + \sum_{k < j < i} J_{ijk} S_i(\sigma) S_j(\sigma) S_k(\sigma) + \dots \quad (4.18)$$

Here, the first two terms include the empty cluster and the on-site cluster and they represent the random alloy without any mutual interaction. The third term gives all pair interactions, the fourth all triplet interactions and so forth. The spin product for a certain figure F with m sites gives its correlation function Π_F , which (for the binary case) can either take the value $+1$ or -1 :

$$\Pi_F(\sigma) = S_1(\sigma) \cdot S_2(\sigma) \cdot \dots \cdot S_m(\sigma) = \pm 1 \quad (4.19)$$

Depending on the underlying crystal lattice, a certain number of clusters will be symmetrically equivalent and will therefore yield the same contribution to the total energy $E(\sigma)$. This is accounted for by a factor D_F , which gives the number of equivalent clusters of class F normalized to the total number of sites N of the configuration (see Figure 4.6).

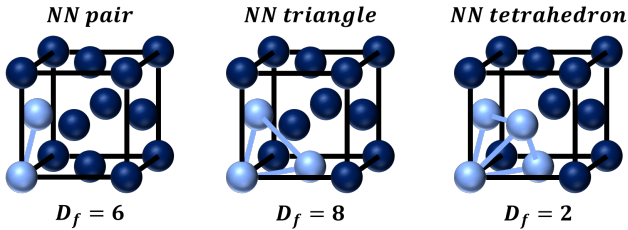


Figure 4.6.: Degeneracies D_f of three example clusters on the fcc lattice.

Using this degeneracy factor, Equation (4.18) may be shortened by introducing the correlation function of symmetrically equivalent clusters $\bar{\Pi}_F$ for a particular configuration σ :

$$\bar{\Pi}_F(\sigma) = \frac{1}{ND_F} \sum_f S_1(\sigma) S_2(\sigma) \dots S_m(\sigma), \quad (4.20)$$

where f runs over the total number of clusters of class F and m is the number of sites of cluster f . Inserting this into Equation (4.18) yields:

$$E(\sigma) = N \sum_F D_F \bar{\Pi}_F(\sigma) J_F. \quad (4.21)$$

The Hamiltonian in Equation 4.21 contains 2^N interactions J for the 2^N possible configurations. Leaving out the constants, Equation 4.21 can therefore be written as a $2^N \times 2^N$ linear equation system in the following way:

$$\begin{bmatrix} E(\sigma_0) \\ \vdots \\ E(\sigma_{2^N-1}) \end{bmatrix} = \begin{bmatrix} \Pi_0(\sigma_0) & \dots & \Pi_{2^N-1}(\sigma_0) \\ \vdots & \ddots & \vdots \\ \Pi_0(\sigma_{2^N-1}) & \dots & \Pi_{2^N-1}(\sigma_{2^N-1}) \end{bmatrix} \begin{bmatrix} J_0 \\ \dots \\ J_{2^N-1} \end{bmatrix} \quad (4.22)$$

Sanchez et al. [172] have proven that this equation system is always solvable, as the matrix of configuration functions is orthogonal. Consequently, in theory, the expansion above provides an exact result for the total energy of every possible atomic configuration, thus rendering numerous more time consuming calculations, such as by means of DFT, unnecessary. However, determining the characteristic energies J_F for such a large number of clusters would not save any time or effort compared to calculating every single configuration "by hand". Therefore, two important questions arise at this point:

1. How many effective interactions and clusters need to be included in the expansion to obtain a result that is sufficiently close to the exact one?
2. Which interactions are important to characterize the system and which ones may be left out without severe consequences?

Physical intuition suggests that the interactions should become weaker with increasing distance, meaning pair interactions spanning over five atoms should be less important than nearest neighbor interactions [175, 176]. Still, even including only figures within a certain cutoff distance may lead to thousands of possible clusters to choose from. Furthermore, some systems may

require long-range interactions to correctly describe the energetics, so that employing only pair and maybe triplet interactions may not be enough.

4.2.2. Genetic algorithm

A popular method which is very suitable for such large and highly correlated search spaces is the Genetic Algorithm (GA)⁶ [179]. The latter mimics the biological concept of "survival of the fittest" by Darwin [180] to obtain the optimal result for the problem at hand. Numerous studies from the past have demonstrated its potential to successfully and efficiently identify the important effective interaction within a cluster expansion (see, for example, References [161, 181–184]). Figure 4.7 schematically illustrates the working principle of the GA. Every possible set out of the total number of clusters n is represented by an n -dimensional vector, the "genome", which consists of 0's and 1's, the "genes". A cluster with the entry 0 is not included in the set for the fit, while the entry 1 means that it is included. A random pool of genomes, also called the population, represents the starting point for the GA. Throughout the whole optimization process, the predictive power of all individual genomes is measured and evaluated. This may be realized by invoking the leave-many-out cross-validation score S_{CV} [185, 186] as a fitness criterion. Given a total number N of DFT input structures, S_{CV} is obtained in the following manner:

1. The set of input structures is divided in k disjoint subsets of $\frac{N}{k}$ elements.
2. Each subset is used as a test set and the fit is performed for the remaining $k - 1$ sets. The outcome is thus not influenced by the respective test set.
3. The resulting effective interactions are employed to predict the energetics of the configurations included in the test set and the result is compared to the total energy obtained by DFT.
4. The k -fold cross-validation error is calculated as the root-mean-square

⁶Other methods are, for example, the direct Connolly-Williams inversion and Compressed sensing. These alternative approaches will not be discussed here, the interested reader may find more information in References [171, 177, 178].

error for all predicted configurations:

$$S_{CV} = \sqrt{\frac{1}{k \frac{N}{k}} \sum_k \sum_{\frac{N}{k}} |E_{\text{DFT}}(\sigma) - E_{\text{CE}}(\sigma)|^2} \quad (4.23)$$

Generally, values for S_{CV} around and below 1 meV are considered to yield a high predictive power of the fit. Those genomes of the starting population with a high fitness (meaning a low value for S_{CV}) are mated to create "children". One by one, each gene of the child genome is passed on from either parent, while the probability is related to the relative fitness of the parents. This new generation of children is subsequently evaluated according to their fitness and the most promising children are included in the pool of parents and replace parent genomes with a lower fitness. If this strategy were strictly followed, no new "genetic information" could enter the algorithm. Furthermore, a certain beneficial combination of genes that is once deleted may never return in a later step. Nature's solution to this problem – mutation – is also applied within the GA. Each gene of the child generation may flip with a certain probability after mating.

When no new offspring with a higher fitness is produced, the pool of parents is considered converged and the genome with the best cross-validation score represents the optimal set of clusters. To avoid ending up in a local minimum, several runs of the GA may be executed in parallel originating from different starting populations. Furthermore, the mutation probability may be increased drastically after a certain number of generations, according to the so-called "lock-out strategy".

The genetic algorithm is able to answer the two questions asked above, namely to identify important effective interactions and determine how many of them are needed for a predictive fit. In the program code UNCLE, which was used throughout this work, the user may adjust several parameters, such as the size of the starting population, the number of children produced, the mutation probability, the number of generations and the maximum number of included clusters. This way, a well-converged fit with high predictive power can be ensured. The way that the GA is implemented in UNCLE is described in References [161, 181].

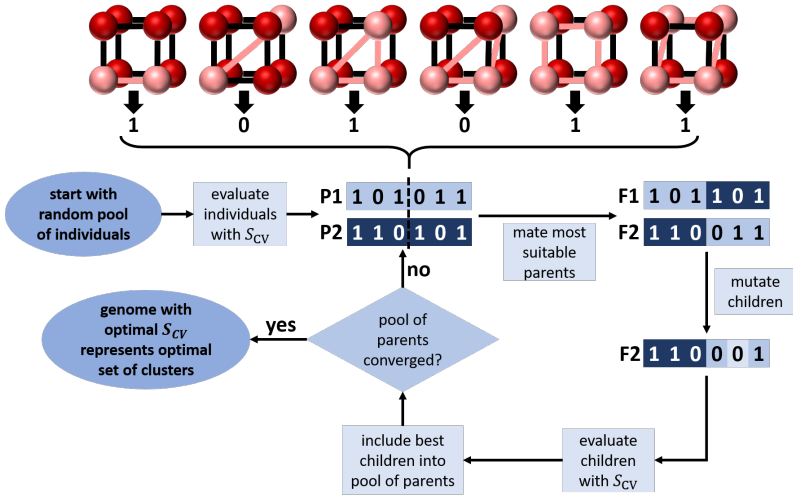


Figure 4.7.: Schematic illustration of the genetic algorithm that is employed to determine relevant interaction energies (adapted from Reference [175]).

4.2.3. Ground-state search

Nevertheless, the GA only represents the inner loop of the actual cluster expansion. It is important to note that the obtained effective interaction can only be as good as the set of input structures allows. Therefore, the input database is also updated and improved iteratively. This outer loop is illustrated via a flow chart in Figure 4.8.

At the beginning of the CE, the input structures consist of a small number of atomic configurations (typically around 20) that have been calculated by means of DFT. They may contain the "usual suspects" – derivative structures of the parent lattice with small unit cells – and random structures [175]. In UNCLE, special program routines read in the input structures and check whether their atoms lie on the pre-defined crystal lattice and whether there are equivalent structures. At this point, it is worth mentioning that the input energy values correspond to the fully relaxed geometries instead of the rigid lattice. The influence of the relaxation on the energetics is therefore included in the calculated interactions. Problems may arise for systems with very strong deviations from the original atomic positions, which result in a loss of the actual lattice symmetry or a change into another lattice structure.

Based on the initial input set, the effective interactions are determined

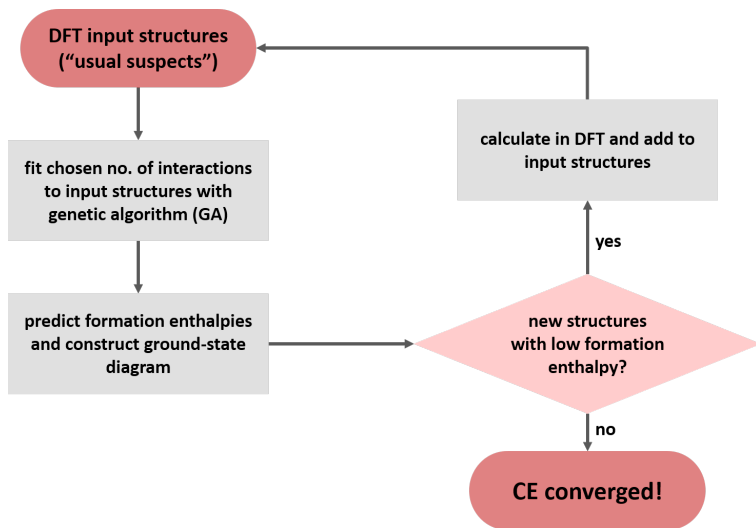


Figure 4.8.: Schematic illustration of the self-consistent outer look of the cluster expansion.

via the GA and they are employed to predict the total energies and thereby formation enthalpies of the whole configuration space. An efficient exhaustive enumeration algorithm [187–189] implemented in UNCLE identifies and enumerates all possible configurations up to a number of atoms within the unit cell that the user can specify. Furthermore, it is possible to include only structures within a certain concentration range of interest. Thereby, it is sufficient to optimize the fit for these concentrations and there is no need to include input structures from the whole concentration range. In addition, a detailed search with large cell sizes and small concentration steps can be performed.

Already at this stage of the CE, a so-called ground-state diagram is plotted (see Figure 4.9). This diagram shows the resulting formation enthalpies ΔH_f against the concentration of one of the elements. Importantly, it allows identifying thermodynamically stable configurations (at that respective temperature) by constructing the ground-state line, i.e. the convex hull around the data points. Mathematically, it is defined in the following way for three possible structures – α , σ and β – which are the energetically most favorable at their respective concentration x and have the concentration hierarchy

$$x(\alpha) < x(\sigma) < x(\beta):$$

$$\Delta H_f(\sigma) < \frac{x(\sigma) - x(\beta)}{x(\alpha) - x(\beta)} \Delta H_f(\alpha) + \frac{x(\sigma) - x(\alpha)}{x(\beta) - x(\alpha)} \Delta H_f(\beta) \quad (4.24)$$

Out of the newly predicted structures, those that are on the ground-state line or close to it (so-called "excited states") and that are not yet included in the input set are then calculated by means of DFT and added to the input structures. Thereby, the input database is systematically increased and the fit quality for the structures of interest, namely the energetically favorable ones, is gradually improved. The cluster expansion is considered converged when the ground-state lines calculated by DFT and the one obtained from the CE fit coincide, and no new ground states are predicted. Typically, the input set for a fully converged CE contains around 100 to 150 DFT input structures.

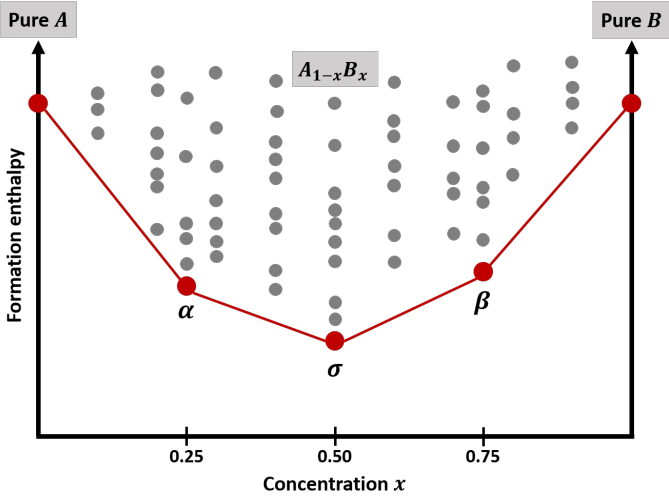


Figure 4.9.: Schematic illustration of a ground-state diagram. The ground-state line, which here contains five ground states, is depicted in red. The gray points represent other possible and energetically less favorable configurations (adapted from Reference [160]).

4.2.4. Surface cluster expansions

Cluster expansions are not restricted to the bulk, but may also be performed for surfaces, for example to identify favorable adsorption sites or to study surface segregation. For the latter, usually, a certain number of surface layers is defined, in which the atoms can be occupied by either species. Thus, configuration and concentration near the surface are varied and can be analyzed. In this case, however, the effective interactions J become layer-dependent (see Figure 4.10), as most surfaces undergo local relaxations along the surface normal, or even reconstruct. Consequently, the degeneracy of certain figures, which were symmetrically equivalent in the bulk, is lifted. A larger number of effective interactions and also input structures may thus be required for a well-converged surface CE [160].

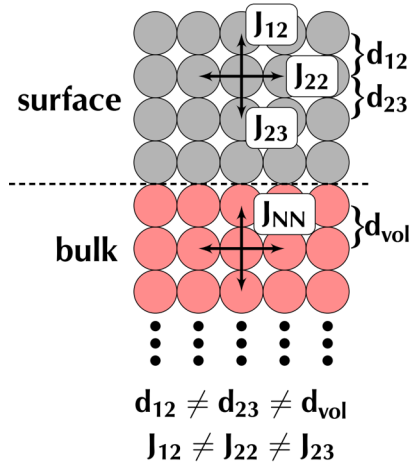


Figure 4.10.: Effective interactions close to the surface are layer-dependent and therefore, the symmetry of figures that are equivalent in the bulk is lifted.

4.2.5. Monte Carlo simulations

For many problems, knowing a system's properties at $T = 0$ K is not enough, and entropic contributions at higher temperatures have to be simulated. In DFT, this may be realized by determining phonon spectra and their contribution to the total energy via perturbation calculations. The phonon contributions can even be included in a cluster expansion, yielding temperature-

dependent effective interactions [190]. However, this requires phonon calculations for all input structures at every temperature step, leading to very high computational cost even for bulk systems.

To obtain trends for order-disorder temperatures or short-range order parameters, for instance, it is often sufficient to account for configurational entropy, which may be calculated in Monte Carlo simulations. The configurational entropy represents a part of a system's entropy that is related to the number of possible arrangements of the constituents, such as different types of atoms on a crystal lattice. In the present work, canonical Monte Carlo simulations⁷ were carried out employing a parallelized version of the classical metropolis algorithm [191, 192] implemented in UNCLE. Basically, the simulations follow this three step process for a binary alloy system containing atoms of types A and B:

1. Select randomly a pair of A and B atoms and flip their positions.
2. Calculate the energy difference δE caused by exchanging the two atoms. If $\delta E > 0$, accept the flip; if $\delta E < 0$, accept the flip with a probability of $\text{expt}(-\delta E/kT)$.
3. Determine the mean change in total energy ΔE averaged over the last number $N \gg 1$ of steps. If ΔE is larger than a given convergence parameter, repeat the process.

In UNCLE, the size of the simulation cell – typically 40^3 to 60^3 atoms – and the concentration of the elements are specified. The total energy of each configuration is then calculated with the Hamiltonian obtained from the CE. A temperature schedule dictates the start and end temperatures and cooling or heating step sizes within predefined temperature ranges. Ideally, a narrow step size is chosen for temperature ranges where phenomena of interest, such as an order-disorder transition, are expected. At the end of the simulations, the total energy at each temperature step as well as the atomic configuration of the simulation cell are obtained.

⁷Canonical means that the concentration of elements was kept fixed, while for grand-canonical simulations, a particle exchange across the system borders may take place and change the concentration.

4.3. Low-energy electron diffraction (LEED)

The present work combines theoretical calculation and an experimental verification of the structure of the Ag-Au (111) surface via low-energy electron diffraction (LEED). In this section, a short summary of the theoretical background of LEED and an introduction to tensor LEED is given. Most of the information on the theoretical aspects is taken from sources by Rous [193], Heinz et al. [194] and Heinz [195]. The reader is encouraged to consult these sources for a more detailed description.

4.3.1. Theoretical background

Historically, the application of low-energy electron diffraction (LEED) goes back to the 1920s, when in 1924, L. de Broglie introduced the wavelike nature of all particles and their characteristic wavelength as the quotient of Planck's constant and their linear momentum. Only three years later, in 1927, C. Davisson and L. Germer [196] reported diffraction patterns created by low-energy electrons diffracted from a crystalline nickel sample. Shortly afterwards, diffraction experiments with high-energy electrons at metal foils by G.P. Thomson and A. Ried [197] followed. Davisson and Thompson shared the Nobel Prize in 1937 for their experimental discovery of the diffraction of electrons by crystal lattices. However, a quantitative structure determination via LEED was only carried out several decades later due to difficulties in the interpretation of the diffraction patterns and peak intensities. Unlike for X-ray diffraction, which was realized by M. von Laue in 1912 and W. L. Bragg in 1913, the low-energy electrons interact very strongly with the atoms within the first surface layers and the layer distances close to the surface may not be equal to those in the bulk due to surface relaxation. Therefore, the kinematic theory of diffraction did not suffice to perform a LEED structure analysis, but the dynamical approach accounting for multiple and strong scattering as well as surface relaxation and electron attenuation in the material had to be applied.

The above mentioned strong scattering of the low-energy electrons results in a relatively small mean free path and the desired surface sensitivity of the method. As the first few atomic layers usually extend about $5 - 10 \text{ \AA}$ into the surface, the electron energy is typically chosen in a range of $25 - 600 \text{ eV}$ to ensure a mean free path of the electrons in the same dimension. These

energy values correspond to an electron wavelength of about $0.5 - 2.5 \text{ \AA}$, which is slightly smaller than most lattice parameters of solids. Applying Bragg's law for diffraction, the angles between incident and diffracted beams may be determined via $\sin \alpha_n = n \lambda/a$. For the low-energy electrons, these angles are large enough to obtain well-resolved diffraction patterns, which is one prominent advantage of the LEED method. Another benefit lies in the rather simple and inexpensive experimental setup. Figure 4.11 schematically illustrates the basic setup for a 3-grid optics LEED system in UHV. An electron gun sends the almost monoenergetic primary beam towards the mounted sample, which should be prepared in a way that it features a flat and well-defined surface. The primary electron beam then interacts with the first atomic layers of the samples and elastically scattered diffracted beams travel towards a hemispheric luminescent screen, where the diffraction pattern may be directly observed. Each of the three grids serves a different purpose: The innermost grid is at the same potential as the sample to ensure that the diffracted electrons are not distorted on their way to the screen. A suppressor voltage on the second grid eliminates unwanted secondary or inelastically scattered electrons, which would impair the obtained diffraction pattern. A high voltage of several kV between the outermost grid and the luminescent screen post-accelerates the diffracted electrons, resulting in bright diffraction spots that can easily be analyzed.

For the first LEED experiments, the current of the diffracted electron beams was measured using a Faraday cup. However, in order to obtain as much information as necessary to carry out a complete structure analysis of a surface, the angle of incidence or (more commonly) the energy of the primary beam are varied. For a varying energy, both the diffraction spot intensities and their location change. Therefore, the experimental setup using a fluorescent screen and a camera tracking the diffraction spots in a video is very convenient. The intensity of each spot may then be traced and digitalized, so that the full intensity versus energy ($I(E)$) spectrum is obtained. These spectra change rapidly for only slight changes in the angle of incidence of the primary electron beam. As a consequence, this angle should be very well adjusted and known to perform a reliable structure analysis.

If the primary electron beam is approximated as an ideal plane wave of unity amplitude, i.e. by $\exp(i\vec{k}_0 \cdot \vec{r})$, and the surface is assumed to be perfectly flat with structurally identical unit cells, the total diffraction intensity I can

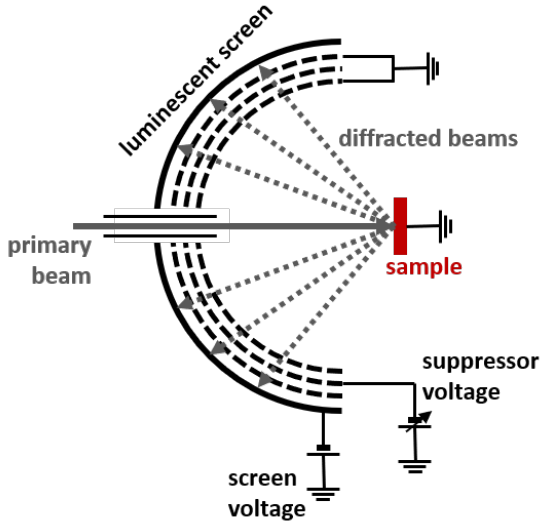


Figure 4.11.: Schematic view of the LEED experimental setup with three grids.

be written as follows:

$$I = |A|^2 = |f(\vec{k}_0 \cdot \vec{k}_f)|^2 \cdot \left| \sum_{m,n} e^{-i\Delta\vec{k}\vec{r}_{mn}} \right|^2 = F \cdot G, \quad (4.25)$$

where A is the amplitude, \vec{k}_0 and \vec{k}_f are the wave vectors of the primary and diffracted beams, respectively, and r_{mn} defines the origins of the periodically repeated unit cells. The two factors in equation (4.25) are called lattice factor G and form or structure factor F , respectively. While G contains information on the translational symmetry and the size and shape of the unit cell, F describes the arrangement of the atoms within the unit cell.

When \vec{r}_{mn} is written in terms of the real-space unit cell vectors \vec{a}_1 and \vec{a}_2 , i.e. $\vec{r}_{mn} = m\vec{a}_1 + n\vec{a}_2$, the lattice factor G may be decomposed in two components as follows:

$$G = \left| \sum_m e^{-im\Delta\vec{k}\vec{a}_1} \right|^2 \cdot \left| \sum_n e^{-in\Delta\vec{k}\vec{a}_2} \right|^2. \quad (4.26)$$

The lattice factor G is only non-zero, when the Laue condition is met:

$$\Delta\vec{k} \cdot \vec{a}_i = 2\pi j \quad (j = -\infty \dots \infty). \quad (4.27)$$

The vectors $\Delta\vec{k} = \vec{g}$, which fulfill this criterion, are called reciprocal lattice vectors. As \vec{a}_1 and \vec{a}_2 lie within the surface plane, every normal component of \vec{g} is allowed, while the two components in the surface are defined as:

$$\vec{g}_1 = 2\pi \frac{\vec{a}_2 \times \vec{n}}{|\vec{a}_1 \times \vec{a}_2|} \quad \text{and} \quad \vec{g}_2 = 2\pi \frac{\vec{n} \times \vec{a}_1}{|\vec{a}_1 \times \vec{a}_2|}, \quad (4.28)$$

where \vec{n} is the surface normal. As a consequence, the reciprocal lattice is made up of parallel rods with the lateral periodicity of the reciprocal unit cell. A very convenient way to visualize the Laue condition within the reciprocal lattice is the construction of the Ewald sphere. Thereby, possible elastically scattered beams that experience constructive interference in the crystal may be identified. Figure 4.12 illustrates the Ewald spheres for a smaller and a larger wave number k , respectively. To begin, the incident wave vector \vec{k}_0 is drawn to point at the origin of the reciprocal lattice. Due to energy conservation in elastic scattering processes, \vec{k}_0 and \vec{k}_f must have the same magnitude and define the radius of the so-called Ewald sphere. The Laue condition for constructive interference is fulfilled only on interceptions between the Ewald sphere and the reciprocal lattice rods. This also illustrates why incoming beams with too large wavelengths (and thereby too small wave numbers) are not diffracted in the crystal, as the Ewald sphere is too small to intercept with the reciprocal lattice.

As mentioned above, the structure factor F from equation (4.25) contains information on the arrangement of atoms within the unit cell and their scattering properties. In electron scattering, the atoms have a rather large scattering cross section as compared to X-ray scattering, and therefore electrons are scattered multiply. Unlike the lattice factor, F is dominated by this multiple scattering.

The $I(E)$ (intensity vs. energy) spectra obtained in LEED measurements contain numerous peaks, which arise from the layers normal to the surface taking part in the electron scattering. Due to the strong scattering, electrons are attenuated and atoms in deeper layers contribute less than those close to the surface. This electron attenuation causes a decrease in the peak height in the spectra and can be included in the LEED analysis by adding a complex

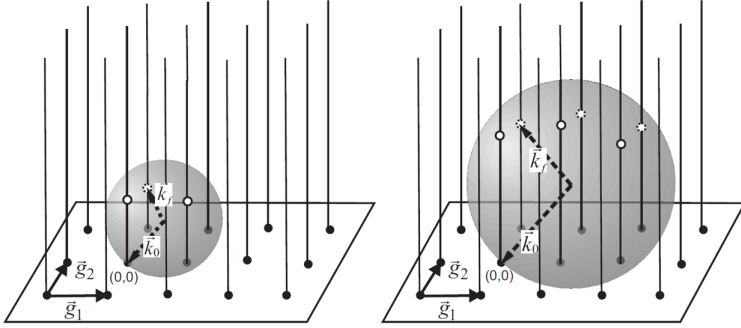


Figure 4.12.: Construction of the Ewald sphere for a smaller (left) and a larger (right) wave number k . From Wandelt, *Surface and Interface Science, Volume 1*. Copyright ©2014 by John Wiley Sons, Inc. Reprinted by permission of John Wiley & Sons, Inc.

energy $V_0 = V_{0r} + iV_{0i}$ to the vacuum energy E_V of the electron, so that the total energy of the electron within the crystal amounts to $E = E_V + V_0$. Here, V_0 is called the inner potential and V_{0i} is the optical inner potential. The latter describes the inelastic losses of the electron flux and for a LEED analysis, typically values of $|V_{0i}| = 4 \dots 6 \text{ eV}$ are employed.

In reality, the layer distances close to the surface is not constant, but for most materials, the first few layers relax inward the surface. Smaller layer distances correspond to smaller wavelengths needed for constructive interference, which causes a peak shift to higher energies in the LEED spectra. In addition to surface relaxation, at finite temperatures, atoms also vibrate around their equilibrium positions and thereby deviate from the ideal translational symmetry. This causes a weakening of the diffraction spot intensities according to the Debye-Waller factor:

$$DWF = e^{-(\Delta \vec{k} \vec{u})^2}, \quad (4.29)$$

where \vec{u} defines the atomic vibrations around the equilibrium position. The residual intensity appears as thermal diffuse background in the LEED spectra. It is important to notice for any structure analysis that the lattice vibrations in the surface layer are usually larger than in the bulk due to fewer atomic bonds.

Not only phenomena in the surface of the sample, but also the experimental

setup cause deviations from the ideal LEED spectra. For example, the primary electron beam possesses a finite energy width and angular width caused by the thermal emission of the electrons from the cathode and the finite size of the emitting area. As a result, the diffraction spots are broadened.

As already mentioned above, the strong and multiple scattering in LEED experiments is not sufficiently well described by kinematic theory, but must be treated dynamically. This also becomes obvious looking at the obtained spectra: Dynamical LEED spectra contain more and broader peaks that vary in height. Furthermore, peaks may appear that are actually canceled in the kinematic calculation of the structure factor F . A fully dynamical LEED structure analysis is typically divided into three steps:

1. Compute the scattering contributions of the single atoms.
2. Combine the atomic scattering to calculate the dynamical diffraction of the atomic layers.
3. Combine the layers to obtain the dynamical diffraction of the whole surface.

The scattering potential of the single atom contains contributions of the nucleus, the core electrons and an exchange-correlation term. As an approximation, one may neglect the weak scattering of the outer electrons and assume the scattering potential as spherical. Therefore, the total incoming wave function is expanded in a set of spherical waves and upon scattering at the spherical atomic potentials, the angular momentum quantum number l is conserved. The Schrödinger equation is then solved inside and outside the scattering atom. The atomic scattering potential imposes a phase shift δ_l on the outgoing wave. In a LEED analysis, the number of angular momenta l and the according phase shifts δ_l which have to be included in the calculation increases with the electron energy and is typically given by $l_{\max} \approx kR$, where R is the radius of the atomic scattering potential. Another important quantity is the atomic scattering factor $t(k, \Phi)$, which gives the atomic scattering in different directions. Figure 4.13 presents $t(k, \Phi)$ for four different elements and shows that forward scattering is dominant except for very weak scatterers like hydrogen. As a rule of thumb, the atomic scattering strength and anisotropy both increase with the atomic number Z , which results in the chemical sensitivity of LEED.

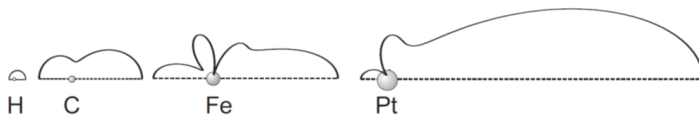


Figure 4.13.: Angular dependence of the scattering factor $t(k, \Phi)$ for four different elements at constant electron energy. From Wandelt, *Surface and Interface Science, Volume 1*. Copyright ©2014 by John Wiley Sons, Inc. Reprinted by permission of John Wiley & Sons, Inc.

In the second step, the atomic scattering potentials are assembled into layers in a muffin-tin potential, meaning a spherical potential in the muffin-tin region and a constant potential in the interstitial space. The incoming wave is then developed in terms of spherical waves in order to match the atomic scattering from above and afterwards, the sum of diffracted spherical waves is again developed in back and forward diffracted plane waves. In that step, it is important to account also for intralayer diffraction, where atoms may scatter back to themselves within an atomic layer. Calculating the layer diffraction is therefore done self-consistently and represents the most time-consuming calculation step in a fully dynamical LEED analysis.

In the last step, the atomic layers are stacked up to obtain the scattering of the whole surface. Here, multiple interlayer diffraction must be considered. Layer diffraction is conveniently described in terms of reflection and transmission matrices, which allow to easily compute diffraction of a double layer starting from a single layer and of a quadruple layer starting from a double layer (layer doubling method).

After the theoretical $I(E)$ curves have been calculated, they need to be compared to the experimental spectra to judge whether the calculated structure matches the real one. The human eye fails to do a reliable comparison, especially when there are many possible similar structures involved. It is important to note that large and small maxima are equally important and also the minima need to be considered. This evaluation is done with the so-called reliability factor or R-factor. The most commonly employed R-factor is the Pendry R-factor [198], R_P , which uses a function $Y(E)$ of the logarithmic derivatives of the intensities $L = (dI/dE)/I(E)$ instead of directly comparing

the intensities:

$$R_P = \frac{\sum_{hk} \int_E [Y_{hk}^e xp(E) - Y_{hk}^{calc}(E)]^2 dE}{\sum_{hk} \int_E [Y_{hk}^e xp(E) + Y_{hk}^{calc}(E)]^2 dE} \quad \text{with} \quad Y(E) = \frac{L(E)}{1 + [V_{0i}L(E)]^2}, \quad (4.30)$$

where the sum is over all beams and the integral over the electron energy range of the experiment and calculation. A total agreement between experimental and theoretical spectra would result in an R-factor of $R_P = 0$, while the maximum value, $R_P = 2$, indicates anticorrelated spectra and uncorrelated spectra yield $R_P = 1$. Nowadays, structural analyses with R-factors below $R_P = 0.1$ have been reported, which indicates excellent agreement between experimental and theoretical data (see, for example, References [199–201]). Assuming statistical errors with a Gaussian probability distribution, the variance of the Pendry R-factor can be calculated as

$$var(R_P) = R_P \sqrt{\frac{8V_{0i}}{\Delta E}}, \quad (4.31)$$

where ΔE is the energy database accumulated over all beams. This value can then be added as the limits of error $\pm \Delta p_i$ to the R-factor R_P .

4.3.2. Tensor LEED

One major drawback of the conventional fully dynamical LEED analysis is that it is a trial and error procedure. The calculated spectra are compared to experimental ones and evaluated via their R-factors and the full calculation needs to be carried out for each candidate surface structure, even though the obtained spectra vary only slightly in many cases. To overcome this problem, a technique called tensor LEED has been developed. It was inspired by the simplicity of x-ray diffraction, where x-rays are assumed to propagate in empty space and the atomic scattering represents a weak perturbation. The situation is more complex for LEED, as it features dynamical and strong scattering. Therefore, instead of vacuum, a reference surface structure is taken as a starting point [202] and it is calculated fully dynamically. Sufficiently small structural changes may then be treated via first-order perturbation theory. The scattering factor for the perturbed structure t'_j is then written as if there was no structural change:

$$t'_j = t_j + \delta t_j (\delta \vec{r}_j), \quad (4.32)$$

where t_j is the scattering factor of the reference structure and $\delta\vec{r}_j$ denotes the displacement of the atom. There is no general rule for how big this displacement may be for the approximation of first-order perturbation to be valid, as this depends on the structure under investigation. The perturbation is, however, not restricted to displacements, but may also be a variation of vibrational amplitudes of the atoms [203] or chemical composition [204]. For the latter, the scattering matrices are replaced by composition-weighted average matrices, so that the composition of each layer may be varied separately. This is very convenient for segregation studies at surfaces.

In this work, the tensor LEED approach has been employed within the program package TensErLEED developed in Erlangen by Blum and Heinz [205]. Figure 4.14 illustrates how a LEED structure analysis is carried out in TensErLEED. First of all, a promising model has to be identified as a reference structure, which represents the starting point of the analysis. This model may, for example, emerge from theoretical predictions, such as DFT calculations. For this structure, a fully dynamical intensity calculation is performed and the LEED amplitudes and wave field components are stored for each atom and beam. In a next step, a suitable set of parameters that are to be varied is chosen. These may include geometrical and thermal displacements and variation of the chemical elements. The LEED amplitude changes caused by these distortions are then calculated for each atom. Via perturbation theory, the $I(E)$ spectra are obtained for all possible combinations and compared to the experimental spectra by calculating the R-factor.

The search algorithm applied in TensErLEED to identify the best fit structure was introduced by Kottcke and Heinz [206]. After an initial set of trial structures is randomly chosen from all possible solutions, each structure develops individually towards a local minimum. In this process, new structures are chosen around the previous ones according to a Gaussian probability distribution (PD). If the R-factor of the new one is lower, it replaces the old structure. Conveniently, the width of the PD decreases with the R-factor. Whenever a certain amount of the trial structures (commonly around 20%) have reached the same parameter set with minimum R-factor, the search stops automatically. This way, the global minimum may be identified and at the same time, information is gained about other local minima, which may be interesting for the final evaluation of the structure analysis. Finally, if the best fit structure deviates too strongly from the reference structure, it is

chosen as the new reference structure and the procedure is repeated.

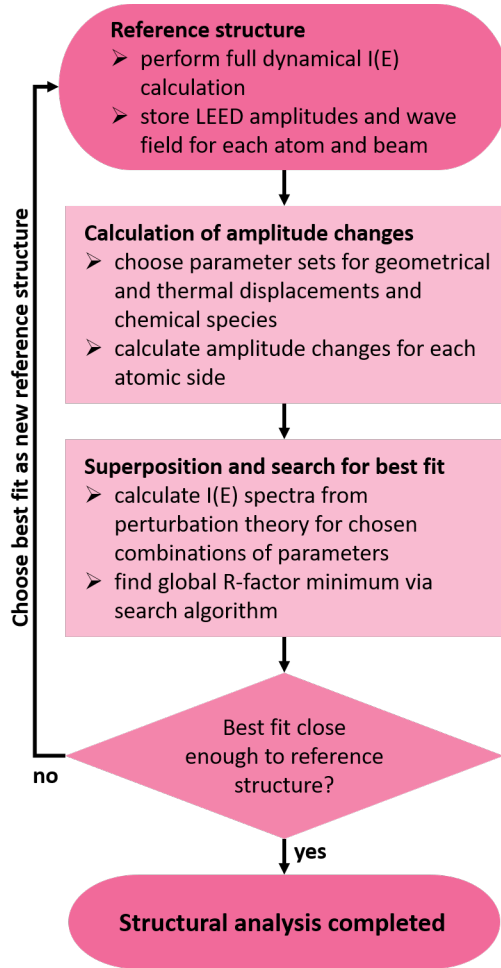


Figure 4.14.: Flow chart of the structure analysis process in TensErLEED.

A number of input parameters have to be provided by the user. First of all, the electron energy range as well as the crystal lattice parameters have to be defined. To calculate the atomic scattering, one has to choose the maximum of the angular momentum quantum number. While it depends on the element and also on the energy range, the estimate mentioned above of $l_{max} \approx kr_{mt}$, where r_{mt} is the muffin tin radius, usually represents a good

assumption. For the calculations in plane wave space, a list of beams to be used as basis set must be provided. The layer doubling scheme is employed to generate the underlying bulk structure and the actual surface layers are then defined with the respective interlayer distances. In order to determine the amplitude changes, a list of thermal and geometrical distortions must then be given for each atomic site within the surface layers and the chemical species are defined via an occupation probability.

Surface segregation at Ag-Au surfaces

"God made the bulk; surfaces were invented by the devil."

- *Wolfgang Pauli*

As already mentioned in Chapter 2, residual silver from the dealloying process in nanoporous gold (npAu) is reported to influence its catalytic performance and potentially play a crucial role in certain reaction steps. In this chapter, the question about the location of these silver atoms within the npAu surface is addressed. For this purpose, the surface segregation at model Ag-Au surfaces was investigated via a combined approach of density functional theory (DFT) calculations and a cluster expansion (CE). Both a flat and a stepped surface were analyzed in their adsorbate-free (clean) state, as well as in the presence of adsorbed oxygen at the surface.

5.1. Bulk reference

Before dealing with surfaces, important considerations and information on the pure elements silver and gold as well as the Ag-Au alloy system are given here.

5.1.1. Pure elements

At the beginning of every DFT investigation, bulk calculations for all pure elements under consideration are performed to obtain their stress-free lattice parameters. This step is important to avoid internal stresses within the surface slabs that might influence the results for the surface properties. Since Ag-Au surfaces are the focus of this work, the bulk properties of the Ag-Au system have been thoroughly investigated. First, the equilibrium lattice parameters of Ag and Au were determined for several different exchange-correlation functionals and compared to theoretical and experimental values from the literature (see Table 5.1). For this purpose, bulk calculations were performed in the primitive unit cell (face-centered cubic, space group Fm3m) with a Γ -centered Monkhorst-Pack grid of $31 \times 31 \times 31$ k-points. The interaction between valence electrons and ionic cores was described via projector augmented wave method (PAW) pseudopotentials, and a cutoff energy of 725 eV and Methfessel-Paxton smearing with a smearing width of 0.2 eV were employed.

As can be seen in table 5.1, PBE strongly overestimates the lattice constant compared to experimental values, while LDA slightly underestimates it. A very good agreement between calculated and experimental lattice parameters is achieved for PBEsol, which is a revised version of the PBE functional that is especially suitable for densely-packed solids and their surfaces. The relative deviation between calculated and experimental values amounts to only 0.8% for Ag and 0.1 – 0.2% for Au, respectively.

Furthermore, van der Waals (vdW) interactions may be included in the exchange-correlation functional via different approaches. Originally designed to improve theoretical results for single atoms or molecules in gas phase and adsorbates on surfaces, these functionals have proven to also perform very well for bulk systems. A prominent example for vdW-corrected functionals is the D3 correction by Grimme et al., where the total energy is calculated as the sum of the self-consistent Kohn-Sham energy from DFT E_{DFT} and a dispersion energy term E_{D3} :

$$E_{\text{DFT+D3}} = E_{\text{DFT}} + E_{\text{D3}} \quad (5.1)$$

The dispersion energy term E_{D3} is obtained from a sum over two-body and three-body terms, where the dispersion coefficients vary with chemical

Table 5.1.: Equilibrium lattice parameters a_0 for the pure elements Ag and Au calculated with different exchange-correlation functionals and compared with literature values. The present results are marked by an asterisk.

a_0 [Å]		Method	Reference
Ag	Au		
4.003	4.052	LDA	*
4.145	4.156	PBE	*
4.052	4.081	PBEsol	*
4.211	4.197	revPBE	*
4.090	4.121	opt86b-vdW	*
4.130	3.996	PBE+D2	*
4.073	4.099	PBE+D3	*
	4.066	FP-LMTO, LDA	[207]
4.02	4.07	USPP, GGA	[44]
4.086	4.072	XRD (293 K)	[208]
4.086	4.078	experimental (298 K)	[97]

environment. This represents a great improvement compared to the previous D2 correction, which provided constant fixed dispersion coefficients for each element. More detailed information can be found in References [209, 210].

For both Ag and Au, the D3 correction together with the PBE functional yields equilibrium lattice constants that are in excellent agreement with experimental values at room temperature. The obtained relative deviations are only 0.3% and 0.5 – 0.7% for Ag and Au, respectively.

5.1.2. Ag-Au alloy

The Ag-Au system has a very simple phase diagram with complete miscibility over the whole concentration range. However, short-range order patterns obtained from Monte Carlo simulations and diffuse X-ray scattering experiments indicate an ordering tendency at low temperatures [211–213]. Lu et al. [213] employed DFT-LDA calculations combined with a cluster expansion and obtained the three ground states $L1_2$, $L1_0$ and $L1_2$ at silver concentrations of $x_{\text{Ag}} = 25\%$, $x_{\text{Ag}} = 50\%$ and $x_{\text{Ag}} = 75\%$, respectively. In a next step, they calculated order-disorder phase transition temperatures via the Monte Carlo method and the cluster variation method (CVM) and compared their results to theoretical values from the literature. For the three ground states, the values ranged between about 100 – 240 K. According to the authors, the

slow diffusion rates at these low temperatures may inhibit direct growth into the ordered phase.

Figure 5.1 shows the ground-state diagram obtained from a bulk cluster expansion for the Ag-Au system. Including around 90 DFT-LDA input structures and 35 clusters for the GA fit, the cross-validation score of $S_{CV} = 0.1 \text{ meV}$ indicates high predictive power. Each of the bright red crosses represents a fully relaxed geometry up to a cell size of 20 atoms. While there are numerous structures close to the ground-state line, the three prominent ground states and their formation enthalpies ΔH_f are consistent with the reported results from the literature [213, 214] L1₂ (AgAu₃), L1₀ (AgAu) and L1₂ (Ag₃Au). Their configuration is illustrated in Figure 5.1 below the ground-state diagram.

5.2. Selection of suitable surface orientations

Nanoporous gold (npAu) consists of nano-sized entangled gold ligaments in a sponge-like structure. By means of first principles calculations with periodic boundary conditions – like the DFT calculations performed in this work – it is practically impossible to model the highly curved npAu surface. Instead, model surfaces have to be chosen to represent the npAu topography as realistically as possible. Fujita et al. [37] conducted a high-angle annular dark-field (HAADF) transmission electron microscope (TEM) study and they describe the npAu surface as close-packed (111) and (100) terraces separated by atomic steps. They estimate the total area of the two surface orientations to be inversely proportional to their respective surface energies $\gamma_{(hkl)}$. Considering that $\gamma_{(111)} = 94.9 \text{ meV } \text{\AA}^{-2} < \gamma_{(100)} = 112.3 \text{ meV } \text{\AA}^{-2}$ [215], the (111) surface may be regarded as the dominating surface at the terraces.

To capture a combination of flat facets and steps, two surface orientations were chosen in this work for an investigation of the segregation behavior at Ag-Au surfaces: the densely-packed (111) surface and the stepped (321) surface (see Figure 5.2). It has been shown experimentally and theoretically that the (111) surface reconstructs into the so-called Herringbone structure with a $22 \times \sqrt{3}$ unit cell [216–219]. Such large structures are not feasible for DFT calculations, and much less for a cluster expansion, where numerous input structures have to be included. Interestingly, experimental work on thin-film gold electrodes [220, 221] suggests that the unreconstructed Au

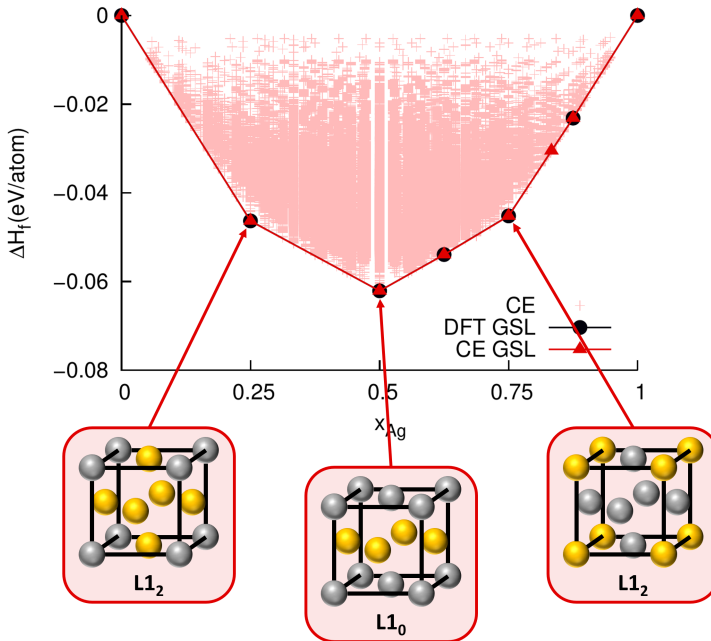


Figure 5.1.: Ag-Au ground-state diagram. Every bright red cross corresponds to a fully relaxed geometry. The two ground-state lines obtained via DFT and CE coincide and indicate a fully converged CE. The three prominent ground states $L1_2$ ($AgAu_3$), $L1_0$ ($AgAu$) and $L1_2$ (Ag_3Au) are depicted below the diagram.

(111) surface may occur in the case of small structures, like they are present on the npAu surface. These findings, together with computational efficiency, make the flat Au (111) surface suitable for the present work.

The Au (321) surface provides a combination of several interesting features which are also present on the npAu surface: narrow and flat (111) terraces separated by zigzag-shaped atomic steps, yielding a large number of Au surface sites with low and high coordination. This is also of particular interest for catalysis, since according to Fujita et al. [37], residual Ag provides reactive sites close to steps and kinks within the surface, as it suppresses the (111) faceting. The present work may shed light on the location of silver atoms in the stepped (321) surface.

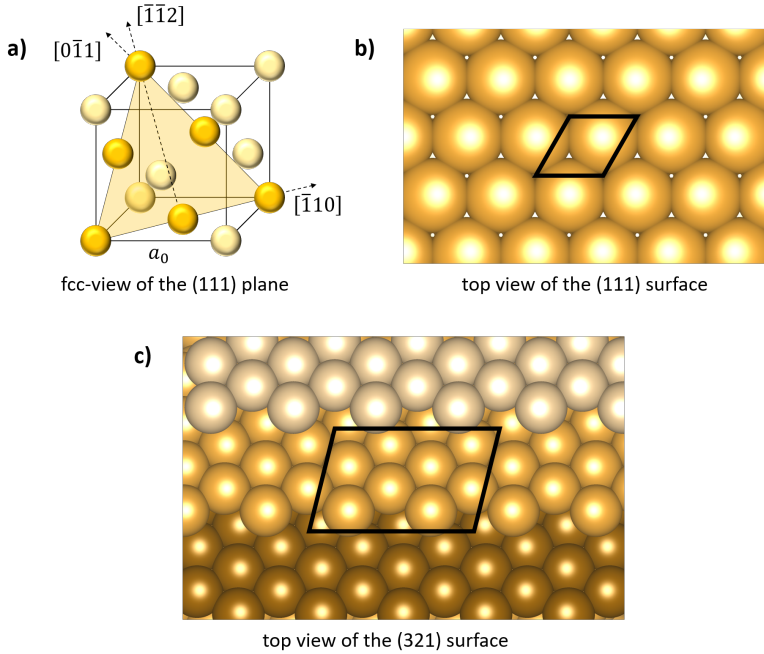


Figure 5.2.: Illustration of the Au (111) and (321) surfaces: a) fcc view of the (111) plane with the principal directions $[\bar{1}\bar{1}0]$ and $[\bar{1}\bar{1}2]$, b) top view of the Au (111) surface, the 1×1 unit cell is indicated in black, c) top view of the Au (321) surface, the 2×1 unit cell is indicated and the (111) terraces are depicted in different shades of gold.

By selecting the two surface orientations mentioned above, it is possible to tackle the question of how the segregation behavior of residual silver that was left after the dealloying process is influenced by the surface topology. In addition to the clean surfaces, the effect of adsorbed oxygen on the segregation profile was also considered in this work. However, before focusing on surface segregation, the properties of the clean (111) and (321) surfaces will be discussed in the following subsection.

5.3. Surfaces of pure elements

5.3.1. Surface energy

As already mentioned in Chapter 3, two parameters that may generally influence the segregation behavior are the lattice constant mismatch and the difference in surface energies. Regarding the equilibrium lattice constants, they are nearly the same for Ag and Au and their values are reproduced very well by several exchange-correlation functionals, such as LDA, PBEsol and PBE-D3. Nevertheless, a wrong hierarchy in the surface energies may lead to wrong results for the segregation analysis. Therefore, in this work, the surface energies of both the Ag and the Au (111) surfaces were calculated for various exchange-correlation functionals and compared to literature values.

Generally, the presence of surfaces always is energetically less favorable than the bulk material, because otherwise the bulk material would simply disintegrate. The surface energy may thus be regarded as the work required to build a certain area of surface. Following the direct approach¹, the surface energy γ was calculated as follows:

$$\gamma = \frac{1}{2A_{\text{slab}}} \left(E_{\text{slab}} - \frac{N_{\text{slab}}}{N_{\text{bulk}}} E_{\text{bulk}} \right), \quad (5.2)$$

where A_{slab} is the area of the modeled surface within the surface slab, E_{slab} and E_{bulk} are the total energies of the slab and bulk calculations, respectively, and N_{slab} and N_{bulk} are the total numbers of atoms within the surface slab and the bulk reference cell, respectively. The factor 2 originates from the fact that symmetric surface slabs were employed here, resulting in two surfaces within the simulation cell. These symmetric Ag and Au (111) surface slabs included 12 atomic layers in ABC-stacking, where two layers in the middle were bulk layers, which remained fixed during the calculation. Five layers on each side of the bulk layers were considered surface layers and allowed to relax until the forces on the atoms reached a value below 0.01 eV/Å. The same smearing parameters, cutoff energy and k-point density as for the bulk calculations were employed, except there was only one k-point along the

¹In DFT, the surface energy may be calculated via two different approaches: a direct one, where the energy of a bulk reference is subtracted from that of the surface, and so so-called FM-approach (Fiorentini and Methfessel). For the latter, the energies for bulk and surface are obtained from surface calculations with an increasing number of layers, making a bulk reference obsolete. The direct approach was chosen in the present work, as numerous surface calculations are computationally less efficient than small bulk reference cells.

Table 5.2.: Surface energies of the Ag and Au (111) surfaces in comparison to literature values from theory and experiment. All energies are given in meV \AA^{-1} and J m^{-2} . The present results are marked by an asterisk.

γ_{Ag}		γ_{Au}		Method	Reference
meV \AA^{-1}	J m^{-2}	meV \AA^{-1}	J m^{-2}		
71.3	1.14	69.6	1.12	LDA	*
45.5	0.73	43.7	0.70	PBE	*
62.5	1.00	52.5	0.84	PBEsol	*
33.8	0.54	31.6	0.51	revPBE	*
67.9	1.09	68.7	1.10	opt86b-vdW	*
81.8	1.31	162.1	2.60	PBE+D2	*
83.8	1.34	88.9	1.42	PBE+D3	*
68.2	1.09	55.3	0.89	EAM	[222]
69.9	1.12	100.5	1.61	TB-LMTO	[223]
73.2	1.17	80.1	1.28	FCD-GGA	[224]
73.0	1.17			MP-PP LDA	[225]
		46.7	0.74	PBE	[226]
		64.9	1.04	MB-PP LDA	[217]
82.4	1.32	96.1	1.54	Experiment	[227]

surface normal. The results, compared to literature values derived from theory and experiment, are given in Table 5.2.

Looking at the surface energies for Ag and Au calculated in this work, it is evident that the values strongly differ depending on the choice of exchange-correlation functional. Also the literature values show discrepancies, though there is good agreement between the reported LDA and PBE results with the present results employing the same functionals. Tyson et al. [227] extrapolated the surface energies for various metals from experimental data at higher temperatures. However, their values represent an average over the most occurring low-index surfaces and therefore cannot be directly compared to the other results in Table 5.2.

Nevertheless, the qualitative trends from experimental and most theoretical results – except for the EAM values – indicate that gold possesses a higher surface energy than silver. This hierarchy is not reproduced by most functionals from the present work in Table 5.2, except for PBE plus either of the two vdW-corrections D2 or D3. The D2 corrections yields a lattice parameter mismatch of 3.4%, which is much larger than the experimentally observed one of about 0.34%. Furthermore, the surface energy of Au for the

D2 correction is twice as large as the one of Ag. The D3 correction, however, leads to a lattice constant mismatch of only 0.6% and a slightly higher surface energy for Au than for Ag. Adding the D3 dispersion correction term to the self-consistent total energy obtained from PBE reportedly leads to values close to experimental values for bulk properties as well as surfaces with adsorbed species [209, 210]. Additionally, a theoretical study by Rehr et al. [228] indicates that the contribution of polarization forces to the cohesive energies of Ag and Au amounts to 14% and 17%, respectively. For these reasons, the PBE functional with additional D3 correction was chosen for all further calculations in this work.

5.3.2. Surface relaxation

The creation of a surface leads to a dangling bonds for the atoms within the surface layer and a resulting redistribution of the electron density. Usually, for fcc metal surfaces, an inward relaxation is reported. Nevertheless, certain surfaces, like the Au (111) surface, exhibit an outward relaxation. Table 5.3 presents the results for the relaxation of the topmost layer distances obtained in this work for different exchange correlation functionals for the Au (111) and the Au (321) surface. The relative change in layer distance in percentage δ_{ij} between layers i and j is defined as follows:

$$\delta_{ij} = 100 \cdot \frac{d_{ij} - d_{\text{bulk}}}{d_{\text{bulk}}}, \quad (5.3)$$

where d_{ij} is the layer distance between layers i and j and d_{bulk} is the equilibrium layer distance along the direction of the surface normal within the bulk. Positive values indicate an outward relaxation, while a negative sign means inward relaxation.

For the (111) surface, the topmost three layer distances are shown, as the following layer distances are already bulk-like again. All chosen functionals – except for the D2 correction – show very good agreement with theoretical values from the literature, with an outward relaxation of the first layer and a slight inward relaxation of the second one.

For the (321) surface, the analysis was slightly more complicated. Since it is difficult to divide it in layers, each two atoms having the same height within the (2×1) unit cell were considered as a layer. This definition led to very small layer distances of around and less than 0.5 Å and large relative changes

in δ_{ij} . Though the magnitudes differ slightly for the employed exchange-correlation functionals, the trend indicates contraction of the atoms at the step edges and an expansion of those underneath. To the best of the author's knowledge, no results on the relaxation of the Au (321) surface have been reported in the literature so far, so that only present results are given in Table 5.3.

Table 5.3.: Surface relaxation of the topmost three and six layer distances for the Au (111) and the Au (321) surfaces, respectively. Results from the present work are marked by an asterisk.

	δ_{12}	δ_{23}	δ_{34}	δ_{45}	δ_{56}	δ_{67}	Method	Ref.
Au (111)	+0.5	-0.4	+0.0				LDA	*
	+1.0	-0.5	-0.1				PBE	*
	+0.7	-0.4	+0.0				PBEsol	*
	+1.3	-0.4	-0.2				revPBE	*
	+1.0	-0.4	-0.1				opt86b-vdW	*
	+2.7	-0.2	-0.1				PBE-D3	*
	+4.7	+0.5	+0.2				PBE-D2	*
	+0.8	-0.3	+0.0				MB-PP LDA	[217]
	+0.4	-0.3	-0.2				USPP LDA	[229]
	+1.7	+0.0	+0.2				PBE	[230]
	+0.0	-1.9	-1.4				PBE	[226]
+1.3	-0.9	+0.2				PW91	[218]	
Au (321)	-32.1	-16.3	-17.1	+7.3	+29.0	-12.8	LDA	*
	-31.7	-19.4	-17.8	+9.9	+29.9	-13.2	PBE	*
	-31.0	-19.0	-15.9	+9.3	+26.3	-12.7	PBEsol	*
	-31.6	-15.5	-16.3	+4.7	+30.7	-10.2	revPBE	*
	-30.9	-20.3	-12.4	+10.0	+24.6	-12.7	opt86b-vdW	*
	-32.6	-20.5	+3.4	+19.5	+20.4	-17.0	PBE-D2	*
	-36.9	-28.9	-3.8	+19.1	+26.4	-18.0	PBE-D3	*

5.4. Results on surface segregation

In this section, the results on the surface segregation at four selected Ag-Au surfaces are presented: the adsorbate-free (111) surface, the (111) surface with adsorbed atomic oxygen, the adsorbate-free stepped (321) surface and the (321) surface with an infinite oxide chain. Before presenting the segregation results, necessary computational details will be explained. A detailed list of VASP input parameters can be found in the Appendix A.

5.4.1. Clean Ag-Au (111) surface

Computational details

The Ag-Au (111) surfaces were modeled in asymmetric (2×2) surface slabs containing 24 atoms in six atomic layers and a vacuum region of $\approx 18 \text{ \AA}$ to separate the upper and lower surfaces of the periodically repeated slabs (see Figure 5.3). A dipole correction [158, 159] in the direction of the surface normal was used to achieve faster convergence of the total energy with increasing vacuum thickness, and to correct for the electrostatic potential within the vacuum region. The six atomic layers were divided in two bulk layers, which were kept fixed during the calculations, and four surface layers, which were allowed to relax in two subsequent steps until the forces acting on the ions reached a value smaller than 0.007 eV/\AA . For the bulk layers, three different Ag concentrations were chosen to investigate the influence of the underlying bulk type on surface segregation: pure Au bulk ($x_{\text{Ag}} = 0\%$), the $L1_2$ structure, as it represents the ground state with the smallest Ag concentration at very low temperatures in the Ag-Au phase diagram [214] ($x_{\text{Ag}} = 25\%$), and pure Ag bulk ($x_{\text{Ag}} = 100\%$). By interpolation, the lattice parameter for the $L1_2$ ordered bulk structure would be 4.0923 \AA . However, literature reports a negative deviation from Vegard’s law for the Ag-Au system and a contraction of the lattice that is caused by the additional Ag atoms [231]. Therefore, the equilibrium lattice parameter for $L1_2$ with $x_{\text{Ag}} = 25\%$ was obtained from a Murnaghan fit from bulk calculations using the four-atom $L1_2$ unit cell. The resulting value of 4.088 \AA corresponds to a negative deviation of about 0.1% from Vegard’s law, which is in good agreement with an experimental study by Lubarda [231]. The converged k-point grid for bulk calculations was adapted to the surface slab unit cell vectors and a set of $21 \times 21 \times 1$ k-points was employed for all (111) surface calculations.

To realize different Ag surface concentrations and to create input structures for the cluster expansions, the Ag concentration within the four surface layers was varied from 0% to 100% , with 0% corresponding to pure gold and 100% corresponding to all the beige atoms in Figure 5.3 occupied by silver. The chosen slab geometry with 16 atoms in the surface layers resulted in a concentration step size of 6.25% with a total of $2^{16} = 65536$ possible atomic configurations. An algorithm implemented in UNCLE identified symmetrically equivalent structures and eliminated them, thereby reducing the

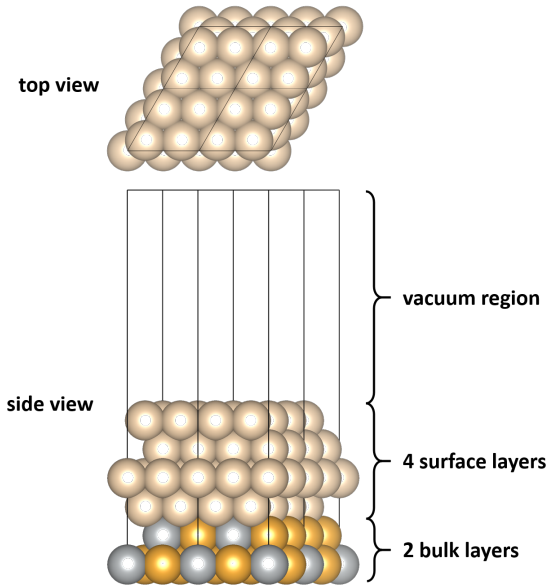


Figure 5.3.: Top and side view of the Ag-Au surface slab with L_{12} bulk structure. The slab consists of two bulk layers and four surface layers (beige), which may be occupied by either Ag or Au for the cluster expansion. Au atoms are depicted in gold, Ag atoms in silver. The (2×2) unit cell is indicated. Reproduced from Ref. [232] with the permission of AIP Publishing.

number of configurations considerably.

In total, three cluster expansions for the three different Ag bulk concentrations were carried out for clean (i.e. adsorbate-free) Ag-Au (111) surfaces. The resulting values for the cross-validation score S_{CV} and the respective number of input structures necessary to obtain a stable expansion are presented in Table 5.4. The values of around and well below 1 meV for S_{CV} indicate a good fit quality.

Segregation results

Based on the performed cluster expansions, the respective surface stability diagrams were constructed. The latter are similar to the ground-state diagram from Figure 5.1, but instead of the classical formation enthalpy, the surface formation enthalpy ΔH_f^{surf} is displayed over the Ag surface concentration within the four surface layers $x_{\text{Ag}}^{\text{surf}}$. For a structure σ , ΔH_f^{surf} is

Table 5.4.: Number of DFT input structures and cross-validation score S_{CV} for the clean Ag-Au (111) surfaces.

Bulk type	No. of input structures	S_{CV} [meV]
Au	125	0.95
Ag	128	1.14
L1 ₂	103	0.15

defined as follows:

$$\Delta H_f^{\text{surf}}(\sigma) = E^{\text{slab}}(\sigma) - x_{\text{Ag}}^{\text{surf}} E_{\text{Ag}}^{\text{slab}} - x_{\text{Au}}^{\text{surf}} E_{\text{Au}}^{\text{slab}}, \quad (5.4)$$

where $E^{\text{slab}}(\sigma)$ is the total energy per atom of structure σ and $E_{\text{Ag}}^{\text{slab}}$ and $E_{\text{Au}}^{\text{slab}}$ correspond to the total energies per atom of surfaces with pure Au and Ag surfaces, irrespective of the underlying bulk structure. $x_{\text{Ag}}^{\text{surf}}$ and $x_{\text{Au}}^{\text{surf}}$ are the respective surface concentration of Ag and Au within the uppermost 16 atoms of the surface slab (beige in Figure 5.3).

The surface stability diagram for the clean Ag-Au (111) surface with L1₂ bulk structure is depicted in Figure 5.4. Below the diagram, five example ground-state configurations are shown in top and side views for different Ag surface concentrations $x_{\text{Ag}}^{\text{surf}}$. To make them easier to distinguish, only every third CE data point was included in the diagram. Each of them corresponds to a fully relaxed surface geometry. The two ground-state lines from DFT input data (black) and CE fit (red) coincide, which indicates a well-converged CE.

Interestingly, the resulting ground-state structures suggest moderate Au segregation to the topmost layer and Ag enrichment in the second topmost layer. At the smallest possible Ag surface concentration of $x_{\text{Ag}}^{\text{surf}} = 6.25\%$, the energetically most favorable position of the Ag atom is within the sub-surface layer. With an increasing number of Ag atoms, the third and fourth layer adapt the L1₂ ordered bulk structure. The ground state at $x_{\text{Ag}}^{\text{surf}} = 25\%$ – i.e. corresponding to the bulk concentration – is Au-terminated and enriched with Ag in the subsurface layer. Up to Ag surface concentrations of $x_{\text{Ag}}^{\text{surf}} = 31.25\%$, this Au termination prevails for the energetically most favorable structures. With only one Au atom present in the four surface layers ($x_{\text{Ag}}^{\text{surf}} = 93.75\%$), this atom is located within the surface layer for the ground state.

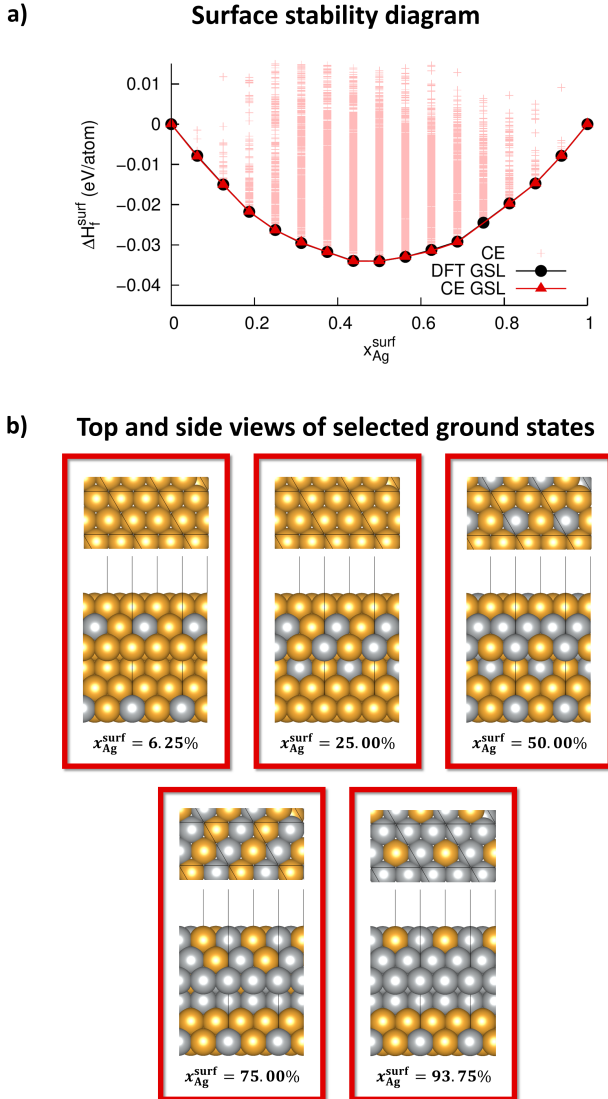


Figure 5.4.: Surface stability diagram for the clean Ag-Au (111) surface with two $L1_2$ bulk layers and four surface layers (a). Below, five example ground-state structures are depicted in top and side views (b). The surface unit cell is indicated.

Nevertheless, the values for the surface formation enthalpies up to $\Delta H_f^{\text{surf}} \approx 35$ meV are quite small. Entropic contributions may lead to fluctuations that result in different atomic structures already at room temperature. Furthermore, the chosen size of the unit cell naturally limits the concentration step size within one layer to 25%, which is rather coarse. Unfortunately, increasing the size of the unit cell leads to very long calculations times and is not feasible to create CE input structures. However, to test whether a smaller concentration step size within the layers would alter the Au-terminated ground state, four test calculations were performed for a (4×1) unit cell, i.e. twice as large and including 48 atoms. All four structures had a silver surface concentration of $x_{\text{Ag}}^{\text{surf}} = 25\%$. One Ag atom was placed within the surface layer at four different atomic sites, corresponding to a surface layer silver concentration of $x_{\text{Ag}}^{\text{layer}} = 12.5\%$, while the subsurface layer contained three Ag atoms ($x_{\text{Ag}}^{\text{layer}} = 37.5\%$). The third and fourth layer had bulk-like $L1_2$ ordered structure. Even though the differences in total energies amounted to only a few meV/atom, the Au-terminated structure remained the energetically most favorable configuration.

The surface stability diagrams resulting from the cluster expansions for pure Au bulk and pure Ag bulk, respectively, are very similar to the one presented in Figure 5.4. A pure gold bulk structure leads to almost the same ground-state configurations as the ones obtained for $L1_2$ bulk. For pure Ag bulk, however, the Au segregation to the topmost layer is slightly less pronounced. The surface stability diagrams as well as example ground-state configurations for pure Au and Ag are given in the Appendix B. Figure 5.5 illustrates the silver concentration $x_{\text{Ag}}^{\text{layer}}$ within the topmost surface layer (red) and within the subsurface layer (black) as a function of the silver surface concentration $x_{\text{Ag}}^{\text{surf}}$ for the three different bulk types. A gray line with a slope equal to one is included to guide the eye. Any data point on this line would correspond to the absence of segregation, as the amount of Ag atoms within the four surface layers would be uniformly distributed. The results presented in the diagram clearly indicate a Au enrichment in the topmost layer and a Au depletion in the subsurface layer. Yet, the Ag concentration within the bulk layers seems to have little influence on the segregation behavior.

Interestingly, the present results stand in contrast to previous experimental and theoretical studies dealing with surface segregation in Ag-Au, as reported in Chapter 3. From segregation models considering the lattice pa-

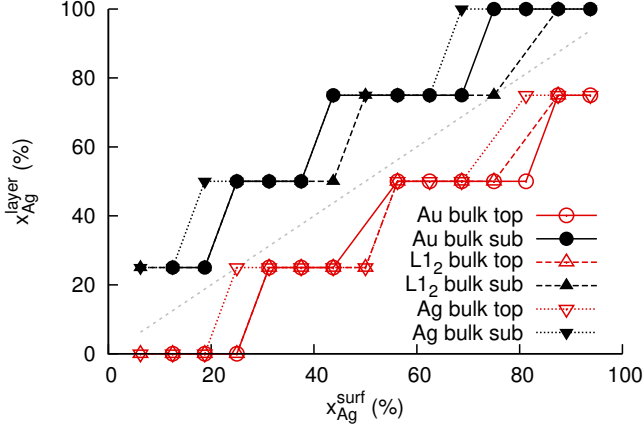


Figure 5.5.: Surface segregation profile for the adsorbate-free Ag-Au (111) surface with three different bulk structures: pure Au, $L1_2$, and pure Ag. The Ag concentration in the surface and subsurface layer is shown in red and black, respectively. A line with a slope equal to one (corresponding to the absence of segregation) is included in gray to guide the eye. Reproduced from Ref. [232] with the permission of AIP Publishing.

parameter mismatch and the difference in surface energies, Ag segregation to the topmost layer might be expected. In order to rule out any effect of the choice of the exchange-correlation functional on the obtained results, test cluster expansions for PBE, PBE-D2 and revPBE input structures were carried out. They did not include as many input structures and were not fully converged, but the segregation trends could be used for comparison. While PBE and revPBE yield Au enrichment in the topmost layer and to some extent the same ground-state configurations as PBE-D3, PBE-D2 leads to a reversed segregation behavior and Ag enrichment in the surface layer. Even though the PBE-D2 results would reproduce previous results from the literature, the D2 correction reportedly performs worse than D3 in almost all applications [210]. Also regarding the present study, D2 gives a very large lattice mismatch of 3.4% (see Table 5.1) and a much larger difference in surface energies than all other employed functionals (see Table 5.2). Thus, the PBE functional plus D3 correction was retained for all further calculations.

Consequently, the question arises why a Au enrichment in the surface is energetically favorable as compared to Ag surface segregation. Consulting the

literature, a similar phenomenon was described by Dianat et al. [114], who analyzed the segregation behavior of bimetallic Co-Cr and Pt-Pd surfaces by means of DFT calculations. For the Pt-Pd system, they report Pd surface segregation for low Pt bulk concentrations and Pt enrichment in the surface layer for higher Pt bulk concentrations. Intuitively, however, one would always expect a Pd-enriched surface layer, since Pd possesses the lower surface energy than Pt. Dianat et al. [114] explain their findings by a charge transfer from Pd to the more electronegative Pt, leading to an increased filling of the *d*-bands of the Pt surface atoms. They refer to a model originally proposed by Friedel [119, 223], which states that the surface energy of a metal decreases with increasing filling of the *d* orbital for metals with more than half-filled *d*-bands.

The electronic configuration of gold is $5d^{10}6s^1$ and thus the *d* orbital is already filled. For this reason, the model by Friedel [119, 223] does not seem to be applicable in this case. However, relativistic effects play an important role for the electronic structure of gold and its properties. With an increasing atomic number, the electrons in the *s* orbitals experience a stronger acceleration by the core, making them faster and – according to relativity – heavier. These relativistic effects cause the *6s* orbital to contract and stabilize [233]. As a consequence, the *s*-electrons are bound to the core more strongly and shield the nuclear charge from the other electrons, such as the *d*-electrons. In gold, this results in an expansion and a destabilization of the *5d* and a reduction of the *s-d* energy gap, which again leads to the characteristic yellowish color [234].

Regarding the interpretation of the present results, due to relativistic effects, the destabilized *5d* orbital of Au may be regarded as not entirely filled and a charge transfer from Ag to the more electronegative Au may thus take place. In addition, the values for the electronegativity on the Pauling scale for Au and Ag (2.54 and 1.93, respectively) reveal a much larger difference than for Pt and Pd (2.28 and 2.20, respectively), which should promote a charge transfer. This possibility was explored by analyzing two test surface configurations with $L1_2$ bulk structure and a) a pure Au surface and Ag subsurface layer and b) a pure Ag surface and Au subsurface layer. The calculated surface energy for the Au-terminated surface is slightly smaller than that of the Ag-terminated surface ($\gamma = 0.98 \text{ eV}/\text{\AA}^2$ and $\gamma = 1.04 \text{ eV}/\text{\AA}^2$, respectively). To determine the amount of charge associated with each atom, a Bader anal-

ysis [115–117] was employed. In this popular tool, zero flux surfaces, i.e. surfaces on which the charge density is at a minimum value perpendicular to the surface, are used to divide atoms. The charge that is enclosed in this so-called Bader volume typically represents a good approximation to the total charge associated to this atom. The resulting Bader charges revealed an excess charge of $-10e/\text{atom}$ (where e corresponds to the elementary charge) within the surface layer of the Au-terminated structure, while the Ag subsurface layer has a positive charge of $+0.16e/\text{atom}$. In contrast to that, the Ag-terminated surface has a positive excess charge of $+0.05e/\text{atom}$ within the Ag surface layer and a negative charge of $-0.07e/\text{atom}$ in the Au subsurface layer. The Bader charges of the pure metal (111) surface have also been determined to rule out the possibility that the calculated surface layer charges originate merely from the topology. The calculations showed that both the Au and the Ag (111) surfaces are slightly negatively charged with $-0.02e/\text{atom}$. Supposedly, this topological effect also contributes to the excess charges of the test configurations reported above. It may explain the smaller magnitude of the positive charge within the Ag surface layer compared to the magnitude of the negative excess charge within the surface layer of the Au-terminated structure.

In a next step, the Bader excess charges of the surface and subsurface layers were determined for several ground states obtained in the CE for the Ag-Au (111) surface with $L1_2$ bulk (see Table 5.5). The negative excess charge within the surface layer of about $-0.04e/\text{atom}$ remains constant with an increasing Ag surface concentration. Only for the two values $x_{\text{Ag}}^{\text{surf}} = 25\%$ and $x_{\text{Ag}}^{\text{surf}} = 50\%$, the magnitude of the negative excess charge is larger with $-0.06e/\text{atom}$. Looking at Figure 5.5, these two values for $x_{\text{Ag}}^{\text{surf}}$ differ from the other data points as well regarding the Ag layer concentration: For $x_{\text{Ag}}^{\text{surf}} = 25\%$ and $x_{\text{Ag}}^{\text{surf}} = 50\%$, the difference in $x_{\text{Ag}}^{\text{layer}}$ between the surface and the subsurface layer is 50%. For all other values of $x_{\text{Ag}}^{\text{surf}}$, this difference is only 25%. Hence, the two quantities of Bader excess charge and Ag surface layer concentration appear to be correlated. Presumably, a larger difference in Ag concentration between the surface and subsurface layer results in a larger negative charge transfer from the subsurface to the surface layer, which lowers the surface energy.

To visualize the charge distribution in a Au-terminated and a Ag-terminated surface, charge density difference plots were calculated for the two test struc-

Table 5.5.: Bader charges of the surface and subsurface layer of various ground states resulting from the CE for the adsorbate-free Ag-Au (111) surface with L1₂ bulk structure.

$x_{\text{Ag}}^{\text{surf}}$	Bader charge [e/atom]	
	Surface layer	Subsurface layer
6.25	-0.04	0.06
12.50	-0.04	0.04
25.00	-0.06	0.07
37.50	-0.04	0.04
50.00	-0.06	0.08
68.75	-0.04	0.04
75.00	-0.04	0.06
87.50	-0.04	0.06

tures mentioned above (see Figure 5.6). The colors represent the difference between the valence charge density resulting from a self-consistent calculation in VASP and the superposition of the atomic charges, which can be obtained in VASP by simply not updating the electron density during the calculation. In the pictures, only positive values are shown, corresponding to an increase in charge density compared to the superposition of atomic charge densities. The dark blue areas within the surface indicate the positions of the atoms, where a charge depletion occurs, which is not shown here.

Clearly, there is a larger charge accumulation within the surface layer for the Au-terminated (111) surface (seen as dark red areas) compared to the Ag-terminated surface. However, the charge density in the subsurface layer is smaller for the Au-terminated surface, illustrating the charge transfer from the Ag subsurface to the more electronegative Au surface layer.

To summarize, moderate Au segregation to the topmost surface layer was obtained for the adsorbate-free Ag-Au (111) surface, practically independent of the Ag bulk concentration. A potential connection was established to previous theoretical results for surface segregation in Pt-Pd, where the unexpected Pt surface enrichment was explained by a charge transfer from Pd to Pt. It has been demonstrated that this charge transfer from the less to the more electronegative element also occurs in Ag-Au surfaces, possibly lowering the surface energy and making Au within the surface layer energetically favorable. Interestingly, the present results stand in contrast to previous experimental and theoretical results reporting Ag surface segregation. Two

possible reasons may lead to this discrepancy: First, the aforementioned results from the literature may originate from pre-adsorbed oxygen at the alloy surfaces, causing silver to migrate to the surface layer. Second, the chosen experimental and theoretical methods may not have been suitable for exclusively measuring the topmost surface layer. To shed more light on this phenomenon, a low energy electron diffraction (LEED) analysis was performed in the frame of this work. The details and results are given in Chapter 7.

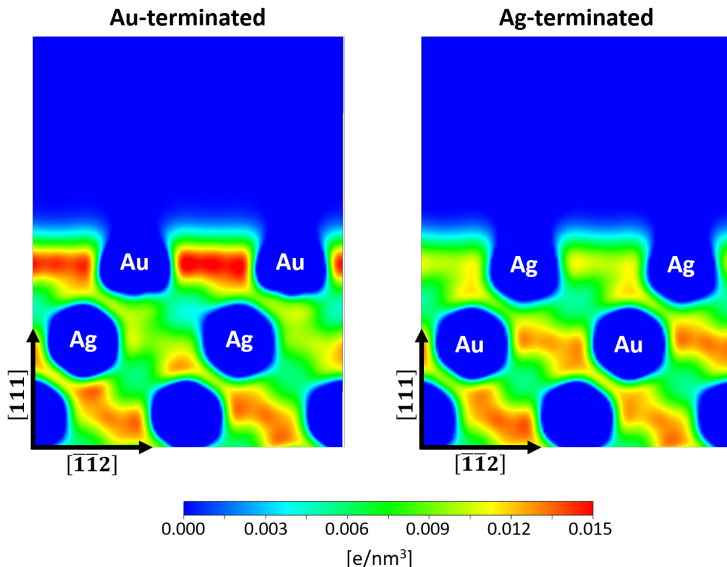


Figure 5.6.: Charge density difference between the valence charge densities resulting from a self-consistent VASP calculation and the superposition of the atomic charges for a Au-terminated (left) and a Ag-terminated (right) surface. The surface normal and the direction along the surface and the position and type of the surface atoms are indicated.

5.4.2. O-covered Ag-Au (111) surface

Computational details

Since nanoporous gold (npAu) offers great potential for catalytic applications, it is crucial to study the behavior of gold surfaces in the presence of an electrolyte or reactive gas. In the catalytic cycle for the self- and cross-coupling

reactions of primary alcohols on npAu (see Figure 2.2), atomic or molecular oxygen is provided, which binds to the npAu surface and remains available for further reaction steps. On the one hand, this is a significant part of the catalytic cycle, and on the other hand, an adsorbed species may influence the surface composition and the segregation behavior. The importance of adsorbate-induced ordering and surface segregation has already been discussed in the literature for various alloy systems and adsorbate species (see for example References [235–238]). In order to gain insight into this phenomenon for Ag-Au surfaces, the effect of adsorbed atomic oxygen at the Ag-Au (111) surface on the energetically preferred positions of the Ag atoms was studied in this work.

While the Au (111) surface seemingly represents the prototypical inert metal surface, the adsorption of oxygen on it has been a controversial subject of several previous experimental and theoretical studies (see for example References [239–243]). By means of first principles calculations, Shi et al. [240] conducted a thorough analysis of oxygen adsorption and surface oxide formation on the Au (111) surface. Their results suggest that up to a coverage of 0.25 ML (monolayer), on-surface chemisorption on fcc hollow sites is preferred over subsurface adsorption. However, according to their calculations, on-surface oxygen is only metastable even at low temperatures, while the most favorable configurations involve the formation of a very thin surface-oxide-like structure. Baker et al. [241] combined *ab initio* molecular dynamics (MD) with high-resolution electron energy loss spectroscopy (HREELS) to analyze the influence of dosing temperature and coverage on the adsorption of molecular oxygen at the Au (111) surface. At low temperatures of 200 K, they found that the majority of the adsorbed oxygen is on-surface chemisorbed at low coverages, while at high coverages, the surface oxide dominates.

As the present work does not deal with the exact adsorption geometry, but simply with the effect of an adsorbate on surface segregation, the same (2×2) surface unit cell as for the adsorbate-free surface with $L1_2$ ordered bulk was chosen, with an O atom on the fcc hollow site (see Figure 5.7). This corresponds to a coverage of 0.25 ML. According to Shi et al. [240], this configuration is only slightly less favorable than the thin surface-oxide-like structures they identified as energetically most favorable. At the same time, the present choice offers the advantage of a much smaller unit cell,

which is a great advantage for CE input calculations. All DFT parameters were the same as for the clean surface in Section 5.4.1. In the surface CE, the configuration of the upper 16 atoms (beige in Figure 5.7) was varied in the same manner, while the oxygen atoms were kept at the fcc hollow sites for all structures. The cross-validation score of $S_{CV} = 0.25\text{eV}$ for 98 input structures indicates a very good fit quality.

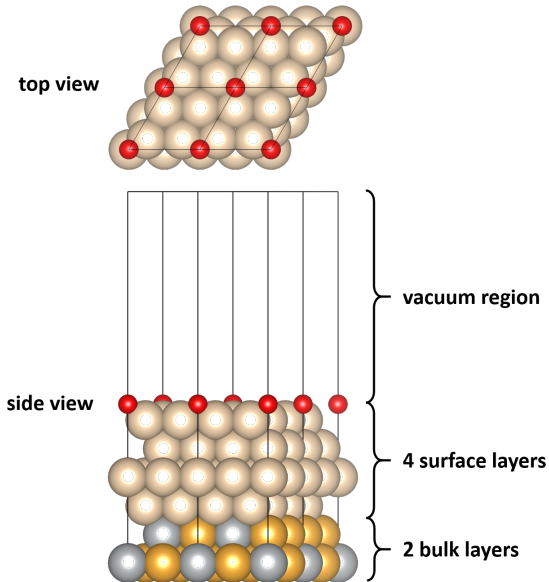


Figure 5.7.: Side and top views of the Ag-Au (111) surface with adsorbed atomic O on the fcc hollow site. Au atoms are depicted in gold, Ag in silver, and O in red. The uppermost four layers (beige) were allowed to be replaced by Ag or Au in the CE input calculations. The (2×2) surface unit cell is indicated. Reproduced from Ref. [232] with the permission of AIP Publishing.

Before dealing with surface segregation, however, adsorption energies were determined with respect to the free oxygen atom for the aforementioned slab for all surface atoms occupied by gold ($x_{\text{Ag}}^{\text{surf}} = 0\%$) and for the L1₂ structure in all layers of the slab ($x_{\text{Ag}}^{\text{surf}} = 25\%$). As a reference, the adsorption energy for the pure gold (111) surface was also calculated. In Table 5.6, the obtained values are compared to results from the literature. In DFT, adsorption energies may be calculated as follows:

$$E_{\text{ad}} = E_{\text{tot}} - (E_{\text{surf}} + E_{\text{adsorbate}}), \quad (5.5)$$

where E_{tot} refers to the total energy of the surface with the adsorbate, E_{surf} is the energy of the clean surface and $E_{\text{adsorbate}}$ represents the energy of the adsorbate, which may be a single atom or a molecule.

The lowest adsorption energy was obtained for the pure Au (111) surface, followed by the Au-terminated Ag-Au (111) surface, while the Ag-terminated Ag-Au (111) surface yielded the largest value for E_{ad} . Generally, the present results are in good agreement with the literature values, especially with the DFT results from slab calculations obtained by Shi et al. [240] and Pessoa et al. [242]. The experimental value from thermal programmed desorption (TPD) is somewhat smaller, but the PBE functional and also the D3-correction are known to overestimate binding energies, leading to a higher adsorption energy.

Table 5.6.: Adsorption energy for chemisorbed oxygen on the fcc hollow site at the pure Au (111) surface and Ag-Au (111) surfaces. For comparison, theoretical and experimental literature results for the pure Au (111) surface are also given. Values are given in eV and with respect to the free oxygen atom. Present results are marked by an asterisk.

Substrate	E_{ad} [eV]	Method	Reference
Au (111)		DFT-PBE-D3	*
Ag-Au (111) Ag-term.	3.96	DFT-PBE-D3	*
Ag-Au (111) Au-term.	3.28	DFT-PBE-D3	*
Au (111)	3.25	DFT-GGA (slab)	[240]
Au (111)	1.26	DFT-B3LYP (cluster)	[242]
Au (111)	2.16	DFT-PW91 (cluster)	[242]
Au (111)	3.08	DFT (slab)	[242]
Au (111)	2.77	DFT-PBE (slab)	[243]
Au (111)	2.43	TPD	[244]

Segregation results

The segregation profile of the adsorbate-free Ag-Au (111) surface with L1₂ bulk structure clearly changes in the presence of an adsorbed oxygen atom in an fcc hollow site. Figure 5.8 presents the surface stability diagram obtained from the CE (a) and four example ground-state configurations at different

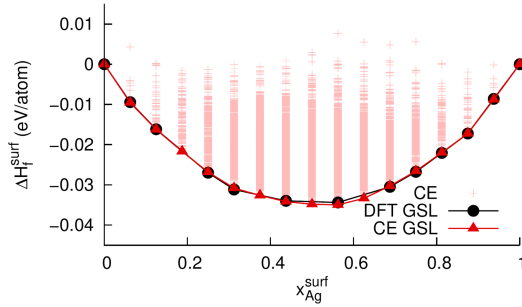
Ag surface concentrations in top and side views (b). Like in Figure 5.4, only every third data point of the CE output is included. The magnitude of the surface formation enthalpy remains practically unaltered as compared to the adsorbate-free surface. Yet, the energetically most favorable structures exhibit a very different distribution of Ag and Au atoms within the four surface layers with a pronounced silver segregation to the topmost layer.

For the lowest possible Ag surface concentration $x_{\text{Ag}}^{\text{surf}} = 6.25\%$, the preferred location of the Ag atom is within the topmost surface layer. At $x_{\text{Ag}}^{\text{surf}} = 12.5\%$, the Ag concentration in the topmost surface layer already amounts to 50%. A pure Ag surface layer for all ground states is obtained for a Ag surface concentration equal to or higher than $x_{\text{Ag}}^{\text{surf}} = 68.75\%$.

Analogous to Figure 5.5, the surface segregation profile for the Ag-Au (111) surface covered by 0.25 ML of atomic oxygen and L1₂ bulk structure is depicted in Figure 5.9. However, it reveals the reverse segregation behavior for this case, with strong Ag enrichment in the topmost layer (red) and moderate Ag depletion in the subsurface layer (black). Seemingly, the effect of the charge transfer stabilizing Au in the topmost layer for the adsorbate-free surface is much smaller than the pull of the strongly electronegative O on the Ag atoms. To characterize the charge distribution, a Bader analysis was performed for the obtained ground states. All of the latter were shown to have a strong negative excess charge at the O atom of approximately 0.75 e/atom and a positive excess charge within the surface layer of 0.2 e/atom. This adsorbate-induced re-segregation has been discussed in the literature for several bimetallic systems [245, 246]. It can be explained by a stronger interaction of the adsorbate with surface sites occupied by one of the constituting metals (here: silver), than with the other metal (here: gold).

Interestingly, the nearest neighbors of the O atom of the ground state at $x_{\text{Ag}}^{\text{surf}} = 6.25\%$ are Au atoms, and the Ag atom with the topmost layer is not located next to the O atom (see Figure 5.8b). However, this ground-state configuration is only slightly more favorable (1.02 meV/atom) than the lowest-energy structure, in which the Ag atom occupies a position next to the O atom. Again, this hierarchy may arise due to gold's special electronic structure. The relatively pronounced $s - d$ hybridization leads to a more strongly directional and therefore partly covalent bonding character for gold. This may result in a more favorable Au-O bond within the surface layer and stabilize Ag at a position between the Au atoms. To test this hypothesis,

a) **Surface stability diagram**



b) **Top and side views of selected ground states**

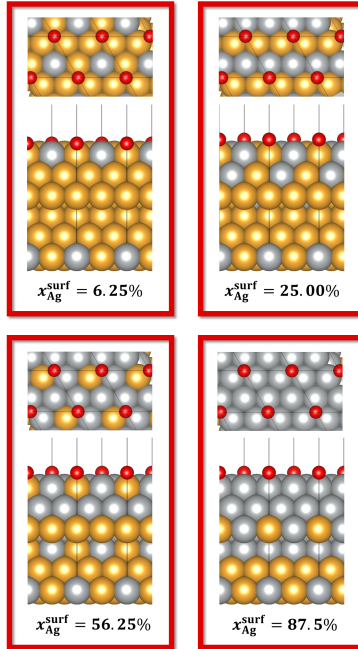


Figure 5.8.: Surface stability diagram for the Ag-Au (111) surface with $L1_2$ bulk structure and 0.25 ML adsorbed O on the fcc hollow site (a). Below, four example ground-state configurations are shown in top and side views (b). The (2×2) surface unit cell is indicated.

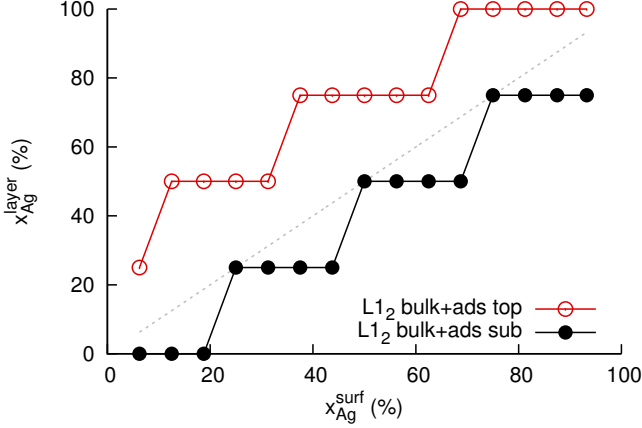


Figure 5.9.: Surface segregation profile for the Ag-Au (111) surface with adsorbed oxygen on the fcc hollow sites and $L1_2$ bulk structure. The Ag concentration in the surface and subsurface layer are shown in red and black, respectively. A gray line with a slope equal to one – corresponding to the absence of segregation – is included to guide the eye. Reproduced from Ref. [232] with the permission of AIP Publishing.

the partial density of states (DOS) for two ground states at the silver surface concentrations $x_{\text{Ag}}^{\text{surf}} = 0\%$ and $x_{\text{Ag}}^{\text{surf}} = 6.25\%$ was calculated (see Figure 5.10). The two structures differ only by one Ag atom located in-between the O atoms. The black and gray dashed curves show the $5d$ DOS of the Au atoms (atoms 1 and 2 in Figure 5.10) and the red solid curve represents the $2p$ DOS of the O atom (atom 3 in Figure 5.10). A more pronounced peak overlap of the Au-O bonding and antibonding states generally indicates a stronger hybridization and a more covalent bonding character. Looking at this overlap in Figure 5.10, it is slightly more pronounced for the structure containing a Ag atom surrounded by Au atoms. Although being a minor effect, this may contribute to small energetic preference of the obtained ground state.

5.4.3. Influence of configurational entropy on the surface segregation at Ag-Au (111) surfaces

In view of the relatively small surface formation enthalpies for both the adsorbate-free and the O-covered Ag-Au (111) surfaces with $L1_2$ bulk struc-

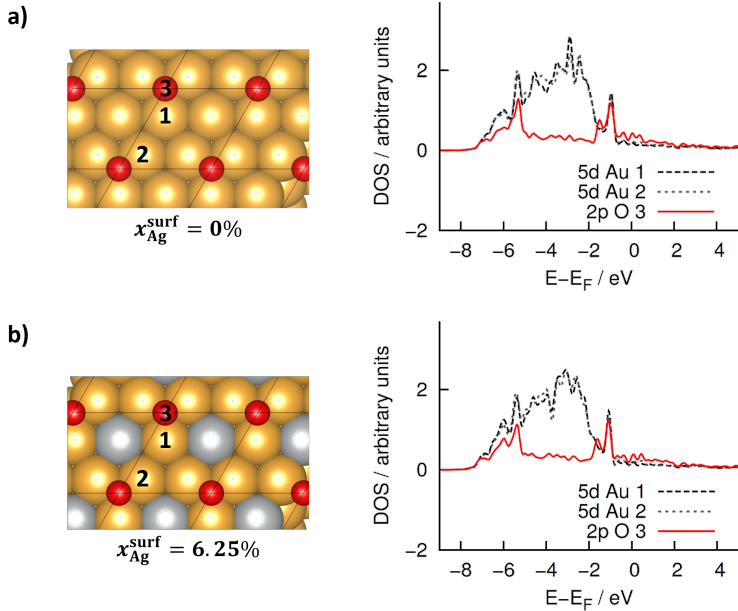


Figure 5.10.: Partial density of states (DOS) of two selected ground states at the silver surface concentrations $x_{\text{Ag}}^{\text{surf}} = 0\%$ (a) and $x_{\text{Ag}}^{\text{surf}} = 6.25\%$ (b). The black and gray dashed lines in the diagrams represent the 5d DOS of the Au atoms (atoms 1 and 2), and the red line depicts the 2p DOS of the adsorbed oxygen (atom 3). Reproduced from Ref. [232] with the permission of AIP Publishing.

ture, the influence of configurational entropy on their segregation profile was investigated. For this purpose, a simulated annealing process was modeled by means of canonical Monte Carlo simulations as implemented in UNCLE. In the past, this approach has reportedly led to excellent agreement with experimental low-energy electron diffraction (LEED) structure determination, for example for the Pt-Rh surface [247]. For both the adsorbate-free and the oxygen-covered surfaces, the simulation cells contained 40×40 atoms in the lateral directions, while the dimension along the surface normal was equal to that of the surface unit cells demonstrated in Figures 5.3 and 5.7.

The annealing process was started at $T = 100\,000$ K, which is clearly an unphysical temperature, but guarantees a random distribution of the two constituents Ag and Au within the surface layers at the beginning of the

simulation. According to the chosen temperature schedule, the MC cells were cooled down rapidly from $T = 100\,000$ K to $T = 10\,000$ K in decrements of $\delta T = 10\,000$ K. Consequently, the temperature was cooled to $T = 2000$ K in steps of $\delta T = 1000$ K, and then to $T = 1000$ K in steps of $\delta T = 200$ K. Finally, the temperature was reduced in decrements of $\delta T = 10$ K until the final temperature of $T = 10$ K was reached. Classic Metropolis iterations (see Section 4.2) were carried out after each temperature step, until the convergence criterion for the free energy of $\delta E = 10^{-6}$ eV was achieved.

Snapshots of the atomic configuration within the four surface layers at room temperature ($T = 300$ K) are shown in Figure 5.11. The respective Ag layer concentrations $x_{\text{Ag}}^{\text{layer}}$ are given at the bottom of the pictures. Gold atoms are depicted in brown, Ag atoms in gray. Clearly, no long-range order is present at this temperature. Even though it contains some silver atoms, the topmost surface layer is enriched in Au ($x_{\text{Ag}}^{\text{layer}} = 11.9\%$), while the subsurface layer is depleted of Au ($x_{\text{Ag}}^{\text{layer}} = 35.8\%$). The third and fourth layer have a practically bulk-like Ag layer concentration around 25%.

Figure 5.12 presents the silver concentration within the four surface layers for both the clean (a) and the oxygen-covered (b) surfaces at different temperatures from 0 K to 1000 K. The Ag bulk concentration of 25% is indicated with a gray line. For the adsorbate-free surface, the Au enrichment in the surface layer and Ag enrichment in the subsurface layer become less pronounced with increasing temperature, but the trend is still obtained at $T = 1000$ K.

Whereas thin surface-oxide like structures are reported to be energetically most favorable, Shi et al. [240] predicted on-surface oxygen with a low coverage of 0.06 ML to be thermodynamically stable above 450 K. The influence of configurational entropy is very similar for the oxygen-covered surface in comparison to the clean surface, meaning the segregation profile becomes less pronounced with increasing temperature. While the Ag enrichment in the surface layer decreases, the remaining three layers become more bulk-like.

Consequently, the energetically favorable surface configurations obtained in the present work for the adsorbate-free and the oxygen-covered surfaces should also be obtained in experiment, without considering phonon contributions. However, a very thorough surface preparation is crucial to ensure that no contaminants are left on the surface, which may change the segregation behavior and even reverse it, as shown here for oxygen. In addition, the

$T = 300 \text{ K}$

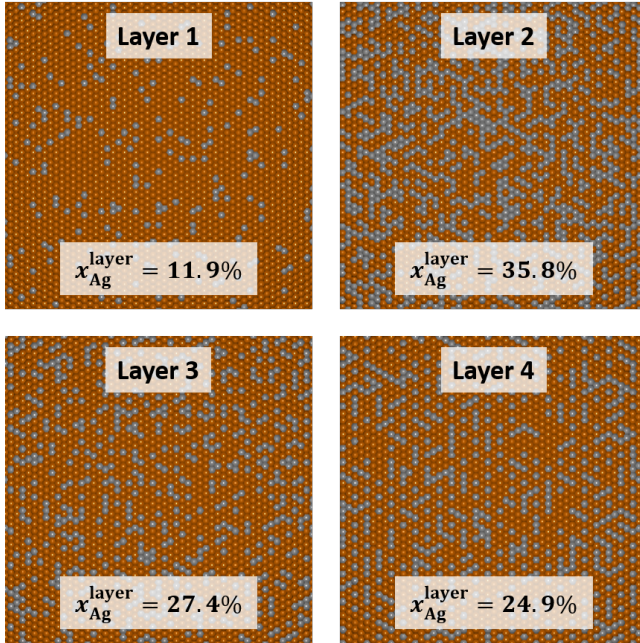


Figure 5.11.: Atomic configuration within the four surface layers as obtained from the MC simulation at $T = 300 \text{ K}$. Gold atoms are depicted in brown, silver atoms in gray. The silver surface concentration $x_{\text{Ag}}^{\text{surf}}$ is given in the pictures.

atomic ordering of the experimentally studied samples has to correspond to thermodynamic equilibrium, and must not be kinetically controlled.

5.4.4. Clean Ag-Au (321) surface

Computational details

The Au (321) surface represents a highly interesting surface from a catalytic point of view, as it contains a rather large number of different adsorption sites, for example atomic positions in the middle of the (111) terraces or highly under-coordinated Au atoms at the edges of the terraces. This work analyzes how the presence of steps and terraces at the surface influences the segregation behavior of Ag impurities. For this purpose, the adsorbate-free

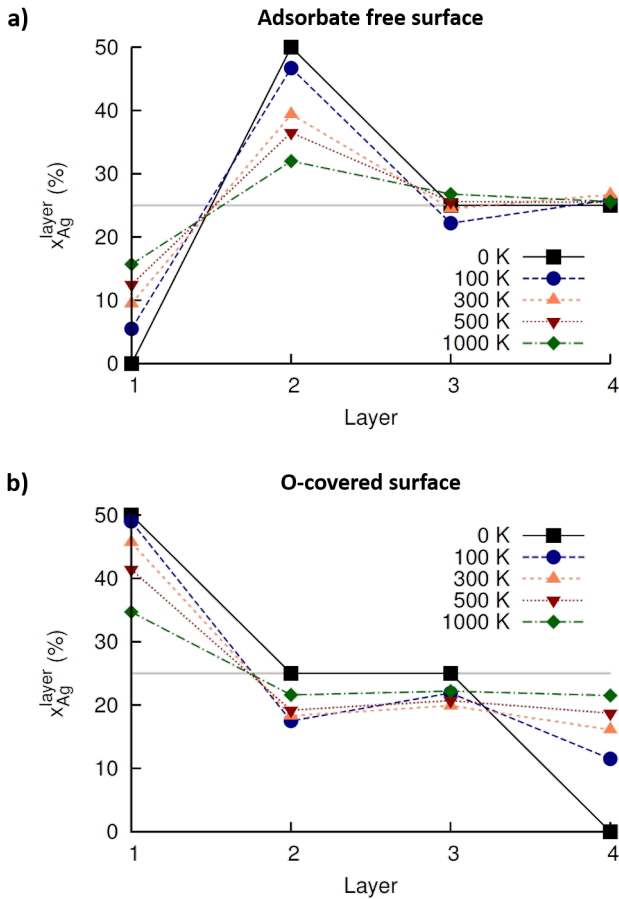


Figure 5.12.: Silver concentration $x_{\text{Ag}}^{\text{layer}}$ within the four surface layers for the adsorbate-free (a) and the oxygen-covered (b) Ag-Au (111) surface with L1₂ bulk. Layer 1 corresponds to the topmost layer, layer 2 to the subsurface layer, and so on. The Ag bulk concentration of 25% is indicated by a gray horizontal line to guide the eye. Reproduced from Ref. [232] with the permission of AIP Publishing.

Au (321) surface was modeled in an asymmetric (2×1) surface slab containing 28 Au atoms and a vacuum region of $\approx 7.7 \text{ \AA}$ (see Figure 5.13). Analogous to the (111) surfaces, dipole corrections were used to ensure a faster convergence of the total energy with increasing thickness of the vacuum. A k-point set of 15×11 k-points within the surface plane and 1 k-point along the surface normal was employed for all calculations. The uppermost 14 atoms of the slab were allowed to relax in two iterative steps until the forces acting on the ions reached a value smaller than 7 meV \AA^{-1} . To create CE input structures with various Ag surface concentrations and configurations, those same 14 atoms were partially replaced by Ag atoms. The chosen slab geometry thereby confined the silver surface concentration step size to 7.124%.

Section 5.4.1 revealed that the Ag bulk concentration does not have a large influence on the surface segregation behavior. For this reason and because the $L1_2$ ordered structure may only be realized in a larger surface unit cell than employed here, a pure Ag bulk was chosen for the clean Au (321) surface.

The formation enthalpies of the $2^{14} = 16384$ possible atomic configurations were obtained via a cluster expansion. The CE fit included up to 6-body interactions and 163 input structures. The low cross-validation score of $S_{CV} = 0.4 \text{ meV}$ indicates a highly predictive fit and a reliable determination of the ground-state structures.

Segregation results

Analogous to the Ag-Au (111) surface, the formation enthalpies for the clean Au (321) surface with Ag impurities within the uppermost 14 atoms were calculated applying Equation (5.4). The resulting surface stability diagram and four selected example ground states are presented in Figure 5.14a and b, respectively. Similar to the (111) surface, the surface formation enthalpies are also relatively small, so that entropic contributions may prevent the obtained structures from forming already at room temperature. The calculated ground-state lines from DFT and the CE coincide and contain numerous ground states.

Up to silver surface concentration of $x_{\text{Ag}}^{\text{surf}} = 28.6\%$, the lowest four of the 14 uppermost atoms are subsequently occupied by silver. As $x_{\text{Ag}}^{\text{surf}}$ is increased further, the most favorable atomic positions for further Ag atoms are located at the edge of the (111) terraces. For higher silver surface concentrations, the remaining subsurface Au atoms are first replaced by Ag, followed by the

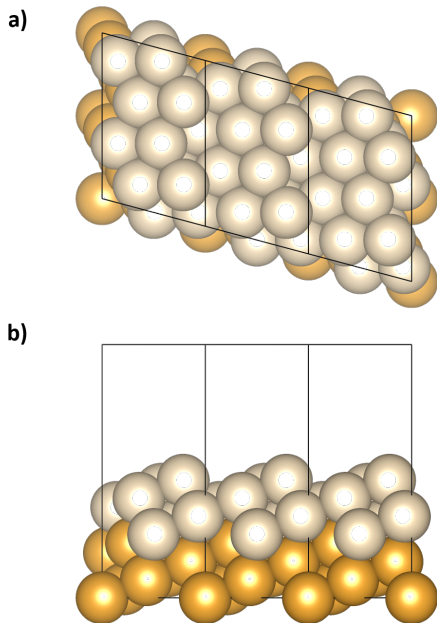


Figure 5.13.: Top view (a) and side view (b) of the adsorbate-free Au (321) surface. The uppermost 14 atoms were substituted by Ag for the CE input structures and are depicted in beige. The (2×1) unit cell is indicated.

atoms within the (111) terraces.

Considering the previous results for the adsorbate-free Ag-Au (111) surface (see Section 5.4.1), one may expect a charge transfer from subsurface silver atoms to stabilize gold atoms at the surface. This seems to be the case for the atoms within the (111) terraces, which are replaced by Ag last. The positions at the edges of the terraces, however, appear to be less influenced by this effect and possibly the lower surface energy of silver causes them to be occupied by Ag atoms after all subsurface atoms are already replaced.

A Bader charge analysis of the pure Au (321) surface reveals an average excess charge of $0.02 e/\text{atom}$ within the uppermost 8 atoms of the slab, which are located at the surface. Regarding the charge associated with the single atoms, it is highest for the position at the edges of the terraces. For the ground state at a silver surface concentration of $x_{\text{Ag}}^{\text{surf}} = 28.6\%$ (see Figure 5.14b), this excess charge is $0.06 e/\text{atom}$, while the subsurface Ag atoms

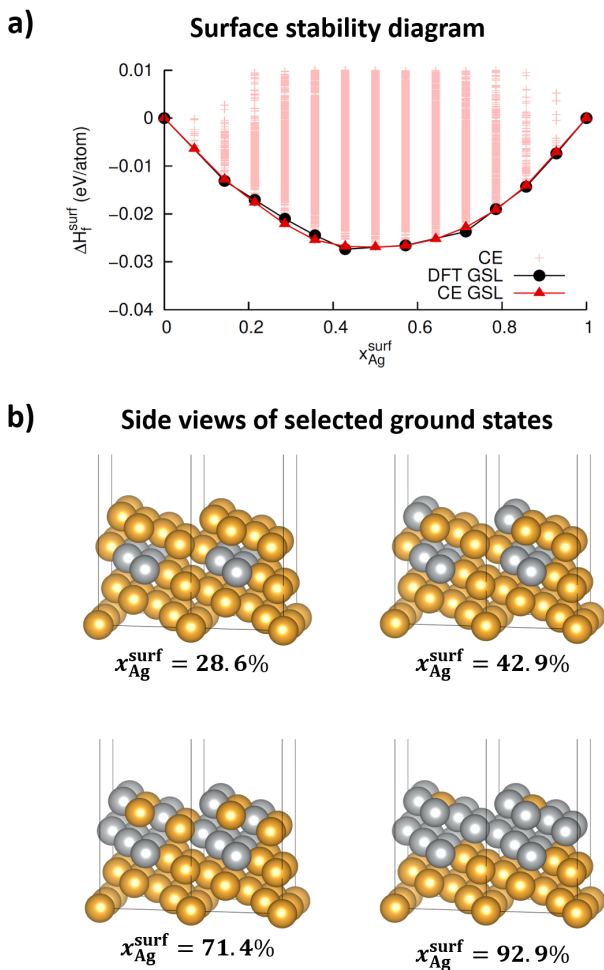


Figure 5.14.: Surface stability diagram for the clean Au (321) surface with Ag impurities within the uppermost 14 atoms of the surface slab (a). Four selected ground states are depicted in side views below the diagram with the respective Ag surface concentrations $x_{\text{Ag}}^{\text{surf}}$ given beneath the pictures (b). Au atoms are depicted in gold and Ag atoms in gray.

are depleted of charge. The atoms at the edge of the terraces, however, experience the smallest charge transfer. When those two atoms are also replaced by silver ($x_{\text{Ag}}^{\text{surf}} = 42.9\%$), more charge is transferred to the remaining Au atoms within the (111) terraces and the average excess charge on them is 0.12 e/atom, possibly stabilizing them at the surface. This configuration has the lowest surface formation enthalpy in the surface stability diagram, meaning that, compared to all 14 atoms occupied by Au or Ag, respectively, it is the most stable structure.

Figure 5.15 shows the difference between the charge density obtained from the fully converged DFT calculation of the relaxed surface and that of the superposition of atomic charges for the same atomic positions for the ground state at a silver surface concentration of $x_{\text{Ag}}^{\text{surf}} = 28.6\%$ and of $x_{\text{Ag}}^{\text{surf}} = 42.9\%$, respectively. The blue surface represents an isosurface at $0.005 \text{ e}/\text{\AA}^3$. When the surface atoms are all occupied by gold, there is a large charge accumulation in the region across the steps between the (111) terraces and the Au atom at the edge relaxes slightly inward. However, if the atoms at the edge are replaced by silver, they relax slightly outward the surface and the electron accumulation in the bonding region across the step is much smaller than for Au atoms. Instead, an increased electron accumulation is observed in the region within the terraces.

In summary, the segregation behavior of the clean stepped Au (321) surface with Ag impurities seems to be similar to that of the adsorbate-free Ag-Au (111) surface. Gold prevails at the surface for smaller silver surface concentrations, possibly due to a charge transfer from silver to the more electronegative gold. This effect may be less pronounced for the Au atoms at the edge of the terraces, which are replaced by silver first. However, due to the chosen slab geometry, only six of the 14 uppermost atoms are subsurface, while 8 atoms are within the surface layer. Since the lowest Au atoms are the first ones to be occupied by Ag at low silver surface concentrations, it would be interesting to analyze the influence of allowing more than those 14 atoms to be replaced by Ag on the segregation behavior.

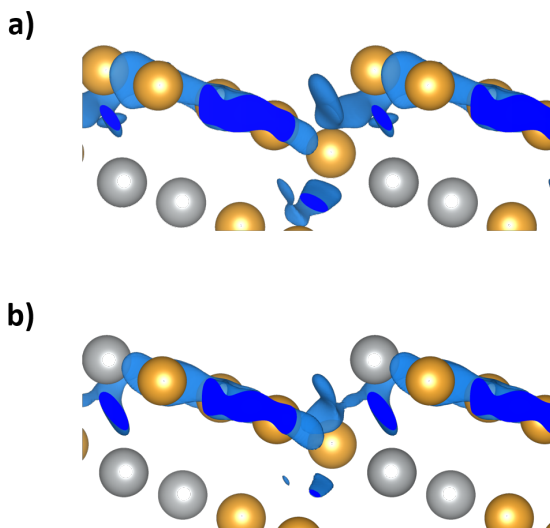


Figure 5.15.: Charge density difference between the charge density obtained from the fully converged DFT calculation and the superposition of atomic charges for the ground state at $x_{\text{Ag}}^{\text{surf}} = 28.6\%$ (a) and that at $x_{\text{Ag}}^{\text{surf}} = 42.9\%$ (b). The blue surface represents an isosurface at $0.005 e/\text{\AA}^3$. Au atoms are depicted in gold and Ag atoms in gray.

5.4.5. O-covered Ag-Au (321) surface

Computational details

For pure Au surfaces, oxygen adsorption energetics and geometries have been studied via UHV experiments [248–253] and theoretically by means of first-principles calculations [63, 240, 241, 251, 254]. Employing DFT calculations, Fajin et al. [255] analyzed preferred adsorption geometries of atomic and molecular oxygen on the Au (321) surface. Their results indicate that single oxygen atoms favor adsorption on the fcc hollow sites near the edges of the steps that connect the (111) terraces, while molecules prefer to be located in a way that their O–O axis is planar to the (111) terraces on bridge or nearby bridge sites. In a consecutive DFT study, Fajin et al. [256] found that upon higher oxygen coverages, a reconstructed Au (321) surface with highly oxidized structures was energetically most favorable. Very recently, Moskaleva et al. reported that for coverages of 0.2 ML or higher, the most stable surface configurations for adsorbed oxygen on the Au (321) surface are characterized by linear –O–Au–O– fragments. In addition, they showed that the presence of silver impurities even stabilizes this oxygen-covered Au (321) surface structure with respect to the clean surface. Apart from the Au (321) surface, these chains of alternating Au and O atoms also represent a common feature of thermodynamically stable surface configurations of the Au (111) [240, 241] and the Au (110) [253, 257] surfaces.

In the present work, the oxygen-covered Au (321) surface was modeled in an asymmetric (2×1) surface slab containing 28 Au atoms and two oxygen atoms building an infinite –(O–Au)– chain (see Figure 5.16). This chosen size of the unit cell offered the advantage of maintaining both low computational cost and a separation between the oxide chains that is large enough to avoid direct interactions between them. Furthermore, the modeled O coverage of 0.2 ML represents the minimum possible coverage allowing for chain formation for the present unit cell size.

The upper and lower surface of two periodically repeated slabs were separated by a vacuum region of $\sim 7.7 \text{ \AA}$ and like for the previous calculations, dipole corrections were employed. Analogous to the clean Au (321) surface, a set of $15 \times 11 \times 1$ k-points was employed for all calculations. The upper 14 atoms (beige in Figure 5.16) and the two oxygen atoms were allowed to relax in two iterative relaxation steps until the forces acting on the ions

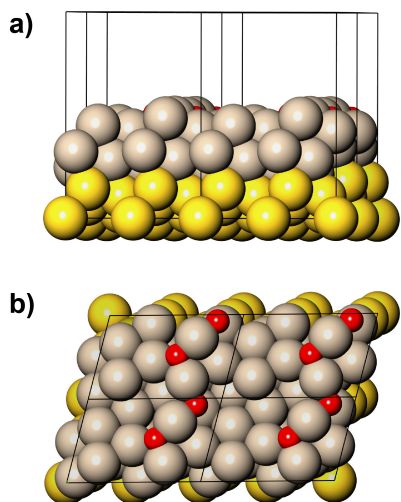


Figure 5.16.: Side view (a) and top view (b) of the Au (321) surface slab with infinite oxide chain. Atoms that were substituted by Ag for the CE input structures are depicted in beige, while the O atoms building the $-(\text{O}-\text{Au})-$ chain are shown in red. The (2×1) unit cell is indicated. Reproduced from Ref. [258] with permission from the PCCP owner societies.

reached a value smaller than 7 meV \AA^{-1} and the lower 14 gold atoms (gold in Figure 5.16) were kept fixed during all calculations. Analogous to the adsorbate-free Au (321) surface, the uppermost 14 atoms could be occupied by either Ag or Au to generate CE input structures with different Ag surface concentrations. In theory, this kind of surface alloying might result in local strain due to a mismatch in lattice constants of the two elements. This mismatch, however, is negligible for silver and gold (the values of a_0 optimized with the PBE-D3 functional are 4.099 \AA and 4.073 \AA , respectively). Using the two values of lattice constants to calculate the adsorption energy of O consequently resulted in a difference of less than 25 meV .

Figure 5.17 illustrates the displacements that the atoms close to the surface undergo upon formation of the infinite oxide chain. The adsorbate-free reference surface is depicted with gray atoms, while the final surface structure is shown in gold Au and red O atoms. Two atoms undergo significant vertical displacements out of the surface to bond with the two oxygen atoms and build the chain going across the steps. In the process, surrounding Au atoms are also slightly displaced vertically and horizontally.

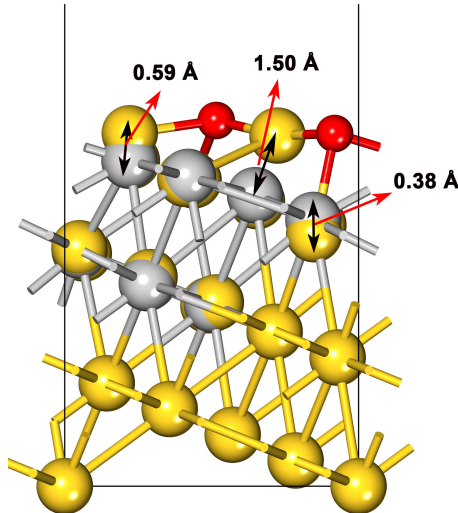


Figure 5.17.: Reconstruction of the adsorbate-free Au (321) surface upon formation of the infinite $-(\text{O}-\text{Au})-$ chain going across the steps. Initial Au positions are shown in gray, final Au positions in gold and O atoms in red. Reproduced from Ref. [258] with permission from the PCCP owner societies.

A cluster expansion was performed to identify the energetically most favorable structures from 16 384 possible surface configurations. For 116 DFT input structures and including up to 6-body interactions, a stable CE with a cross-validation score of $S_{CV} = 0.8$ meV was achieved.

A similar approach to determine the lowest-energy chemical ordering based on the topological degrees of freedom was realized by Kozlov et al. [259] for bimetallic nanoparticles at DFT level of accuracy. As compared to their method, the CE fit employed in the present work offers the advantage of selectively choosing the most important effective interactions out of two-body as well as many-body interactions up to a controllable size. Hence, a highly representative Hamiltonian for the system at hand is obtained.

Segregation results

For the bimetallic surface with an infinite oxide chains, the surface formation enthalpies of all possible configurations were calculated according to Equation (5.4). The two oxygen atoms in the slab were included in the total number of atoms used to calculate ΔH_{surf} . Figure 5.18a shows the ground-state diagram obtained from the CE fit, where each brown cross corresponds to a fully relaxed surface configuration predicted by the CE. The fact that the two ground-state lines – the convex hull marking the energetically most favorable structures – from DFT input structures and CE predictions coincide demonstrates the good convergence of the CE fit. Numerous ground states within the whole Ag surface concentration range were found along the ground-state line. Below the surface stability diagram, six example ground-state configurations are illustrated in top views (Figure 5.18b). Au atoms are depicted in gold, Ag atoms in blue and O atoms in red. The respective Ag surface concentrations $x_{\text{Ag}}^{\text{surf}}$ are given below the pictures.

Considering the magnitude of the calculated formation surface formation enthalpies, however, the obtained values of up to $\Delta H_{\text{surf}} = 26$ meV are very small and suggest that the predicted surface configurations might not even be thermodynamically stable already at room temperature.

As explained at the beginning of this chapter in Section 5.3, the employed PBE exchange-correlation functional with D3 corrections was chosen carefully and based on tests for the equilibrium lattice constant, surface energy and surface relaxations. While the choice of a functional may always change the absolute values of calculated surface formation enthalpies, the qualita-

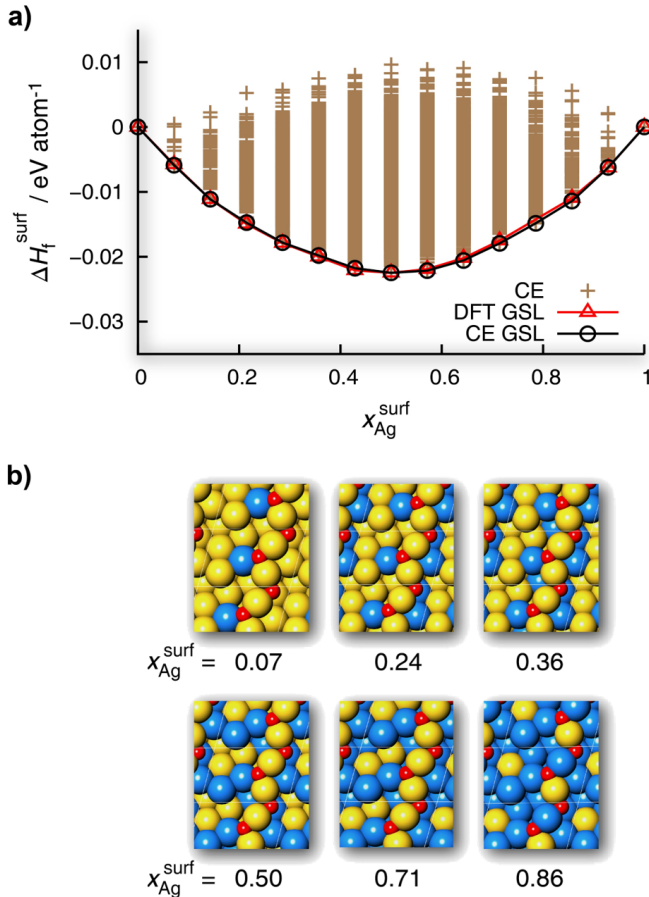


Figure 5.18.: Surface stability diagram for the Au (321) surface with Ag impurities within the uppermost 14 atoms of the unit cell and an infinite oxide chain (a). The configuration of six selected ground-state structures is shown in top views with the respective Ag surface concentration $x_{\text{Ag}}^{\text{surf}}$ given below the pictures (b). Au atoms are depicted in gold, Ag atoms in blue and O atoms in red. Reproduced from Ref. [258] with permission from the PCCP owner societies.

tive result remains valid as long as the obtained hierarchy and therefore the energetic preference of one structure over the other is preserved. To ensure that this was the case for the present results, formation enthalpies ΔH_{surf} were calculated for different structures at the same Ag surface concentration $x_{\text{Ag}}^{\text{surf}} = 35.7\%$ (which was chosen arbitrarily) employing the pure PBE functional in comparison to the values for PBE with dispersion corrections (D3) (see Table 5.7). For both functionals, the energetically most favorable structure is the same, and also the overall hierarchy is preserved with some slight deviations. Thus, adding the D3 dispersion correction to the PBE results should not have any impact on the qualitative outcome of the present study.

Table 5.7.: Surface formation enthalpies ΔH_{surf} of selected structures at constant Ag surface concentration $x_{\text{Ag}}^{\text{surf}} = 35.7\%$ for PBE and PBE+D3. The structure numbers emerge from the enumeration algorithm implemented in UNCLE and do not have any specific meaning.

Structure no.	ΔH_{surf} [meV]	
	PBE	PBE+D3
7848	-27.5	-20.0
16036	-25.9	-19.8
7908	-25.0	-19.7
8100	-21.8	-19.1
15528	-22.4	-18.6
7080	-21.8	-17.0
16260	-17.6	-16.2
11056	-16.7	-13.2
16	-6.1	-6.9

The present results for the energetically most favorable configurations are somewhat in contrast to what one would expect from intuition. In theory, it seems plausible that the silver atoms should preferably occupy all positions close to the oxygen atoms first, because, due to its less noble nature, silver ought to bind to oxygen more strongly. This hypothesis is supported by estimates from the O adsorption energies from a previous theoretical study [260], suggesting that an ordinary Ag–O bond is 90 – 130 meV stronger than a Au–O bond. Looking at the top views of the ground states presented in Figure 5.18, one phenomenon is striking: Below Ag surface concentrations of $x_{\text{Ag}}^{\text{surf}} = 85.7\%$, the Ag atoms are preferably located around the $-(\text{O}-\text{Au})$ -chain, but never within the chain substituting the Au atoms. First, Au atoms

at the surface adjacent to the oxide chain are replaced by Ag, followed by Au atoms beneath the chain. With increasing Ag surface concentration, Au atoms at and beneath the characteristic (111) terraces of the (321) surface are replaced by Ag, whereas the atomic site in the middle of the terraces is occupied by Au up to high values of $x_{\text{Ag}}^{\text{surf}}$.

Figure 5.19 illustrates the silver concentration $x_{\text{Ag}}^{\text{layer}}$ within the surface and subsurface layer for varying silver surface concentrations $x_{\text{Ag}}^{\text{surf}}$. Here, the surface layer was defined as those metal atoms of the surface slab that do not have another atom on top of them. Consequently, each layer consists of six atoms. Generally, $x_{\text{Ag}}^{\text{layer}}$ increases approximately linearly with increasing silver surface concentration. Up to $x_{\text{Ag}}^{\text{surf}} = 0.5$, the surface layer has a larger Ag concentration than the subsurface layer, while for $x_{\text{Ag}}^{\text{surf}} > 0.5$, the two lines cross and the Ag concentration is larger in the subsurface layer. This crossing corresponds to the point where no further direct Ag–O bonds can be formed within the surface layer and all low-coordinated surface atoms are already occupied by Ag. At the same time, substitution of Au by Ag within the $-(\text{O}-\text{Au})-$ chain is energetically unfavorable and occurs only at very high Ag surface concentrations.

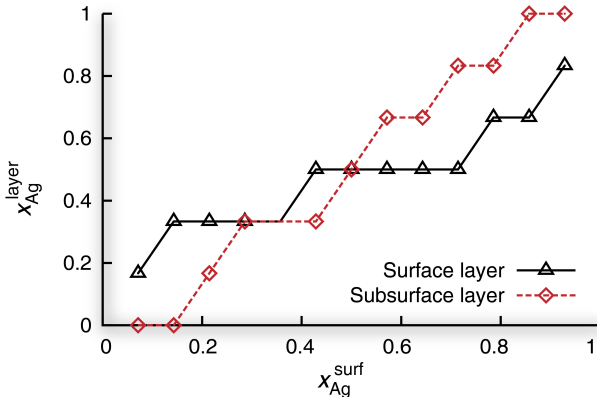


Figure 5.19.: Ag layer concentration $x_{\text{Ag}}^{\text{layer}}$ in the surface (black, solid) and subsurface (red, dashed) layer for the ground states at all Ag surface concentrations. Reproduced from Ref. [258] with permission from the PCCP owner societies.

The special electronic structure of gold, which was already mentioned in connection with the unexpected Au segregation to the Ag-Au (111) surface

layer (see Section 5.4.1), also explains the present results for the (321) surface with an infinite oxide chain. The relatively strong *s-d* hybridization causes a more covalent bonding character for gold, which may result in a stronger bonding between the Au and O atoms within the infinite oxide chain, consequently stabilizing Au in these positions.

Fortunately, DFT calculations provide insight into the electronic structure and allow a detailed investigation employing certain techniques, which will be explained in the course of this analysis. This way, the different nature of the bonding characteristics of Ag and Au located within and around the infinite oxide chain was studied for selected surface configurations.

In a first step, the partial density of states (DOS) was calculated for four different structures with two Ag atoms within the oxide chain, one Ag and Au atom in the chain, two Au atoms in the chain and two Au atoms in the chain with an additional Ag atom adjacent to it, respectively. Figure 5.20 illustrates top views of the configurations under consideration. Next to them, diagrams show the *4d* and the *5d* DOS plots for the two metal atoms (1 and 2) within the oxide chain (dashed/dotted curves) and the *2p* DOS plots for the two oxygen atoms (3 and 4, red curve). In the present DOS curves, a covalent bonding character is indicated by an overlap between peaks close to the Ag–O or Au–O bonding and antibonding states, respectively. In the diagrams, these are located around -6 eV and -1 eV relative to the Fermi energy. The mentioned overlap between peaks is relatively weak for the case of a pure $-(\text{O-Ag})-$ chain (Figure 5.20a). However, it increases as a Au atom replaces one Ag atom (Figure 5.20b) and becomes even stronger for the pure Au (321) surface with an $-(\text{O-Au})-$ chain (Figure 5.20c). The strongest peak overlap and therefore the most pronounced covalent bonding character seems to occur for a Ag atom next to the pure $-(\text{O-Au})-$ chain (Figure 5.20d). This surface configuration is also the energetically most favorable structure at that respective Ag surface configuration (see Figure 5.18b). Both the stronger covalent bonding and the energetic preference of this structure may arise from a charge transfer from the adjacent Ag atom into the oxide chain. This hypothesis was tested via a Bader charge analysis, revealing that the excess negative charge within the oxide chain (including the positive charge on Au and the negative charge on the O atoms) is 0.62 e in the presence of Ag next to the chain, compared to 0.57 e for the pure Au surface. In turn, the Ag atom adjacent to the chain bears a significantly larger positive charge

of $+0.40 e$ than the Au atom would have at the same position ($+0.18 e$).

The Bader charges within the oxide chain may also provide information on the bonding character between metal and oxygen atoms. For the pure $-(\text{O}-\text{Ag})-$ chain, calculations revealed an average negative charge of $-0.80 e$ on the O atoms, while the Ag atoms bear an average positive charge of $+0.58 e$. For the pure $-(\text{O}-\text{Au})-$ chain, both these values are smaller in magnitude ($-0.76 e$ and $+0.48 e$, respectively), indicating a less ionic and more covalent bonding between gold and oxygen within the infinite oxide chain.

In a second step, the electron localization function (ELF) was calculated for the structures in Figure 5.20a and c with only Ag atoms and only Au atoms within the oxide chain, respectively. The ELF was first defined by Becke and Edgecombe in 1990 [261] and provides a measurement of electron localization by considering the probability for an electron to be located in the neighborhood space of a reference electron with the same spin. For numerical convenience, the ELF is mapped to a function which is defined between zero and one, where the uniform electron gas serves as a reference point and corresponds to a value of 0.5. Hence, a value of the ELF close to one indicates a region where there is a high probability of finding electron localization. The results of the analysis are presented in Figure 5.21, where the $-(\text{O}-\text{Ag})-$ and the $-(\text{O}-\text{Au})-$ chains are vertically oriented and the ELF is plotted in the plain containing metal atoms 1 and 2 and oxygen atom 3 in Figure 5.20. The regions of low ELF values in the center of the atoms arise because the DFT calculations consider only the valence electrons. In Figure 5.21a, the ELF around the O atoms exhibits relatively sharp boundaries and there is a very small probability for electrons to be located around the Ag atoms. These features indicate a predominantly ionic bond within the oxide chain. Yet, deviations from a perfectly spherical shape of the ELF around the O atoms suggest a small covalent contribution for both the Ag-O and Au-O bonds within the chain. In Figure 5.21b, the boundaries of the ELF in the bonding region between Au and O become more blurry as compared to the Ag-O bond. In addition, the striking difference to the ELF results for the $-(\text{O}-\text{Ag})-$ chain are regions of increased ELF around the Au atoms. The shape of these regions clearly deviates from spherical, indicating directional bonding.

In a third step, a crystal orbital Hamilton population (COHP) analysis [262, 263] was employed for the pure $-(\text{O}-\text{Ag})-$ and the pure $-(\text{O}-\text{Au})-$

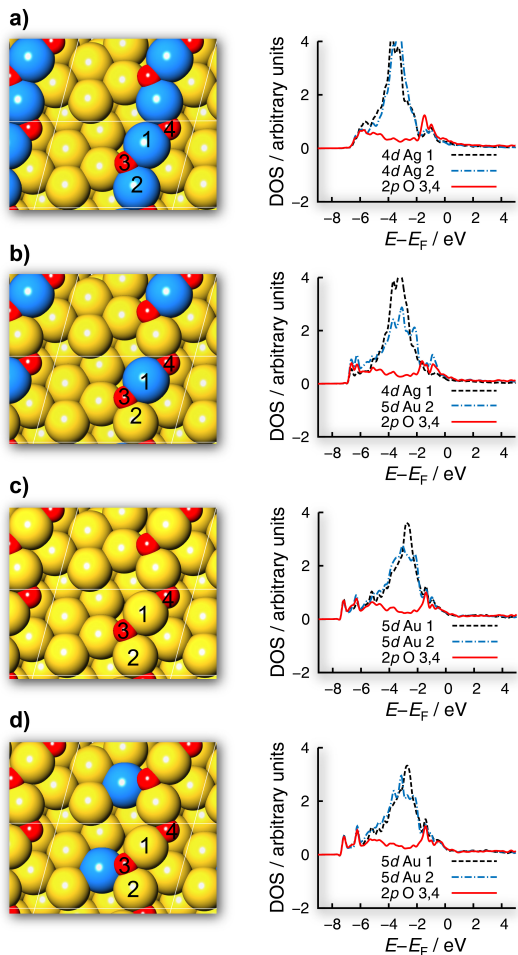


Figure 5.20.: Partial density of states (DOS) of four selected configurations: two Ag atoms in the infinite oxide chain (a), one Ag and one Au atom in the chain (b), two Au atoms in the chain (c) and two Au atoms in the chain and one Ag atom adjacent to it (d). The black dashed and the blue dashed/dotted lines show the 4*d* or 5*d* DOS of the Ag or Au atoms, respectively, in the oxide chain (atoms 1 and 2), and the red solid line represents the 2*p* DOS of the oxygen atoms in the chain (atoms 3 and 4). In the top views next to the diagrams, Au atoms are shown in gold, Ag atoms in blue and O atoms in red. Reproduced from Ref. [258] with permission from the PCCP owner societies.

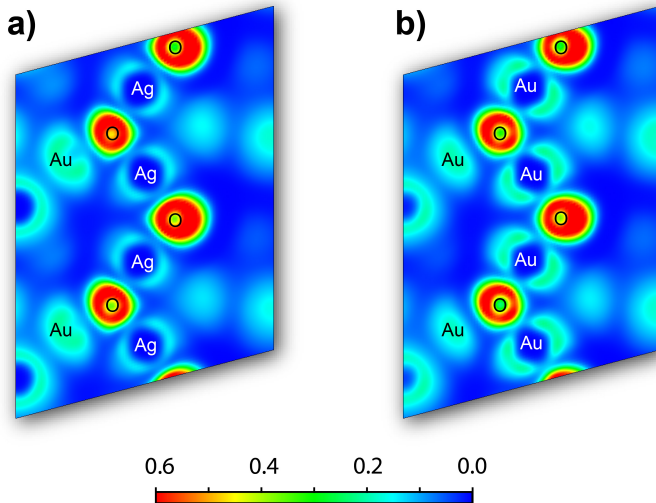


Figure 5.21.: Electronic localization function (ELF) for two surface configurations with an $-(\text{O-Ag})-$ chain (a) and an $-(\text{O-Au})-$ chain (b), respectively. Blue regions indicate low ELF values, while high ELF values are depicted in red. Reproduced from Ref. [258] with permission from the PCCP owner societies.

chains, respectively. This analysis partitions the band structure energy into bonding, nonbonding and antibonding contributions, where a positive value of the COHP corresponds to bonding energy regions (positive overlap population) and a negative value indicates antibonding interactions. In the present work, the COHP analysis was carried out with the program code LOBSTER [262–266]. Figure 5.22 shows the negative average COHP between Ag and O atoms (a) and Au and O atoms (b) within the oxide chain, respectively. Alongside the COHP, the partial DOS is plotted, which indicates the energy levels of the electrons, but does not reveal anything about their bonding nature. The filled area under the COHP curve on the right-hand side corresponds to bonding contributions, while the left-hand side represents antibonding contributions. The Fermi energy is included as a horizontal line. For both Ag and Au within the oxide chain, the analysis yields two groups of filled bonding and partially filled antibonding states below the Fermi level. The present findings are consistent with low lying completely filled d -bands of Ag and Au. Comparing the COHP curve to the partial DOS, it becomes

evident that the mentioned two groups are mainly composed of the bonding and antibonding states between Ag/Au and O. The attractive interaction between O and Ag/Au originates in filling the bonding states and emptying some of the antibonding states.

Strikingly, the peak resonances for the $-(\text{O-Au})-$ chain are far more pronounced than those for the $-(\text{O-Ag})-$ chain, indicating a more covalent bonding character of the former. In addition, the bonding states for the $-(\text{O-Au})-$ chain lie at lower energy values than those of the $-(\text{O-Ag})-$ chain. This results in a larger gap between the bonding and antibonding peaks, which is indicative of a stronger orbital interaction.

Combined with results from the Bader analysis and the ELF, the different techniques to analyze the electronic structure and thus the bonding nature reveal that the Au–O bonds within the infinite oxide chain are more covalent and less ionic than the Ag–O bonds.

A partially covalent Au–O bonding within the oxide chain should also affect the bond lengths in and around the chain. Compared to Ag–O bonds in the chain and also to bonds between O and Au nearest neighbors within the surface, the Au–O bonds in the chain should have a shorter bond length. Indeed, the relaxed DFT structures reveal that the average Au–O bond length within the oxide chain in Figure 5.20c equals 2.02 Å, while the corresponding Ag–O bond length in Figure 5.20a is slightly larger with 2.06 Å. For the $-(\text{O-Au})-$ chain, the bond length between the O atoms and their nearest Au neighbors in the surface equals 2.18 Å, whereas the same distance for the $-(\text{O-Ag})-$ chain is only 2.10 Å. Hence, also the analysis of different bond lengths indicates a stronger covalent contribution to the bonding character for the $-(\text{O-Au})-$ chain than for the $-(\text{O-Ag})-$ chain.

Finally, some knowledge may be gained by looking more closely at the obtained energetics. The surface formation enthalpy ΔH_f^{surf} quantifies the stability of a certain structure containing Ag and Au atoms with respect to a phase separation into the two reference surface configurations, where the 14 uppermost atoms are occupied by either only Ag or Au, respectively. As a consequence, the pure gold surface with an infinite oxide (Figure 5.20c) chain has the surface formation enthalpy of $\Delta H_f^{\text{surf}} = 0$ meV. Replacing only one Au–O bond of this reference structure by a Ag–O bond gives a rough estimate of the difference between the two bond energies. An example for this is given by the ground state at the Ag surface concentration $x_{\text{Ag}}^{\text{surf}} = 6.25\%$

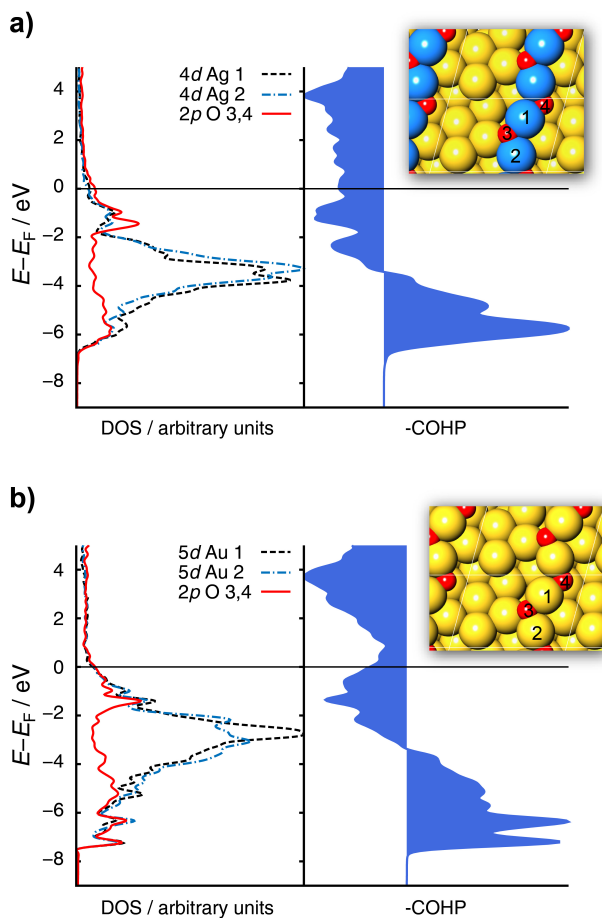


Figure 5.22.: Partial DOS and COHP analysis for the structure with an $-(\text{O-Ag})-$ chain (a) and the structure with an $-(\text{O-Au})-$ chain (b). Top views of the respective structures are shown in the top right corner of the diagrams. Reproduced from Ref. [258] with permission from the PCCP owner societies.

(Figure 5.20d), for which $\Delta H_f^{\text{surf}} = -173$ meV. This value is in good agreement with the estimates from O adsorption energies from the literature [260] (100 – 170 meV). The present value may be slightly larger in magnitude as it also includes favorable contributions from replacing homometallic Au–Au bonds with heterometallic Ag–Au bonds. However, the difference between the bond energies of Ag–O and Au–O bonds within the oxide chain is very small, as estimated from O adsorption energies [260]. Upon comparison of the surface formation enthalpies of the surface configurations with a Ag atom within the chain ($\Delta H_f^{\text{surf}} = -7$ meV, Figure 5.20b) and one next to it ($\Delta H_f^{\text{surf}} = -173$ meV, Figure 5.20d), two aspects become evident: First, the large negative value for ΔH_f^{surf} of the structure in Figure 5.20d suggests that the Ag–O bond outside the chain is stronger than the Au–O bond and therefore, Ag prefers locations close to the oxygen atoms. Second, Ag positions binding to O outside the chain are clearly preferred over positions within the oxide chain.

Ab initio molecular dynamics (AIMD) simulations [258], which were carried out in collaboration with the University of Bremen, support the results obtained from the DFT and CE calculations in this work. They revealed two interesting aspects. First, a Ag impurity located at the kink of a Au (321) surface at least 5 \AA away from a (O–Au–O) fragment diffused towards the fragment and bonds with an O atom. During this process, the (O–Au–O) fragment behaved as a single entity and only slightly moved its axis. This demonstrates that the O atoms within the chain attract silver atoms and also that silver atoms at kink sites are especially prone to diffusion. Figure 5.23 shows the distance of the Ag atom (Ag_1) and the O atom over the course of the simulation and snapshots at four different times over the diagram. After about 5 ps, a Ag–O bonding is established and kept. In a second AIMD simulation, it was shown that not only Ag migrates towards the oxide chain, but also the chain itself adjusts its position to maximize the number of Ag–O contacts without destroying the chain structure.

Summarizing the findings of this subsection, the obtained ground-state configurations in the surface stability diagram of Figure 5.18 arise due to two effects. On the one hand, silver is most stable at locations adjacent to the O atoms, because it binds to oxygen more strongly than gold. On the other hand, strong-partially covalent bonds between gold and oxygen stabilize gold within the infinite oxide chain.

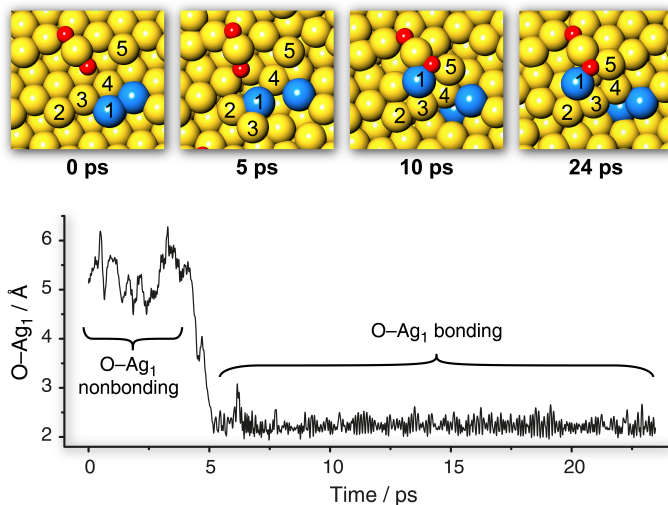


Figure 5.23.: An AIMD simulation of Ag diffusion from a kink site in the Au (321) surface to an (O–Au–O) fragment. The Ag₁–O distance between the migrating Ag atom Ag₁ and the nearest O atom of the fragment is plotted as a function of time. Au is depicted in gold, Ag in blue and O in red. Reproduced from Ref. [258] with permission from the PCCP owner societies.

Electromechanical coupling at the Ag-Au (111) surface

"The role of the infinitely small in nature is infinitely great."

- *Louis Pasteur*

This chapter deals with an interesting phenomenon that connects lattice deformation with catalytic performance. Nanoporous gold (npAu) features a fairly complex structure, where the consequences of an applied macroscopic strain are non-trivial. Due to this structure, however, it offers outstanding catalytic properties. The coupling between those two parameters, referred to as electromechanical coupling, will be analyzed for the model Ag-Au (111) surface in the present work.

6.1. Theoretical background

Nanoporous metals represent an attractive material for actuators, since they have been reported to respond to potential variation by macroscopic contraction or expansion [267–271]. When their sponge-like structure is filled with an electrolyte, extremely large internal electrode surfaces are created. Applying an electric potential locally changes the surface stress of the ligaments, resulting in large volume changes and a considerable mechanical work density. In an experimental study, Biener et al. [62] obtained reversible strain

amplitudes of the order of a few tenths of a percent by alternating exposure of nanoporous gold samples to ozone and carbon monoxide. They explained their findings by an adsorbate-induced change of the surface stress, thereby exploiting the potential of chemistry-driven actuators and sensors.

For bulk metal electrodes, the change in surface stress f due to charging is characterized by the coupling coefficient ς :

$$\varsigma = \left. \frac{\partial f}{\partial q} \right|_e, \quad (6.1)$$

where q is the superficial charge density and e is the tangential elastic area strain (relative change in area). This relation has been explored both theoretically and experimentally [220, 272–274] for various metals. Regarding gold, Haiss et al. [272] found an influence of the electrolyte on the response parameter ς for the Au (111) surface and therefore could not give a numerical result. By cantilever bending through electrochemical charging, Smetanin et al. [220] obtained a value for ς of -2 V, which is close to the theoretical one of -1.86 V determined by ab-initio calculations [275]. They attributed the slight divergence in literature to a charge transfer between the electrode metal and adsorbed anions of the electrolyte solution influencing the coefficient. By choosing weakly adsorbing anions as adsorbates, they avoided this problem.

The response of the charge density q to a change in surface stress f is connected to the response of the electrode potential E to tangential elastic area strain e via a thermodynamic Maxwell relation:

$$\left. \frac{\partial f}{\partial q} \right|_e = \left. \frac{\partial E}{\partial e} \right|_q. \quad (6.2)$$

The right-hand side of Equation (6.2) has been determined by Smetanin et al. [221] via cyclic deformation of a thin gold film on a polymer substrate and measurement of the potential variation. They obtained a value of -1.83 V, which is close to the surface stress charge response parameter of -2 V stated above [220]. This agreement represents an experimental confirmation of the Maxwell relation in Equation (6.2).

As an alternative to measuring the response of the electrode potential E to tangential strain e , it is also possible to determine that of the electronic work function ϕ [275]. Following the work of Lang and Kohn [276], ϕ may

be split into a surface contribution and a bulk contribution as follows:

$$\phi = V_{\text{dip}} - E_{\text{F}}, \quad (6.3)$$

where V_{dip} is the dipole barrier caused by the charge redistribution at the surface (see Figure 6.1) and E_{F} is the Fermi energy. ϕ thus defines the work needed to remove an electron from a solid to a point right outside its surface. In experimental studies including a critical evaluation of large

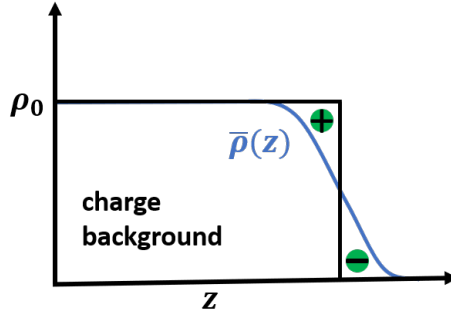


Figure 6.1.: Illustration of the dependence of the planar average of the electron density $\bar{\rho}(z)$ (blue) of the surface normal coordinate z . At a solid surface (black lines), $\bar{\rho}(z)$ does not abruptly drop to zero, but creates a dipole by spilling out of the surface. Positive and negative charges are indicated in green.

amounts of experimental data [277, 278], a mathematical relation between the work function of a neutral metal surface in vacuum and its potential of zero charge¹ has been established. Hence, the response parameter ς can be calculated from the work function strain response of a neutral surface without considering an electrolyte in the model system [275]:

$$\varsigma = q_0^{-1} \left. \frac{\partial \phi}{\partial e} \right|_{q=0}, \quad (6.4)$$

where q_0 is the elementary charge $1.6022 \cdot 10^{-19}$ C.

A dependence of the work function on strain was already found experimentally for Al, Ti and Fe alloys, albeit mainly in the plastic regime [279, 280].

¹The potential of zero charge (pzc) represents a characteristic value of the electrode potential for a metal, at which its clean surface does not acquire any electrical charge when coming into contact with an electrolyte.

Several results for the work function strain response for copper surfaces exist in the literature. Experimental work employing a scanning Kelvin probe revealed a decrease in the work function for tensile strain and an increase for compression in the elastic regime [281]. Sekiba et al. [282] also obtained a linear increase of the work function of copper under compressive strain via first principles calculations. They explained their findings by electrons spilling out of a compressed surface, which increase the surface dipole and thereby the work function. Additional calculations for the copper work function under different types of strain were carried out by Wang et al. [283], who obtained the largest response parameters for a biaxial and triaxial strain state. To interpret their results, they separated the work function into two components: the intrinsic bulk electronic structure and the surface dipole barrier. For the strain states mentioned above, both the bulk component and the dipole barrier varied more strongly than for uniaxial strain. These results hint at the importance of modeling a realistic strain state, which is never purely uniaxial due to lateral contraction or expansion. More recently, Albina et al. [225] calculated strain response parameters for various $4d$ and some $3d$ and $5d$ metals. They attributed larger surface stress charge coefficients for close-packed surfaces to the smoothing effect suggested by Smoluchowski [284]². In addition, they obtained a parabolic dependence of the response parameter on the d -band occupancy and also suggested a second parabola for the dependence of the s -orbital occupation. For the most close-packed surfaces, they calculated response parameters ranging from -1 V to -2.5 V, and for the (100) surfaces of a selection of fcc metals from -0.25 V to -0.75 V.

A connection between a shift of the d -bands resulting from lattice strain and the catalytic activity was presented by Mavrikakis et al. [285] and Kibler et al. [286]. The former describe a linear correlation between the d -band center shift and adsorption energies.

Consequently, a metal's catalytic activity can be altered by applying strain to it, possibly even tailored to a specific application. A potential application may be a chemical switch, where adsorption can be inhibited completely for a certain applied strain, while it may reach a maximum for a different value

²The "smoothing effect" proposed by Smoluchowski in 1941 [284] suggests a flattening of the electron cloud at the surface of a metal by a charge flow from the "hills" to the "valleys", which decreases the work function of the surface. Positive (tensile) strain on the surface reduces the smoothing effect, while negative (compressive) strain enhances it. For close-packed surfaces, this reduction/enhancement is more pronounced than for loosely-packed surfaces, leading to a larger sensitivity of the work function to an applied strain.

of applied strain.

For nanoporous gold (npAu), the response of the electrode potential to an applied macroscopic strain was obtained in two different approaches by Stenner et al. [287]: by quasi-static actuation experiments and by measuring potential and strain amplitudes in sensing experiments. Both strategies yielded the same response parameters around -21 mV, thus two orders of magnitude smaller than the values reported for bulk gold surfaces [220, 272, 275]. The difference in coupling parameters obviously originates from the sponge-like structure of npAu. Depending on structural parameters like ligament length and width, interconnectivity and homogeneity of the network, a macroscopic deformation may couple into local strain in the ligaments in many different ways. Ligament bending or buckling may result in both tensile and compressive strains, causing a partial canceling of the response.

Even without an applied macroscopic deformation, the npAu ligaments are inherently strained as a consequence of the surface stress reducing the interatomic spacing in the surface plane [288]. In a transmission electron microscopy (TEM) study, Mahr et al. [289] presented spatially resolved measurements of local lattice strain in dealloyed npAu samples. As previously predicted theoretically [288], they reported compressive strain values along the axis of cylindrically shaped ligaments and expansion in radial direction. Furthermore, they observed an inward relaxation of the topmost layers of the curved surfaces. Considering the results reported above, the catalytic activity at npAu ligament surfaces should not be equivalent to that of the bulk surface, as their strain state is different.

In an experimental study, Mahr et al. [77] employed energy dispersive X-ray spectroscopy (EDXS) to analyze the distribution of residual silver in the npAu ligaments. They observed silver-rich clusters both inside the ligaments as well as on the ligament surface, and they reported that the formation of these clusters is more likely for lower residual silver concentrations. While the influence of lattice strain on the catalytic activity has been thoroughly investigated for gold – experimentally [220, 272] and theoretically [275] – no results exist for the electromechanical coupling at Ag-Au alloy surfaces. Both the experimental observations by Mahr et al. [77] and the present results for oxygen-covered Ag-Au surfaces (see Chapter 5) indicate that silver should be present at the npAu ligament surface during catalytic processes. Hence, analyzing the influence of residual silver and its potential configurations within

the surface layers on the electromechanical coupling behavior may be of interest for the npAu community, as it may affect the sensing/actuation properties.

6.2. Computational details

In the preceding Chapter 5, the configuration of adsorbate-free and oxygen-covered Ag-Au surfaces was investigated via a combination of density functional theory (DFT) calculations and cluster expansions (CE). Here, these results are combined with a CE for the electromechanical coupling coefficients for the Ag-Au (111) surface with $L1_2$ bulk structure. For this purpose, the response of the work function to tangential area strain has been calculated for a large number of the CE input structures from the surface segregation cluster expansion. As the coupling coefficient also represents a quantity that only depends on the configuration of the two constituent metals, it can as well be expanded in a CE. This way, the present work addresses the question of how ζ is influenced by a varying Ag surface concentration and configuration.

Figure 6.2 illustrates the two different types of strain that were applied to the (111) surface slabs with the atomic coordinates as obtained after the two relaxation steps described in Subsection 5.4.1. In a first step, a tangential in-plane area strain ϵ in two perpendicular directions was employed, which is defined as the relative change in area ΔA with respect to the original area A_0 (see Figure Figure 6.2a). Consequently, the strained lattice constant a is calculated as follows:

$$a = \sqrt{1 + \epsilon} \cdot a_0, \quad (6.5)$$

where a_0 is the equilibrium lattice constant. In this case, the layer distances were kept fix, so that the atomic coordinates along the surface normal remained unchanged. Small values for ϵ of $\pm 1\%$, $\pm 2\%$ and $\pm 4\%$ were applied, as in this strain regime the work function strain response is expected to be linear and the coupling coefficient can be obtained from the slope.

Second, a more realistic strain state was considered by including lateral contraction as well as additional surface relaxations. Therefore, Ag-Au bulk cells with $L1_2$ structure were subjected to the tangential strain mentioned above in the (111) plane and their equilibrium layer distances were determined via a Murnaghan fit (see Figure 6.3). From the slope of the line, the Poisson ratio ν , which is defined as the ratio of transverse strain to axial

strain, can be derived. The obtained value of $\nu = 0.45$ for the Ag-Au L1₂ bulk structure should be an intermediate value of the constituents' Poisson ratios. This assumption agrees well with literature values for Au, which range from 0.42 for polycrystalline samples [290] to 0.52 for (111) gold films [291], as well as the Poisson ratio of polycrystalline Ag of 0.37 [292]. With the definition of the in-plane strain from above and the Poisson ratio ν , the new layer distances d including lateral contraction/expansion are defined as follows:

$$d = -\frac{\sqrt{1 + \epsilon} - 1}{\nu} d_0, \quad (6.6)$$

where d_0 is the original equilibrium layer distance and ϵ is the tangential in-plane strain.

In addition to the adjusted layer distances, the upper four layers were allowed to relax again until the forces upon the atoms reached a value of $0.01 \text{ eV}\text{\AA}^{-1}$. All other VASP parameters remained the same as for the segregation input calculations. However, for all calculations in this chapter, the surface slabs contained six instead of only two bulk layers. This was necessary to obtain the dipole potential V_{dip} , which is defined as the difference between the vacuum potential V_{vac} right outside the surface and the plane-averaged local electrostatic potential within the bulk layers of the slab V_{ave} . Determining V_{ave} from six bulk layers resulted in more accurate values and a linear increase of V_{dip} with strain.

The second quantity to calculate the work function ϕ of the surface slabs, apart from the dipole potential, is the Fermi energy E_{F} . Fall et al. [293] discussed the slow convergence of the work function of metals with slab thickness due to quantum-size effects. In order to avoid more costly calculations with a large number of bulk layers, the Fermi energy was taken from bulk calculations in the present work. The in-plane strain in the (111) plane and the transverse contraction/expansion were accordingly applied to the bulk cells with L1₂ structure.

Figure 6.4 illustrates the plane-averaged local electrostatic potential of a surface slab with six bulk and four surface layers over the surface normal direction. The quantities mentioned above are indicated by colored lines and arrows, and the position of the atomic layers are shown by gray atoms. Within the vacuum region, a step in the potential can be seen that results from the artificial charge at that position from the dipole correction.

Table 6.1 presents the work function of the unstrained Ag-Au (111) sur-

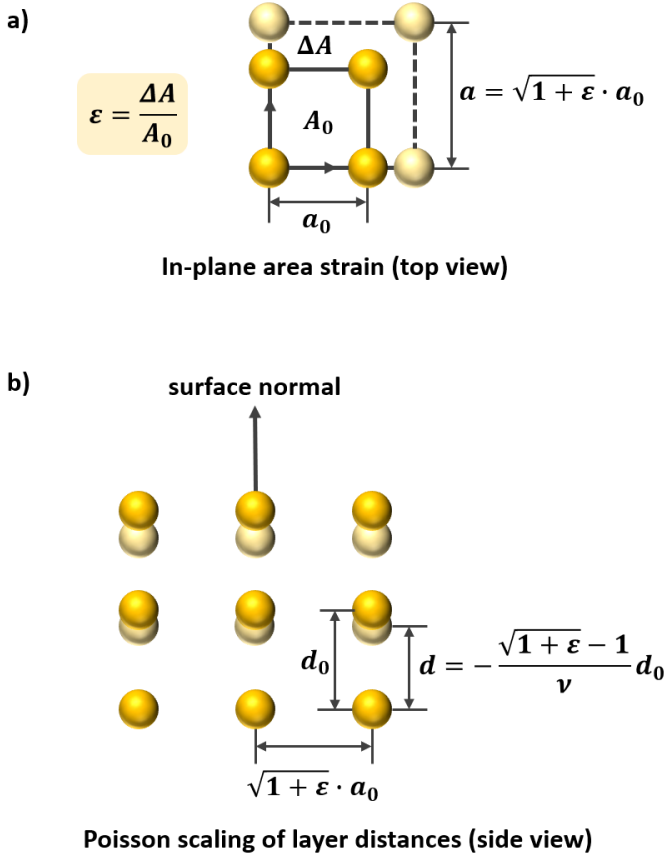


Figure 6.2.: Illustration of the strain applied to the surface slabs for the example of a simple cubic lattice. The in-plane area strain (a) is defined as the relative change in area ΔA with respect to the original area A_0 . Arrows indicate the direction of the deformation and the equilibrium and deformed lattice constants a_0 and a , respectively, are indicated. In a next step, the layer distances were scaled employing the Poisson ratio ν (b). The original layer distance d_0 as well as the scaled one d are indicated.

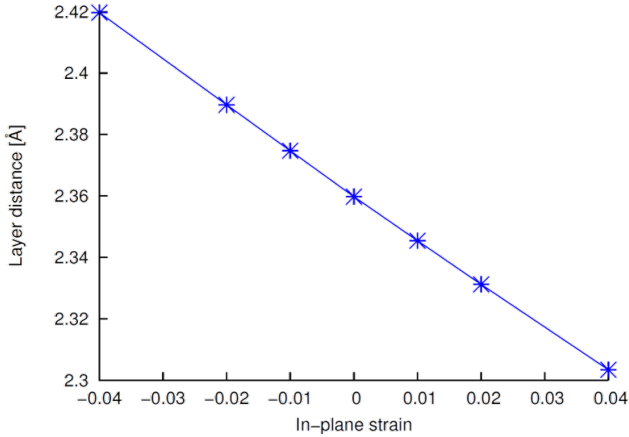


Figure 6.3.: Equilibrium layer distances determined from deformed bulk cells subjected to in-plane strain in the (111) plane.

face with $L1_2$ bulk layers and the configuration of the surface layers that was identified as the ground state in Section 5.4.1: a pure Au surface layer, Ag-enriched subsurface layer and bulk-like third and fourth layer. For comparison, literature values for the work functions of the pure Ag (111) surface and the pure Au (111) surface are given. The present result lies slightly closer to that of pure Au than to that of pure Ag, which may be due to the pure Au surface layer. In general, the here obtained work function seems to be in good agreement with literature values.

Table 6.1.: Work function ϕ of the unstrained Ag-Au (111) surface with $L1_2$ bulk, a pure Au surface layer and Ag-enriched subsurface layer in comparison to literature values for the pure Ag and Au (111) surfaces. Present results are marked by an asterisk.

Type of surface	Work function ϕ [eV]	Method	Reference
AgAu ₃ (111)	5.19	DFT-PBE+D3	*
Ag (111)	4.85	DFT-LDA	[294]
Ag (111)	4.46	Experiment	[295]
Au (111)	5.54	DFT-LDA	[294]
Au (111)	5.26	Experiment	[296]

Since in-plane strain values of $\epsilon = \pm 4\%$, $\pm 2\%$, $\pm 1\%$ were employed, six calculations had to be carried out for each CE input structure to obtain

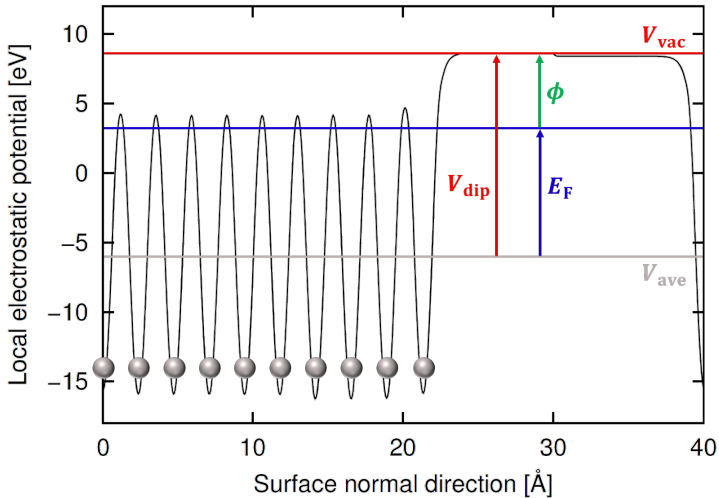


Figure 6.4.: Illustration of the plane-averaged local electrostatic potential of a surface slab with six bulk and four surface layers over the surface normal direction and the necessary quantities to determine its work function ϕ (green). The positions of the atomic layers are indicated by gray atoms.

the electromechanical coupling coefficient ς . The linear fits of both the bulk Fermi level and the surface dipole potential possessed very small fitting errors of around and up to 0.05 eV. This was necessary to obtain significant results, as especially for the pure in-plane strain without transverse contraction, ς represents a small value, emerging from the difference of two large negative quantities. Due to the high computational cost, not all 103 input structures from the CE in section 5.4.1 were considered in this study, and priority was given to those close to the ground-state line. Therefore, both cluster expansions are probably not converged yet, but the trend and the qualitative result stayed the same after adding new structures, even for a very small input. The results presented here were obtained from 49 input structures for the pure in-plane strain and 47 input structures for additional transverse contraction and surface relaxation. In both cases, up to 6-body interactions and up to 30 clusters were employed for the CE fit. The cross validation scores of $S_{CV} = 0.006$ V and $S_{CV} = 0.010$ V, respectively, indicate a highly representative fit quality.

6.3. Results on electromechanical coupling

The employed CE algorithms in UNCLE enumerate all possible surface configurations for the surface stability CE in section 5.4.1 and for the present CE in the same manner, making it very simple to combine the two outputs in one diagram. Figure 6.5 presents the results for the electromechanical coupling coefficients for pure in-plane strain for the Ag-Au (111) surface with $L1_2$ bulk structure. Basically, the diagram in Figure 6.5a is the same as the surface stability diagram in Figure 5.4, only that here, the coupling coefficient ς is included via a color coding. While dark and purple colors represent a more pronounced coupling with larger negative values, orange and yellow colors show weaker coupling. Two trends can be observed in the diagram: First, the coupling coefficient attains a larger magnitude for an increasing silver surface concentration $x_{\text{Ag}}^{\text{surf}}$. This may be expected, as the coupling for the pure silver surface is stronger than that of the pure gold surface (-1.72 V and -0.70 V, respectively). Second, a weaker electromechanical coupling is obtained closer to the ground-state line of the surface stability diagram. This arises because structures with a gold-rich surface layer have been determined to be thermodynamically more stable than silver-terminated configurations in section 5.4.1 for the clean Ag-Au (111) surface.

As an example, three surface configurations at the same Ag surface concentration $x_{\text{Ag}}^{\text{surf}} = 25\%$ with different surface formation enthalpies are depicted in Figure 6.5b along with their coupling coefficients ς . Clearly, the surface configuration and especially that of the topmost surface layer have a strong influence on the magnitude of ς . However, it stays a negative quantity in all cases. Compared to the calculated values for pure gold of -1.86 V [275] and pure silver of -2.31 V [225], the coupling coefficients obtained in this work have a quite small magnitude. This may be due to the unrealistic strain state of pure in-plane strain, which was also reported to result in a weaker electromechanical coupling for aluminum surfaces than the presence of additional transverse contraction [297].

The results for in-plane strain with additional transverse contraction and relaxation of four surface layers are presented in Figure 6.6. In the surface stability diagram with included coupling coefficients (Figure 6.6a), similar trends as for the pure in-plane strain can be observed, though they are less pronounced here. This may be due to an insufficient number of input structures, or it may be caused by the different strain state. A striking feature are

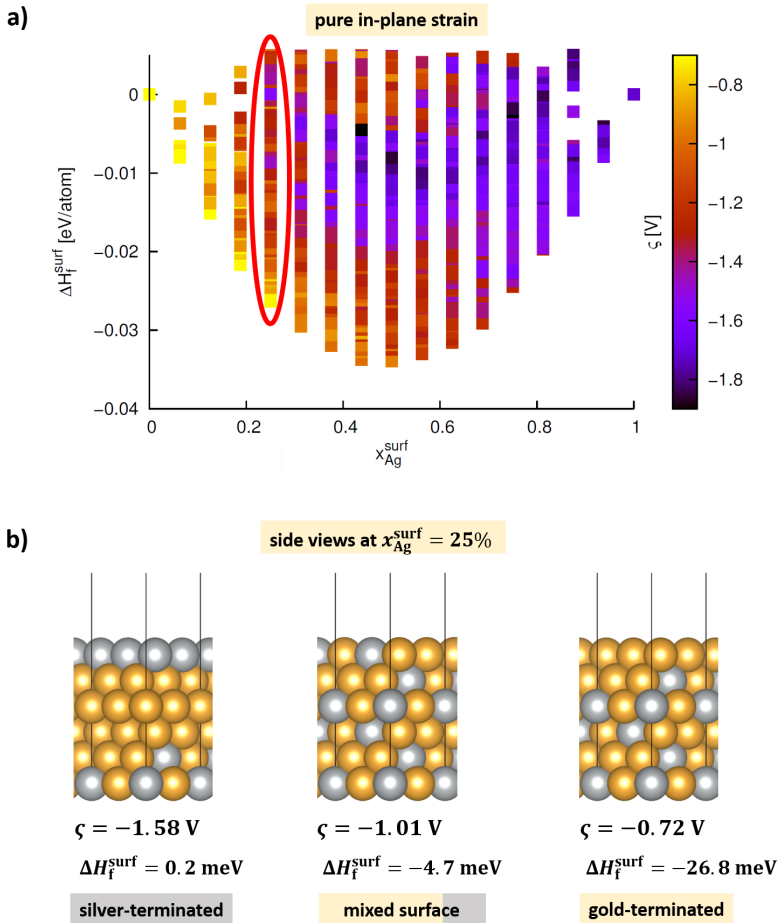


Figure 6.5.: Surface stability diagram with electromagnetic coupling coefficients for pure in-plane strain included via a color coding (a). Three example surface configurations at $x_{\text{Ag}}^{\text{surf}} = 25\%$ (marked in red in the diagram) are shown with their respective coupling coefficients ζ below the diagram (b). Au atoms are depicted in gold, Ag atoms in gray.

the large negative magnitudes of the electromechanical coupling coefficients. Interestingly, they are about twice as large as the coefficients reported above for pure gold and silver. Intuitively, one may expect the coefficients for the alloy to lie somewhere between those of the pure metals. This deviation may originate from the choice of the D3 correction to the PBE functional, which results in accurate equilibrium lattice constants and surface energies, but performs worse than pure PBE regarding surface relaxations (see Tables 5.1 and 5.2) and may result in different energetics. Since the applied strain values are small, a slight variation in the calculated Fermi energies and surface dipoles possibly results in a large difference for the coupling coefficients. A comparison of the surface relaxation of the first four surface layers of a gold-terminated and a silver-terminated surface, respectively, revealed that the uppermost silver atoms tend to relax inward of the surface under tensile in-plane strain, while gold atoms move slightly out of the surface under tensile in-plane strain.

In Figure 6.6b, the same structures and in Figure 6.5b are shown with their coupling coefficients for additional transverse contraction and surface relaxation. Though the magnitudes are larger for all three, the hierarchy stays the same, with the strongest response for the Ag-terminated surface and the weakest response for the Au-terminated one.

To analyze the origin of the different magnitudes of the coupling coefficients, it should be noted that according to Equation (6.3), the response can be divided into the surface contribution of the surface dipole potential V_{dip} and the bulk contribution of the Fermi energy E_{F} . Table 6.2 shows the response of the work function ϕ , the surface dipole potential V_{dip} and the bulk Fermi energy E_{F} to the two applied types of strain for the ground-state configuration at $x_{\text{Ag}}^{\text{surf}} = 25\%$. All responses are negative, and the electromechanical coupling coefficient, i.e. the response of ϕ , emerges as the difference of two larger negative quantities. Considering the response of the bulk Fermi energy, it is much more pronounced for pure in-plane strain than when a transverse contraction is taken into account. This behavior may be due to a larger volume change for pure in-plane strain, resulting in a decreased electron density and a more strongly affected electronic structure. A larger increase in volume may also lead to a decreased surface dipole and may therefore be responsible for the stronger response of the dipole potential to pure in-plane strain.

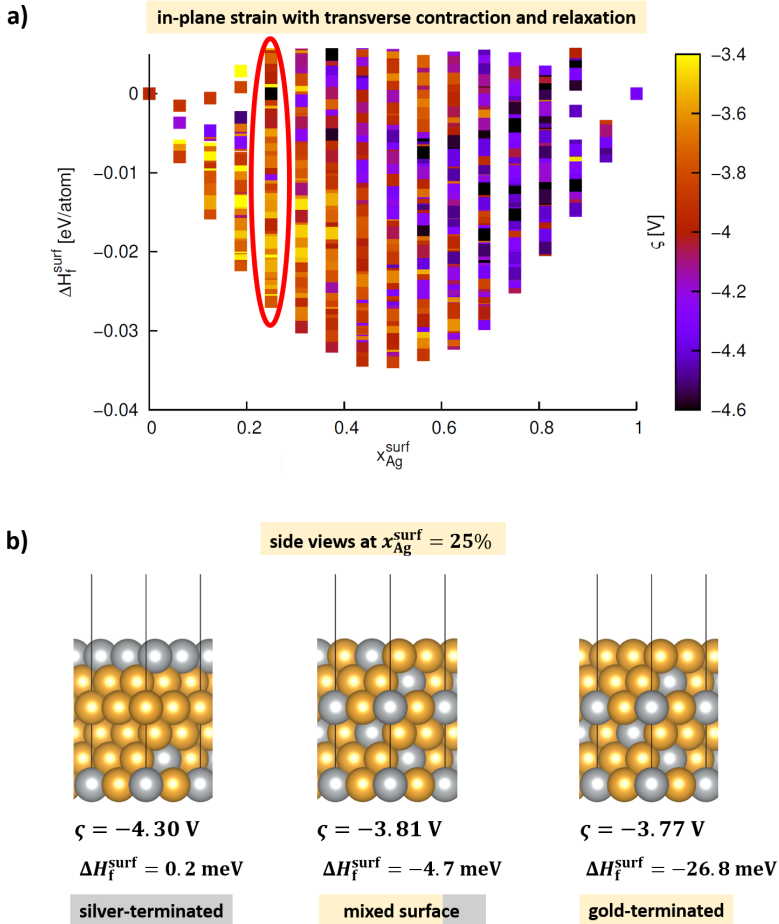


Figure 6.6.: Surface stability diagram with electromagnetic coupling coefficients for in-plane strain with additional transverse contraction and relaxation of four surface layers included via a color coding (a). Three example surface configurations at $x_{\text{Ag}}^{\text{surf}} = 25\%$ (marked in red in the diagram) are shown with their respective coupling coefficients ζ below the diagram (b). Au atoms are depicted in gold, Ag atoms in gray.

Table 6.2.: Response of the work function ϕ , the surface dipole potential V_{dip} and the bulk Fermi energy E_{F} to pure in-plane strain ϵ and to in-plane strain with additional transverse contraction and surface relaxation (ϵ +relax). All values are given in eV.

Type of strain	Response of...		
	ϕ	V_{dip}	E_{F}
ϵ	-0.71	-17.00	-16.26
ϵ +relax	-3.77	-9.99	-6.22

In the present chapter, the electromechanical coupling behavior of the Ag-Au (111) surface with L1₂ bulk structure has been analyzed for two different strain states. Qualitatively, the observed trends agree with intuitive expectations, for example regarding the stronger response for Ag-terminated surfaces than for Au-terminated ones. On the other hand, the magnitudes of the calculated response parameters appear too large, which may be due to the chosen exchange-correlation functional. In a next step, it would therefore be interesting to compare the present results to those obtained applying the pure PBE or LDA functional.

LEED structure analysis and results

"Today's scientists have substituted mathematics for experiments, and they wander off through equation after equation, and eventually build a structure which has no relation to reality."

- Nikola Tesla

The segregation results for the Ag-Au surfaces presented in Chapter 5 of this work stand in contrast to several experimental and theoretical studies from the past, among them also a low-energy electron diffraction (LEED) analysis (see Section 4.3 of the Ag-Au (100) surface [108]). Therefore, a LEED structure analysis was carried out in cooperation with the experimental group of Prof. Dr. Schneider with the help of Dr. Lutz Hammer at the Friedrich-Alexander-Universität Erlangen-Nürnberg for a Ag-Au (111) surface. This way, the calculated segregation profile from this work could be compared directly to experimental results for the same surface orientation and a controlled silver bulk concentration. In this chapter, the obtained experimental results are presented and discussed.

The LEED experiment was carried out in cooperation with the Chair of Solid State Physics at the Friedrich-Alexander-Universität Erlangen-Nürnberg. For this purpose, disc-shaped Ag-Au samples with (111) surface orientation, a nominal composition of 75% Au and 25% Ag and the dimensions of 8 mm diameter and 1.5 mm thickness were ordered from MaTeck GmbH. Before the actual LEED measurements, the surface purity of the crystal may be checked,

for example via scanning tunneling microscopy (STM). For the present work, no atomic resolution was achieved in STM measurements of the Ag-Au (111) surface. However, larger STM pictures revealed steps in the order of 100 nm with a clean surface. Employing DFT calculations, it is possible to simulate STM micrographs at different bias voltages in order to compare possible structures to the experimental outcome or interpret the measurements. This was done here for the $L1_2$ ordered structure and the obtained ground state at a silver surface concentration of 25% with a Au surface layer and 50% Ag in the subsurface layer (see Figure 5.4). The obtained STM pictures at a bias voltage of -500 meV are presented in Figure 7.1. For the $L1_2$ ordered surface (Figure 7.1a), the silver atoms appear less bright and therefore less high than the gold atoms. For the calculated ground state at $x_{\text{Ag}}^{\text{surf}} = 25\%$ (Figure 7.1b), one Au atom in the surface unit cell appears brighter than the other three. This is probably because it is adjacent to only one Ag atom in the subsurface layer, while the other three Au atoms are adjacent to two Ag atoms in the subsurface layer.

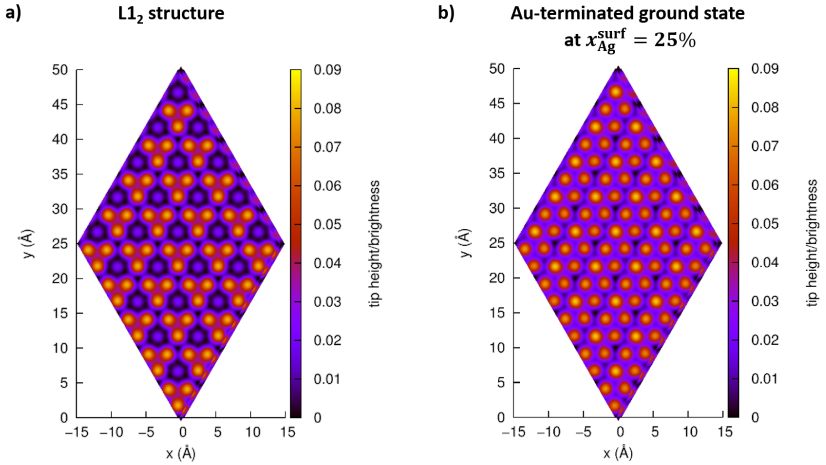


Figure 7.1.: Simulation of STM pictures at a bias voltage of -500 meV for the $L1_2$ ordered structure (a) and the obtained ground state at a silver surface concentration of 25% (b). The color coding indicates the tip height.

All LEED intensity measurements were made with normal incidence of the primary beam on the sample. The latter was cooled down to less than 100 K to keep the thermal background intensity at a minimum. In order to

ensure a distribution of the elements corresponding to thermodynamic equilibrium, different annealing temperatures were employed and held for 2 min, respectively, before the sample was cooled again slowly. Figure 7.2 compares the $I(E)$ curves of the (10) beam for four different annealing temperatures in the range between 200 °C and 700 °C. For higher annealing temperatures, the peaks become larger and their features more pronounced. On the whole, the spectra changed only slightly with varying annealing temperature and no qualitative change was observed between 400 °C and 700 °C. For the intensity measurements in this work, the sample was annealed at 700 °C to obtain sharp peaks in the $I(E)$ curves. The LEED patterns were then recorded with a CCD camera in the primary beam energy range of 50 – 600 eV. As the energy increases, the LEED spots move towards the center and more maxima appear at the edge. Figure 7.3 shows a snapshot of the hexagonal LEED pattern at an energy of 139 eV and indicates the surface unit cell. To ensure consistency of the results, two sets of data were recorded for the same sample and both were fitted to theoretical spectra with the TensErLEEED program.

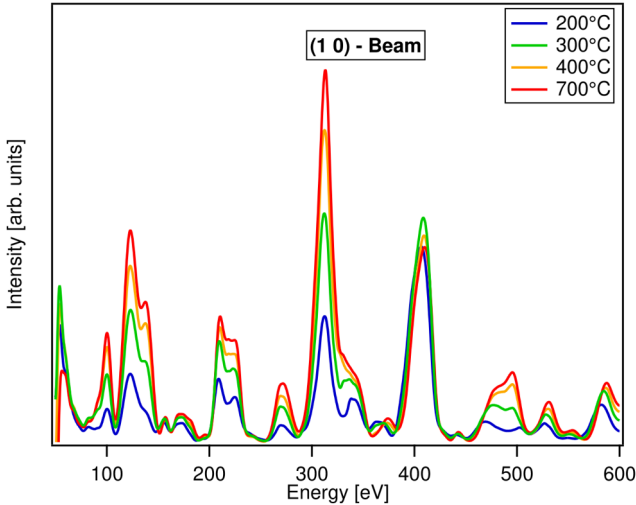


Figure 7.2.: Intensity vs. energy ($I(E)$) spectra of the (10) beam for different annealing temperatures of the sample.

After the actual intensity measurement, the integral spot intensities as a

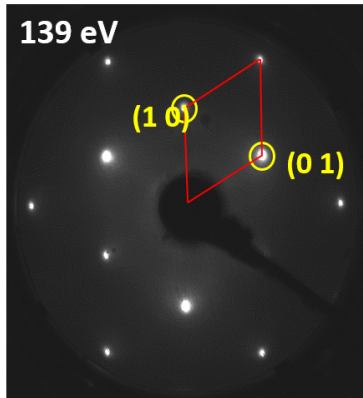


Figure 7.3.: LEED pattern at a primary beam energy of 139 eV. The surface unit cell is indicated.

function of the energy, i.e. the $I(E)$ curves, were created by tracing the intensity maxima over the whole energy range in an offline evaluation for all accessible beams. For both sets of data, ten beams were included in the evaluation. The spectra were subsequently smoothed to remove residual noise and curves of equivalent beams were averaged. The background-corrected curves were then normalized by the primary beam current.

In the TensErLEED calculation of the theoretical spectra, phase shifts of up to $l_{max} = 14$ were employed and electron attenuation was simulated by an optical potential which was fitted to $V_{0i} = 5.2$ eV for the first set of data and to $V_{0i} = 4.9$ eV for the second set of data. The angle of incidence of the primary beam was also determined within the fitting process to be 0.5° for the first set of data and 0.45° for the second one. The weighted average lattice parameter of 4.068 \AA was used for the Au_3Ag lattice and analogous to the model calculations from this work, four surface layers were implemented in the program. The parameters to be fitted were the concentrations of Ag and Au within the four surface layers, their vertical positions and vibrational frequencies. In order to identify the structure with the best agreement between theoretical and experimental $I(E)$ spectra, a more rough fit was carried out first, followed by a fit with a finer mesh around the former best-fit configuration.

The TensErLEED fit revealed slight differences between the results for the two sets of data. Their Pendry R-factors were determined to be $R_P =$

0.0645 ± 0.008 and $R_P = 0.0754 \pm 0.008$, respectively, indicating an excellent fit quality. Figure 7.4 presents the experimental (in red) and theoretical (in blue) $I(E)$ curves for eight of the ten investigated beams of the first data set and for theoretical results from the best fit configuration. As these diagrams look very similar for the second data set, they are included in the Appendix C. In each diagram of Figure 7.4, the type of beam and the R-factor for that particular beam are given. As described for the Ewald sphere construction, more diffraction spots appear with increasing electron energy of the primary beam, which is why the $I(E)$ curves for higher order beams only start at higher energies.

Regarding the concentration of silver and gold within the first four surface layers, the results for the best fit configurations for both data sets are shown in Figure 7.6. In both cases, a silver enrichment in the subsurface layer was obtained. For the first set of data, the surface layer is gold-enriched with a Au concentration of $x_{\text{Au}} = 82\%$. For the second data set, the surface layer was determined to have a bulk-like Au concentration of 76%. The third and 4th layer exhibited the nominal bulk concentration for both data sets.

Figure 7.5 shows example error curves for the Pendry R-factor R_P for the second data set for different Ag concentrations in the surface and subsurface layer, respectively. The concentration error may be determined by the curve for the R-factor and the sum of the best-fit R-factor $P_{R,min}$ and its variance R_{var} (black line in Figure 7.5). This results in a Ag concentration of about $24 \pm 3\%$ in the surface layer and about $42 \pm 4\%$ in the subsurface layer. In theory, the best fit would have to be determined at every concentration to obtain the all-parameter error. However, the latter usually deviates only slightly from the one-parameter error, especially for a simple surface like the Ag-Au (111) surface.

Even if the gold enrichment in the surface layer, which resulted from the theoretical segregation study in this work, was only obtained for the first set of data, the silver enrichment in the subsurface layer and the bulk-like third and fourth layer are consistent with the results from this work. This segregation profile has not been reported in former experimental studies of Ag-Au surfaces (see Chapter 3). Furthermore, the concentrations within the layers determined in the LEED structure analysis agree well with the theoretically obtained ground-state at a silver surface concentration of $x_{\text{Ag}}^{\text{surf}} = 31.25\%$, which is labeled as Structure 5999 in the CE (see Section 5.4.1).

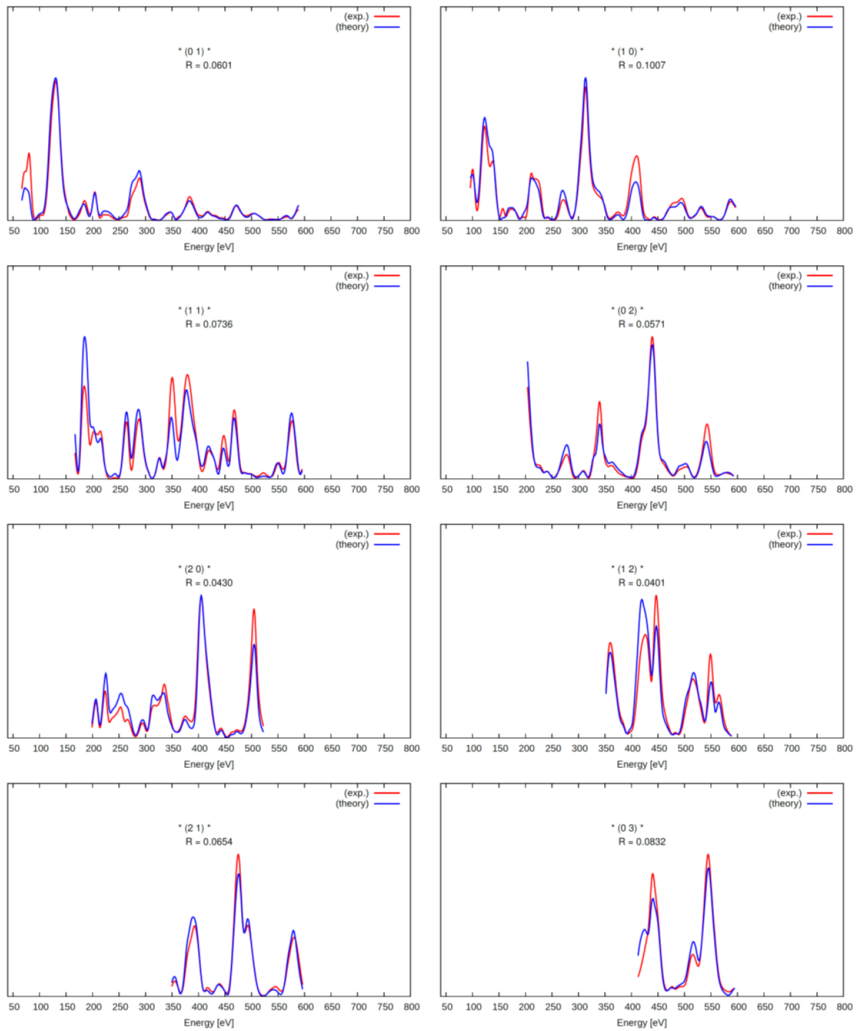


Figure 7.4.: Comparison between experimental (red) and theoretical (blue) $I(E)$ curves for eight of the investigated ten beams. The type of beam and R-factor are given in the diagrams.

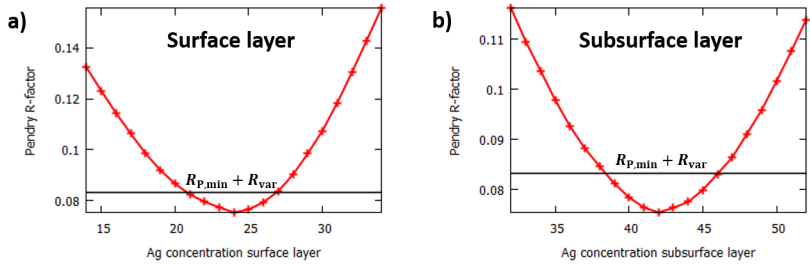


Figure 7.5.: Pendry R-factor R_P for different silver concentrations in the surface layer (a) and the subsurface layer (b). The black line indicates the sum of the best-fit Pendry R-factor $R_{P,min}$ and the variation of the latter. The error in silver concentration can then be determined from the intersection points of the two curves.

The latter exhibits a silver concentration of 50% in the subsurface layer, while the surface layer and the third and fourth layer have the nominal bulk silver concentration of 25%. As the underlying bulk may be regarded as an infinite reservoir of both Ag and Au atoms, silver atoms can diffuse towards the surface and the overall silver concentration within the first four surface layers may also be larger than the nominal bulk concentration.

Figure 7.7 compares the first four layer distances obtained in the LEED structure analyses for the two sets of data to the L_{12} structure, which corresponds to the bulk configuration, and the ground state determined in the CE in Section 5.4.1 at a silver surface concentration of $x_{Ag}^{surf} = 31.25\%$ (Structure 5999). The diagram shows that the first layer distance between surface and subsurface layer is much larger for the L_{12} structure than that determined from the LEED structure analyses. The layer distances of the ground-state configuration Structure 5999, however, agree very well with both sets of LEED data. The buckling between the Au atoms and the Ag atom within the surface layer was 0.07 \AA for both sets of LEED data, as compared to 0.06 \AA for the L_{12} structure and 0.05 \AA for Structure 5999.

At the surface, thermal vibrations are usually more pronounced than in the bulk due to missing atomic bonds. Therefore, the vibrational amplitudes were fitted separately for the atoms within the surface layer and the underlying layers (here referred to as bulk). The results for the best fit configurations for the two sets of LEED data are presented in Table 7.1. In both cases,

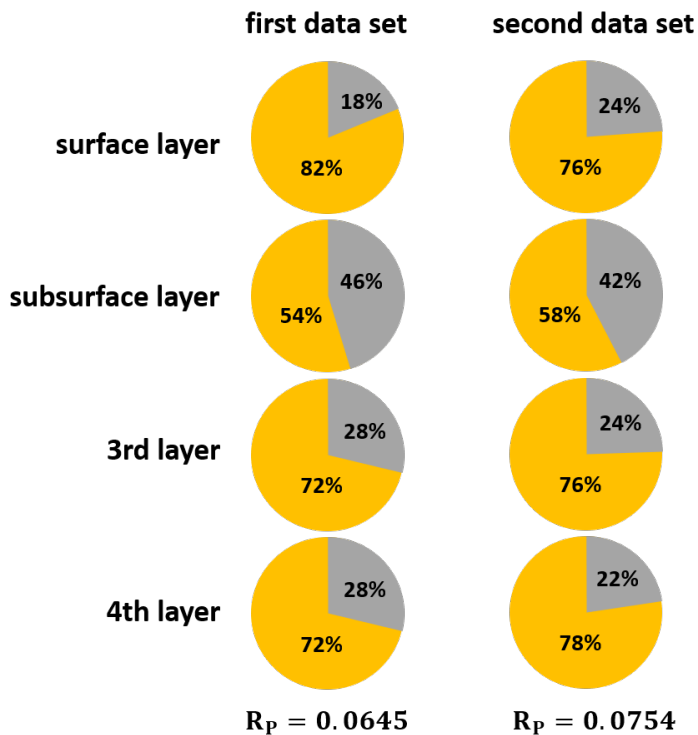


Figure 7.6.: Comparison of the silver and gold content within the four surface layers as determined in the LEED structure analysis for the two measured sets of data.

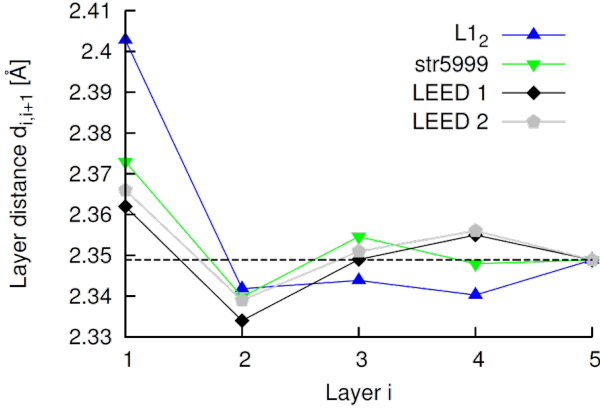


Figure 7.7.: Absolute layer distances as obtained from the two LEED fits (LEED1 and LEED2) in comparison to those from the $L1_2$ structure ($x_{\text{Ag}}^{\text{surf}} = 25\%$) and the ground state at $x_{\text{Ag}}^{\text{surf}} = 31.25\%$ (Structure 5999) determined in the CE in Section 5.4.1.

the amplitudes are larger in the surface layer than in the bulk layers as expected. However, as gold has the lower Debye temperature than silver (170 K compared to 215 K, respectively [98]), that should correspond to larger vibrational amplitudes for gold. The results obtained here stand in contrast to this expectation, and especially the vibrational amplitude of the Au bulk atoms for the first data set is rather small with only 0.0410 \AA .

Table 7.1.: Best fit results for the vibrational amplitudes u for both LEED data sets for the Au and Ag bulk and surface atoms. All values are given in \AA .

		Data set 1	Data set 2
Surface	u_{Au}	0.0950	0.1000
	u_{Ag}	0.0700	0.1000
Bulk	u_{Au}	0.0410	0.0710
	u_{Ag}	0.0745	0.0795

Taking into account that the LEED measurements were carried out at a temperature of approximately 100 K, entropic contributions may already influence the segregation profile as compared to the surface at 0 K. The Monte Carlo simulation in Section 5.4.3 predicts a silver concentration of about

12.5% within the surface layer and of about 47% in the subsurface layer, which agrees very well with the concentrations obtained from the first set of LEED data.

To conclude, the results from the LEED structure analysis corroborate the theoretical calculations for the clean Ag-Au (111) surface from the present work. Qualitatively, a silver enrichment in the subsurface layer was obtained in both cases and the first set of LEED data also indicates a gold-enriched surface layer. Both the concentrations within the first four surface layers as well as the determined layer distances agree well comparing experiment and theory.

Summary

The main goal of the present work was the investigation of silver-gold surface via modern simulation methods to develop a better understanding of the origins of the high catalytic activity of nanoporous gold (npAu). The high accuracy of density functional theory (DFT) calculations at atomic scale goes hand in hand with certain restrictions, such as the limited size of the unit cell. This method is therefore not suitable to model, for example, a whole npAu ligament and calculate the silver distribution. However, important fundamental phenomena may be explained in terms of the electron density and atomic configurations, bonding characters and energetics may be analyzed to great detail. From this, a fundamental study on selected properties of clean and adsorbate-covered Ag-Au surfaces in vacuum emerged and was presented to the reader in this work.

First, the question of where the silver atoms are located in the npAu surface was addressed. For this purpose, suitable model surfaces were selected and their segregation behavior was investigated via a combination of DFT calculations and the cluster expansion (CE) method. Both flat and stepped surfaces as well as adsorbate-free and oxygen-covered surfaces were considered in this work. For the clean Ag-Au (111) surface, gold enrichment in the topmost layer and depletion in the subsurface layer were obtained, while the silver bulk concentration was found to have only little effect on this result. Interestingly, the present findings stand in contrast to earlier theoretical and experimental studies on surface segregation in Ag-Au. However, the gold

segregation to the surface layer and silver enrichment in the subsurface layer may be explained by a charge transfer from Ag to Au, which is revealed by DFT simulations.

When adsorbed oxygen is present at the surface, this subtle charge transfer effect is dominated by strong Ag–O interactions and the segregation behavior is reversed with silver segregating to the surface layer. During catalytic processes in realistic conditions, atoms or molecules are always adsorbed on the npAu surface, which is surrounded by either a reactive gas or an electrolyte. Consequently, residual silver atoms in npAu will probably be located at the surface and actively take part in the occurring chemical reactions, and thereby influence the reactivity.

The segregation behavior for flat and stepped surfaces calculated here was qualitatively similar. Nevertheless, an interesting phenomenon was obtained for the stepped Au (321) surface with silver impurities and an infinite oxide chain going across the steps: Up to high silver surface concentrations, silver does not replace gold within the oxide chain. This is due to strong, partially covalent bonds between gold and oxygen. In addition, silver atoms adjacent to the chain seem to further stabilize gold within the chain. The present results were supported by ab initio molecular dynamics (AIMD) calculations performed at the University of Bremen.

In a next step, the electromechanical coupling was analyzed for the Ag–Au (111) surface. Nanoporous gold ligaments are known to be subjected to inherent tensile and compressive strains, which may affect the surface’s reactivity. Via DFT, the electromechanical coupling coefficient can be calculated by considering the change of the work function due to an applied strain. The present work shows that the values of the coupling coefficients for pure in-plane strain lie between those of pure gold and pure silver surfaces, respectively, and that their magnitude is dominated by the composition of the topmost surface layer. When lateral contractions and surface relaxation are accounted for, unusually large coupling coefficients were obtained. This should be further tested for different exchange–correlation functionals or adjusted DFT parameters, to check if these large values still prevail.

Finally, a low-energy electron diffraction (LEED) structure analysis for the clean Au₃Ag (111) surface was carried out in a collaboration with the Friedrich-Alexander-University Erlangen-Nürnberg. The resulting silver enrichment in the subsurface layer and possible gold enrichment in the surface

layer are in good agreement with the calculated segregation profiles. Regarding the gold and silver concentrations within the first four surface layers and the layer distances, the LEED results match a ground-state configuration resulting from the cluster expansion for the clean Ag-Au (111) surface.

The present work therefore sheds new light on very fundamental phenomena at silver-gold surfaces and combines thoroughly performed materials simulations with an experimental study that verifies the obtained predictions. Starting from the results reported here, more complex surfaces or adsorbates may be considered to gain a deeper understanding of the important reaction mechanisms during catalytic processes at npAu surfaces.



VASP input parameters

The surface unit cell configurations and some selected important input parameters for the DFT calculations were given in the main part of this work. In Tables A.1 and A.2, a more detailed list of the parameters defined in the VASP INCAR file for a static calculation and additional dipole corrections as well as relaxation parameters are provided.

Table A.1.: List of VASP input parameters from the INCAR file of a static DFT calculation.

Static calculation	Meaning
LWAVE=F	Store wave function?
LCHARG=T	Write charge densities?
ISTART=0	Read WAVECAR?
ICHARG=2	How to construct initial charge density?
PREC=ACCURATE	Precision of calculation
ALGO=F	Mixture of the Davidson and RMM-DIIS algorithms for electronic minimization
LREAL=F	Projection operators evaluated in reciprocal space
ENCUT=725	Cutoff energy
NELMIN=7	Minimum of electronic steps
NELM=40	Maximum of electronic steps
EDIFF=0.5E-7	Break condition for self-consistent electronic loop
ISMEAR=2	Smearing method
SIGMA=0.2	Width of smearing in eV
LVHAR=T	LOCPOW contains the entire local potential (ionic + Hartree + exchange correlation)
ISPIN=2	spin-polarized calculation
IVDW=11	DFT-D3 method of Grimme

Table A.2.: List of VASP input parameters for dipole corrections and relaxation.

Dipole corrections	
LDIPOL=T	Corrections to the potential?
IDIPOL=1	Dipole corrections parallel to the first lattice vector
DIPOL=0.25 0.5 0.5	Center of the cell w.r.t. which the total dipole-moment in the cell is calculated
Relaxation	
NSW=20	Maximum number of ionic steps
ISIF=2	Calculation of forces, stress tensor and atomic positions are allowed to change, while cell shape is fixed
IBRION=2	ionic relaxation via conjugate gradient algorithm
EDIFFG=-1E-2	Break condition for the ionic relaxation loop

B

Segregation results for pure Au bulk and pure Ag bulk

As reported in Section 5.4.1, the silver concentration in the underlying bulk has only little influence on the surface segregation behavior. Figures B.1 and B.2 show the surface stability diagrams and top and side views of example ground-state configurations for pure Ag bulk and pure Au bulk, respectively. Similar to the structures with $L1_2$ bulk, the surface formation enthalpies are of relatively small magnitude and there are numerous ground states along the ground-state lines in both cases. Furthermore, for the highest possible silver surface concentration $x_{\text{Ag}}^{\text{surf}} = 93.75\%$, the remaining Au atom is located in the surface layer for pure Ag bulk and pure Au bulk.

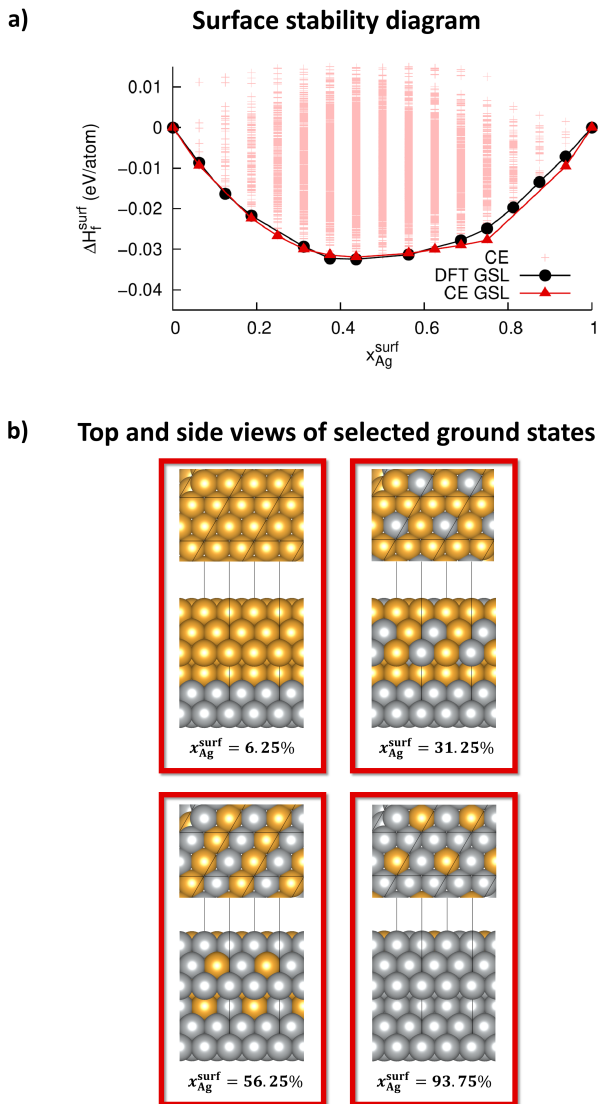
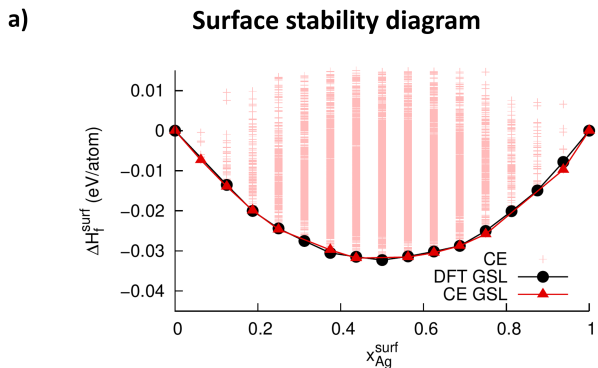


Figure B.1.: Surface stability diagram for the clean Ag-Au (111) surface with two Ag layers and four surface layers (a). Below, four example ground-state structures are depicted in top and side views (b). The surface unit cell is indicated.



b) **Top and side views of selected ground states**

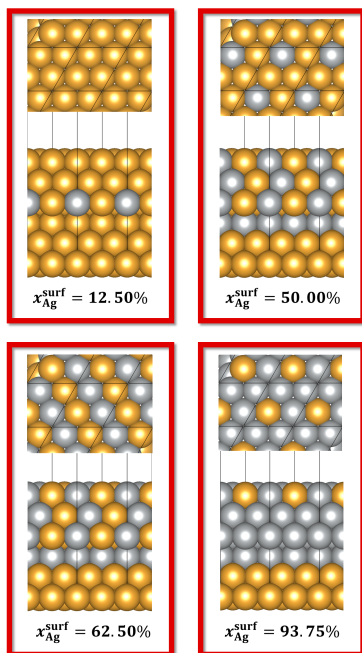


Figure B.2.: Surface stability diagram for the clean Ag-Au (111) surface with Au bulk layers and four surface layers (a). Below, four example ground-state structures are depicted in top and side views (b). The surface unit cell is indicated.



LEED intensity vs. energy spectra

Figure C.1 presents the experimental and theoretical $I(E)$ spectra for the second LEED data set as determined from LEED measurements and the TensErLEED program. The respective type of beam and the Pendry R-factor are given in the diagrams.

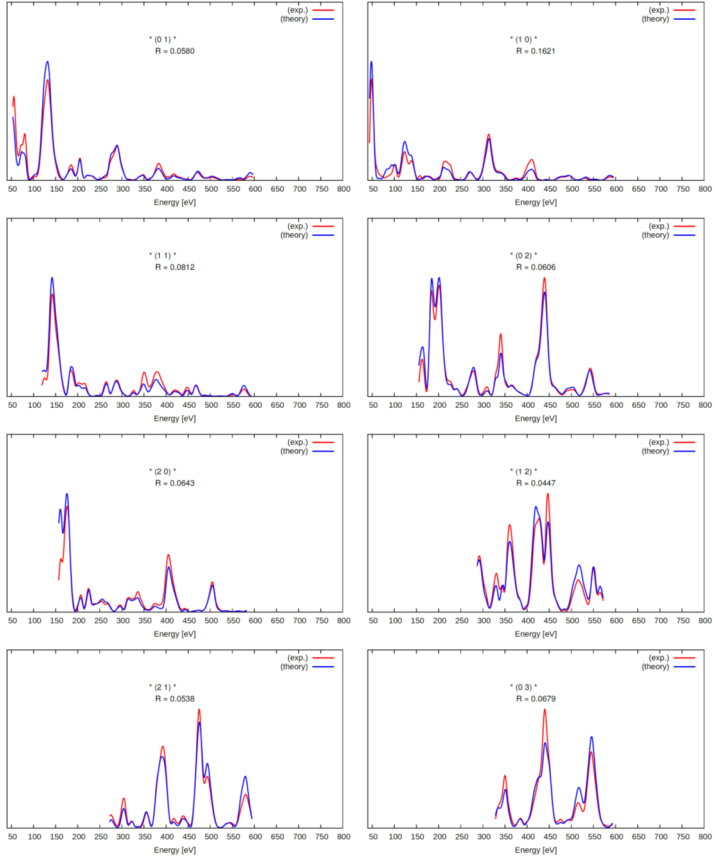


Figure C.1.: Comparison between experimental (red) and theoretical (blue) $I(E)$ curves for eight of the investigated ten beams. The type of beam and R-factor are given in the diagrams.

Acknowledgements

I would like to use this opportunity to thank some people who have helped me through the last years.

- My parents – You have supported me all the way, since I was born, through my school life, my studies and finally my PhD time. You never doubted me or judged me and I know that I can always count on you. Thank you for always being there when I need you, I hope I can do the same for you!
- My first examiner Prof. Stefan Müller – First of all, I would like to thank you for inviting me to your group back in 2011 and for awakening my interest in solid state physics and atomistic materials simulation in your lecture. Obviously, I enjoyed writing my master thesis in your group so much that I stayed for my PhD thesis and I have never regretted that decision. I am happy that through your long absence, you were able to stay my first supervisor and to take my final exam.
- My dear colleagues Sascha Maisel and Anja Michl – My second me and my former supervisor, thank you so much for introducing me to the world of density functional theory and cluster expansion and for sharing (at least some) of your vast knowledge with me! Both of you are an inspiration and I am very happy that you found each other!

- My other dear colleagues – Besides Sascha and Anja, I had the honor to work with the serious business woman Beatrix aka Trixi and the really not helpful Wolfgang. Later on, the group was further completed by sweet Kai and our Austrian connection Gregor and Wernfried. I want to thank you all for making my PhD life that much more enjoyable and always being helpful (even Wolfgang).
- The whole M-9 crew – Despite being a theoretician, I very much enjoyed spending time with the experimentalists of M-9 as well. Since I have spent quite some time at this institute, I have seen some people come and go, but I have always loved the warm and familiar atmosphere. In the beginning, I had my coffee breaks with Robert, Jefferson and Pia. Later on, I met some of the best ladies here (yes, I am talking about you, Diletta, Kaline and Berta), whom I would consider my true soulmates and Goldies forever. Furthermore, I was very lucky to have Prof. Gerold Schneider as my new boss in my position as coordinator of the SFB 986. Besides our good teamwork on a professional level, I also appreciate him very much as a person. And of course, the following people will not be forgotten: Anja, Manfred, Andrea, Yen, Alex, Pia, Büsra, Jasmin, Sanjay, Benedikt, Hans, Bärbel, Sophia, Ezgi, Sebastian and Roman.
- Dr. Lyudmila Moskaleva – Thank you for giving me advice and supporting me in a difficult time and inspiring me to successfully publish my results.
- Prof. Robert Meißner – Thank you for taking the time to be my second examiner.
- Prof. Patrick Huber – Thank you for helping me with the organization of my oral exam and leading the committee.

Bibliography

- [1] P. Hohenberg and W. Kohn. *Phys. Rev.* 136.3B (1964) B864–B871.
- [2] W. Kohn and L. J. Sham. *Phys. Rev.* 140.4A (1965) A1133–A1138.
- [3] G. Kresse and J. Hafner. *Phys. Rev. B* 47.1 (1993) 558–561.
- [4] G. Kresse and J. Hafner. *J. Phys.: Condens. Matter* 6.40 (1994) 8245.
- [5] G. Kresse and J. Furthmüller. *Phys. Rev. B* 54.16 (1996) 11169–11186.
- [6] B. Hammer and J. K. Nørskov. *Surf. Sci.* 343.3 (1995) 211–220.
- [7] Arne Wittstock, Andre Wichmann, and Marcus Bäumer. *ACS Catal.* 2.10 (2012) 2199–2215.
- [8] A. J. Smith and D. L. Trimm. *Annual Review of Materials Research* 35.1 (2005) 127–142.
- [9] Hermann Renner et al. *Ullmann's Encyclopedia of Industrial Chemistry*. Wiley-VCH Verlag GmbH & Co. KGaA, 2000.
- [10] Arne Wittstock, Jurgen Biener, Jonah Erlebacher, and Marcus Baumer. *RSC Nanoscience & Nanotechnology*. The Royal Society of Chemistry, 2012.
- [11] Arne Wittstock and Marcus Bäumer. *Acc. Chem. Res.* 47.3 (2014) 731–739.

-
- [12] Arne Wittstock, Jurgen Biener, and Marcus Baumer. *Phys. Chem. Chem. Phys.* 12.40 (2010) 12919–12930.
- [13] Olaf Deutschmann, Helmut Knözinger, Karl Kochloeff, and Thomas Turek. *Ullmann's Encyclopedia of Industrial Chemistry*. Wiley-VCH Verlag GmbH & Co. KGaA, 2000.
- [14] B. Hammer and J. K. Norskov. 376 (1995) 238 EP.
- [15] Geoffrey C. Bond, Paul A. Sermon, Geoffrey Webb, Douglas A. Buchanan, and Peter B. Wells. *J. Chem. Soc., Chem. Commun.* 13 (1973) 444b–445.
- [16] G. C. Bond and P. A. Sermon. *Gold Bull.* 6.4 (1973) 102–105.
- [17] G. J. Hutchings. *J. Catal.* 96.1 (1985) 292–295.
- [18] Masatake Haruta, Tetsuhiko Kobayashi, Hiroshi Sano, and Nobumasa Yamada. *Chem. Lett.* 16.2 (1987) 405–408.
- [19] Masatake Haruta. *Catal. Surv. Asia* 1.1 (1997) 61–73.
- [20] Markus M. Schubert et al. *J. Catal.* 197.1 (2001) 113–122.
- [21] Masatake Haruta. *CATTECH* 6.3 (2002) 102–115.
- [22] Geoffrey Colin Bond, Catherine Louis, and David T. Thompson. Vol. v. 6. Catalytic science series. London and Singapore: Imperial College Press, 2006.
- [23] Cassandra G. Freyschlag and Robert J. Madix. *Mater. Today* 14.4 (2011) 134–142.
- [24] A. Wittstock, V. Zielasek, J. Biener, C. M. Friend, and M. Bäumer. *Science* 327.5963 (2010) 319–322.
- [25] G. Patrick, E. van der Lingen, C. W. Corti, R. J. Holliday, and D. T. Thompson. *Top. Catal.* 30.1 (2004) 273–279.
- [26] Ai-Qin Wang, Jun-Hong Liu, S. D. Lin, Tien-Sung Lin, and Chung-Yuan Mou. *J. Catal.* 233.1 (2005) 186–197.
- [27] Virginia Gewin. 440 (2006) 378–379.
- [28] Jun-Hong Liu, Ai-Qin Wang, Yu-Shan Chi, Hong-Ping Lin, and Chung-Yuan Mou. *J. Phys. Chem. B* 109.1 (2005) 40–43.
- [29] Xiaoyan Liu et al. *Chem. Mater.* 21.2 (2009) 410–418.

- [30] Chun-Wan Yen et al. *J. Phys. Chem. C* 113.41 (2009) 17831–17839.
- [31] Alberto Sandoval, Antonio Aguilar, Catherine Louis, Agn?s Traverse, and Rodolfo Zanella. *J. Catal.* 281.1 (2011) 40–49.
- [32] Yasuo Iizuka et al. *Catal. Lett.* 97.3/4 (2004) 203–208.
- [33] Graham J. Hutchings. *Catal. Today* 100.1-2 (2005) 55–61.
- [34] Thierry Déronzier, Franck Morfin, Marc Lomello, and Jean-Luc Rousset. *J. Catal.* 311 (2014) 221–229.
- [35] Isabel Xiaoye Green, Wenjie Tang, Matthew Neurock, and John T. Yates. *Science* 333.6043 (2011) 736.
- [36] Lu-Cun Wang et al. *Beilstein J. Nanotechnol.* 4 (2013) 111–128.
- [37] Takeshi Fujita et al. *Nat. Mater.* 11.9 (2012) 775–780.
- [38] Volkmar Zielasek et al. *Angew. Chem. Int. Ed.* 45.48 (2006) 8241–8244.
- [39] Juergen Biener et al. *Nano Lett.* 6.10 (2006) 2379–2382.
- [40] Arne Wittstock et al. *J. Phys. Chem. C* 113.14 (2009) 5593–5600.
- [41] R. C. Newman, S. G. Corcoran, J. Erlebacher, M. J. Aziz, and K. Sieradzki. *MRS Bull.* 24.7 (1999) 24–28.
- [42] A. J. Forty. 282 (1979) 597 EP.
- [43] Satoshi Kameoka and An Pang Tsai. *Catal. Lett.* 121.3 (2008) 337–341.
- [44] Xiaoguang Wang, Zhen Qi, Changchun Zhao, Weimin Wang, and Zhonghua Zhang. *J. Phys. Chem. C* 113.30 (2009) 13139–13150.
- [45] Zhonghua Zhang et al. *J. Phys. Chem. C* 113.29 (2009) 12629–12636.
- [46] Erkin Seker, Michael L. Reed, and Matthew R. Begley. *Materials* 2.4 (2009) 2188–2215.
- [47] Jonah Erlebacher and Ram Seshadri. *MRS Bull.* 34.8 (2009) 561–568.
- [48] A. Dursun, D. V. Pugh, and S. G. Corcoran. *J. Electrochem. Soc.* 150.7 (2003) B355–B360.
- [49] Aziz Dursun, Dylan V. Pugh, and Sean G. Corcoran. *Electrochem. Solid-State Lett.* 6.8 (2003) B32–B34.

-
- [50] Aziz Dursun, Dylan V. Pugh, and Sean G. Corcoran. *J. Electrochem. Soc.* 152.2 (2005) B65–B72.
- [51] G. Tammann. *Z. Anorg. Allg. Chem.* 107.1 (1919) 1–239.
- [52] G. Masing. *Naturwissenschaften* 11.22 (1923) 413–422.
- [53] Lloyd W. Covert and Homer Adkins. *J. Am. Chem. Soc.* 54.10 (1932) 4116–4117.
- [54] E. Ivanov et al. *Mat. Lett.* 7.1 (1988) 51–54.
- [55] Heather Lechtman. *Sci. Am.* 250.6 (1984) 56–63.
- [56] H. W. Pickering and P. R. Swann. *CORROSION* 19.11 (1963) 373t–389t.
- [57] H. W. Pickering. *Corros. Sci.* 23.10 (1983) 1107–1120.
- [58] A. J. Forty and P. Durkin. *Philos. Mag. A* 42.3 (1980) 295–318.
- [59] Caixia Xu, Xiaohong Xu, Jixin Su, and Yi Ding. *J. Catal.* 252.2 (2007) 243–248.
- [60] Masatake Haruta. *Chem. Phys. Chem.* 8.13 (2007) 1911–1913.
- [61] Caixia Xu et al. *J. Am. Chem. Soc.* 129.1 (2007) 42–43.
- [62] J. Biener et al. *Nat. Mater.* 8.1 (2009) 47–51.
- [63] Lyudmila V. Moskaleva et al. *Phys. Chem. Chem. Phys.* 13.10 (2011) 4529–4539.
- [64] Kathryn M. Kosuda, Arne Wittstock, Cynthia M. Friend, and Marcus Bäumer. *Angew. Chem. Int. Ed.* 51.7 (2012) 1698–1701.
- [65] Michelle L. Personick et al. *ACS Catal.* 5.7 (2015) 4237–4241.
- [66] Günther Reuss, Walter Disteldorf, Armin Otto Gamer, and Albrecht Hilt. *Ullmann’s Encyclopedia of Industrial Chemistry*. Wiley-VCH Verlag GmbH & Co. KGaA, 2000.
- [67] Werner Reutemann and Heinz Kieczka. *Ullmann’s Encyclopedia of Industrial Chemistry*. Wiley-VCH Verlag GmbH & Co. KGaA, 2000.
- [68] N. Lopez et al. *J. Catal.* 223.1 (2004) 232–235.
- [69] Anastasia Lackmann et al. *J. Catal.* 353.Supplement C (2017) 99–106.
- [70] L. M. Molina and B. Hammer. *Phys. Rev. B* 69.15 (2004) 155424.
- [71] Ton V. W. Janssens et al. *Top. Catal.* 44.1 (2007) 15.

- [72] Hanne Falsig et al. *Angew. Chem. Int. Ed.* 47.26 (2008) 4835–4839.
- [73] Jooho Kim, Enrique Samano, and Bruce E. Koel. *Surf. Sci.* 600.19 (2006) 4622–4632.
- [74] Thierry Déronzier, Franck Morfin, Laurence Massin, Marc Lomello, and Jean-Luc Rousset. *Chem. Mater.* 23.24 (2011) 5287–5289.
- [75] Balaram S. Takale et al. *J. Am. Chem. Soc.* 138.32 (2016) 10356–10364.
- [76] Lu-Cun Wang et al. *J. Catal.* 344 (2016) 778–783.
- [77] Christoph Mahr et al. *J. Catal.* 352 (2017) 52–58.
- [78] Tobias Krekeler et al. *Mater. Res. Lett.* 5.5 (2017) 314–321.
- [79] Branko Zugic et al. *Nat. Mater.* 16.5 (2017) 558–564.
- [80] Jose L. C. Fajin, M. Natalia D. S. Cordeiro, and Jose R. B. Gomes. *Chem. Commun.* 47.29 (2011) 8403–8405.
- [81] Sandra Hoppe and Lyudmila V. Moskaleva. *Noble and Precious Metals*. Ed. by Mohindar Singh Seehra and Alan D. Bristow. Rijeka: In-techOpen, 2018.
- [82] Yong Li et al. *J. Phys. Chem. C* (2017).
- [83] Matthew M. Montemore, Robert J. Madix, and Efthimios Kaxiras. *J. Phys. Chem. C* 120.30 (2016) 16636–16640.
- [84] Wilke Dononelli and Thorsten Klüner. *Faraday Discussions* 208.0 (2018) 105–121.
- [85] Gabriele Tomaschun et al. *J. Catal.* 364 (2018) 216–227.
- [86] Peter A. Dowben and Allen Miller, eds. Boca Raton, Fla.: CRC Press, 1990.
- [87] Micha Polak. *J. Phys.: Condens. Matter* 28.6 (2016) 060301.
- [88] R. A. van Santen and W.M.H. Sachtler. *J. Catal.* 33.2 (1974) 202–209.
- [89] Frank L. Williams and D. Nason. *Surf. Sci.* 45.2 (1974) 377–408.
- [90] J. J. Burton, E. Hyman, and D. G. Fedak. *J. Catal.* 37.1 (1975) 106–113.
- [91] S. H. Overbury, P. A. Bertrand, and G. A. Somorjai. *Chem. Rev.* 75.5 (1975) 547–560.

-
- [92] C. A. Balseiro and J. L. Morán-López. *Phys. Rev. B* 21.2 (1980) 349–354.
- [93] J. Willard Gibbs. New York: Longmans, Green, 1928.
- [94] Peter A. Dowben, Allen H. Miller, and Richard W. Vook. *Gold Bull.* 20.3 (1987) 54–65.
- [95] P. Wynblatt and R. C. Ku. *Surf. Sci.* 65.2 (1977) 511–531.
- [96] Farid F. Abraham, Tsai Nan-Hsiung, and G. M. Pound. *Surf. Sci.* 83.2 (1979) 406–422.
- [97] Werner Martienssen and Hans Warlimont. Springer Science & Business Media, 2006.
- [98] Charles Kittel. 8. ed. Hoboken, NJ: Wiley, 2005.
- [99] S.H Overbury and G.A Somorjai. *Surf. Sci.* 55.1 (1976) 209–226.
- [100] Masao Yabumoto, Kuniaki Watanabe, and Toshiro Yamashina. *Surf. Sci.* 77.3 (1978) 615–625.
- [101] R. Bouwman, L.H Toneman, M.A.M Boersma, and R.A van Santen. *Surf. Sci.* 59.1 (1976) 72–82.
- [102] S. C. Fain and J. M. McDavid. *Phys. Rev. B* 9.12 (1974) 5099–5107.
- [103] G. A. Somorjai and S. H. Overbury. *Faraday Discuss. Chem. Soc.* 60 (1975) 279.
- [104] G.C Nelson. *Surf. Sci.* 59.1 (1976) 310–314.
- [105] M. J. Kelley, D. G. Swartzfager, and V. S. Sundaram. *J. Vac. Sci. Technol.* 16.2 (1979) 664–667.
- [106] T. S. King and R. G. Donnelly. *Surf. Sci.* 151.2 (1985) 374–399.
- [107] K. Meinel, M. Klaua, and H. Bethge. *Phys. Stat. Sol. a* 106.1 (1988) 133–144.
- [108] G. N. Derry and R. Wan. *Surf. Sci.* 566-568 (2004) 862–868.
- [109] Guillermo Bozzolo, Jorge E. Garcés, and Gregory N. Derry. *Surf. Sci.* 601.9 (2007) 2038–2046.
- [110] Daojian Cheng, Xin Liu, Dapeng Cao, Wenchuan Wang, and Shiping Huang. *Nanotechnol.* 18.47 (2007) 475702.

-
- [111] B. C. Curley, G. Rossi, R. Ferrando, and R. L. Johnston. *Eur. Phys. J. D* 43.1-3 (2007) 53–56.
- [112] Lei Deng, Wangyu Hu, Huiqiu Deng, Shifang Xiao, and Jianfeng Tang. *J. Phys. Chem. C* 115.23 (2011) 11355–11363.
- [113] Lauro Oliver Paz-Borbón, Roy L. Johnston, Giovanni Barcaro, and Alessandro Fortunelli. *J. Chem. Phys.* 128.13 (2008) 134517.
- [114] Arezoo Dianat et al. *Surf. Sci.* 602.4 (2008) 876–884.
- [115] R. F. W. Bader. Reprinted. Vol. 22. The International series of monographs on chemistry. Oxford [England]: Clarendon Press, 2003, cop. 1990.
- [116] Graeme Henkelman, Andri Arnaldsson, and Hannes Jónsson. *Comput. Mater. Sci.* 36.3 (2006) 354–360.
- [117] Edward Sanville, Steven D. Kenny, Roger Smith, and Graeme Henkelman. *J. Comput. Chem.* 28.5 (2007) 899–908.
- [118] W. Tang, E. Sanville, and G. Henkelman. *J. Phys.: Condens. Matter* 21.8 (2009) 084204.
- [119] J. Friedel. *Ann. Phys.* 1 (1976) 257–307.
- [120] Erwin Schrödinger. *Ann. Phys.* 384.6 (1926) 489–527.
- [121] Werner Heisenberg. S. Hirzel Leipzig, 1930.
- [122] M. Born and R. Oppenheimer. *Ann. Phys.* 389.20 (1927) 457–484.
- [123] D. S. Sholl and J. A. Steckel. Hoboken, NJ, USA: John Wiley & Sons, Inc, 2009.
- [124] Wolfram Koch and Max C. Holthausen. Weinheim, FRG: WILEY-VCH Verlag GmbH, 2001.
- [125] Takao Tsuneda. Tokyo: Springer Japan, 2014.
- [126] L. H. Thomas. *Math. Proc. Camb. Philos. Soc.* 23.5 (1927) 542–548.
- [127] E. Fermi. *Zeitschrift für Physik* 48.1 (1928) 73–79.
- [128] W. Kohn. *Rev. Mod. Phys.* 71.5 (1999) 1253–1266.
- [129] D. R. Hartree. *Math. Proc. Camb. Philos. Soc.* 24.1 (1928) 89–110.
- [130] V. Fock. *Zeitschrift für Physik* 61.1 (1930) 126–148.
- [131] J. C. Slater. *Phys. Rev.* 35.2 (1930) 210–211.

- [132] Per-Olov Löwdin. *Phys. Rev.* 97.6 (1955) 1509–1520.
- [133] R. O. Jones. *Computational Nanoscience: Do It Yourself* 31 (2006) 45–70.
- [134] Lars Hedin and Bengt I. Lundqvist. *J. Phys. C.: Solid State Phys.* 4.14 (1971) 2064.
- [135] D. M. Ceperley and B. J. Alder. *Phys. Rev. Lett.* 45.7 (1980) 566–569.
- [136] J. P. Perdew, E. R. McMullen, and Alex Zunger. *Phys. Rev. A* 23.6 (1981) 2785–2789.
- [137] N. M. Harrison. *Nato Science Series Sub Series III Computer And Systems Sciences* 187 (2003) 45–70.
- [138] Matthias Ernzerhof, John P. Perdew, and Kieron Burke. *Int. J. Quantum Chem.* 64.3 (1998) 285–295.
- [139] John P. Perdew and Yue Wang. *Phys. Rev. B* 45.23 (1992) 13244–13249.
- [140] John P. Perdew, Kieron Burke, and Yue Wang. *Phys. Rev. B* 54.23 (1996) 16533–16539.
- [141] John P. Perdew, Kieron Burke, and Matthias Ernzerhof. *Phys. Rev. Lett.* 77.18 (1996) 3865–3868.
- [142] Jianmin Tao, John P. Perdew, Viktor N. Staroverov, and Gustavo E. Scuseria. *Phys. Rev. Lett.* 91.14 (2003) 146401.
- [143] John P. Perdew, Jianmin Tao, Viktor N. Staroverov, and Gustavo E. Scuseria. *J. Chem. Phys.* 120.15 (2004) 6898–6911.
- [144] Axel D. Becke. *J. Chem. Phys.* 98.2 (1993) 1372–1377.
- [145] S. H. Vosko, L. Wilk, and M. Nusair. *Can. J. Phys.* 58.8 (1980) 1200–1211.
- [146] Chengteh Lee, Weitao Yang, and Robert G. Parr. *Phys. Rev. B* 37.2 (1988) 785–789.
- [147] Jochen Heyd, Gustavo E. Scuseria, and Matthias Ernzerhof. *J. Chem. Phys.* 118.18 (2003) 8207–8215.
- [148] Jochen Heyd and Gustavo E. Scuseria. *J. Chem. Phys.* 121.3 (2004) 1187–1192.

- [149] John P. Perdew and Karla Schmidt. *AIP Conference Proceedings* 577.1 (2001) 1–20.
- [150] D. J. Chadi and Marvin L. Cohen. *Phys. Rev. B* 8.12 (1973) 5747–5753.
- [151] Hendrik J. Monkhorst and James D. Pack. *Phys. Rev. B* 13.12 (1976) 5188–5192.
- [152] David Vanderbilt. *Phys. Rev. B* 41.11 (1990) 7892–7895.
- [153] M. C. Payne, M. P. Teter, D. C. Allan, T. A. Arias, and J. D. Joannopoulos. *Rev. Mod. Phys.* 64.4 (1992) 1045–1097.
- [154] P. E. Blöchl. *Phys. Rev. B* 50.24 (1994) 17953–17979.
- [155] G. Kresse and D. Joubert. *Phys. Rev. B* 59.3 (1999) 1758–1775.
- [156] H. Hellmann. Leipzig: Franz Denticke, 1937.
- [157] R. P. Feynman. *Phys. Rev.* 56.4 (1939) 340–343.
- [158] Jörg Neugebauer and Matthias Scheffler. *Phys. Rev. B* 46.24 (1992) 16067–16080.
- [159] G. Makov and M. C. Payne. *Phys. Rev. B* 51.7 (1995) 4014–4022.
- [160] Stefan Müller. *J. Phys.: Condens. Matter* 15.34 (2003) R1429.
- [161] Gus L. W. Hart, Volker Blum, Michael J. Walorski, and Alex Zunger. *Nat. Mater.* 4 (2005) 391–394.
- [162] Murray S. Daw and M. I. Baskes. *Phys. Rev. Lett.* 50.17 (1983) 1285–1288.
- [163] Murray S. Daw, Stephen M. Foiles, and Michael I. Baskes. *Mater. Sci. Rep.* 9.7 (1993) 251–310.
- [164] G. Tréglia et al. *Comput. Mater. Sci.* 15.2 (1999) 196–235.
- [165] V. Drchal, A. Pasturel, R. Monnier, J. Kudrnovský, and P. Weinberger. *Comput. Mater. Sci.* 15.2 (1999) 144–168.
- [166] A. V. Ruban and H. L. Skriver. *Comput. Mater. Sci.* 15.2 (1999) 119–143.
- [167] M. Lundberg. *Phys. Rev. B* 36.9 (1987) 4692–4699.
- [168] S. Müller, M. Stöhr, and O. Wieckhorst. *Appl. Phys. A* 82.3 (2006) 415–419.

- [169] Ryoichi Kikuchi. *Phys. Rev.* 81.6 (1951) 988–1003.
- [170] R. Kikuchi and K. Masuda-Jindo. *Calphad* 26.1 (2002) 33–54.
- [171] J. W. D. Connolly and A. R. Williams. *Phys. Rev. B* 27.8 (1983) 5169–5172.
- [172] J. M. Sanchez, F. Ducastelle, and D. Gratias. *Physica A* 128.1-2 (1984) 334–350.
- [173] J. M. Sanchez. *Phys. Rev. B* 81.22 (2010) 224202.
- [174] Ernst Ising. *Zeitschrift für Physik* 31.1 (1925) 253–258.
- [175] D. Lerch, O. Wieckhorst, G. L. W. Hart, R. W. Forcade, and S. Müller. *Modell. Simul. Mater. Sci. Eng.* 17.5 (2009) 055003.
- [176] Barbara Knöbl. Diplomarbeit. Wien: Universität Wien, 2012.
- [177] Emmanuel J. Candès, Justin Romberg, and Terence Tao. *IEEE Transactions on information theory* 52.2 (2006) 489–509.
- [178] Emmanuel J. Candès and Michael B. Wakin. *IEEE signal processing magazine* 25.2 (2008) 21–30.
- [179] Zbigniew Michalewicz and David B. Fogel. Springer Science & Business Media, 2013.
- [180] Charles Darwin. *London: Murray* 247 (1859) 1859.
- [181] Volker Blum, Gus L. W. Hart, Michael J. Walorski, and Alex Zunger. *Phys. Rev. B* 72.16 (2005) 165113.
- [182] Stefan Müller. *Multiscale Simulation Methods in Molecular Science* (2009).
- [183] Tobias C. Kerscher, Wolfgang Landgraf, Raimund Podlousky, and Stefan Müller. *Phys. Rev. B* 86.19 (2012) 195420.
- [184] Sascha B. Maisel, Michaela Höfler, and Stefan Müller. 491 (2012) 740 EP –.
- [185] M. Stone. *J. R. Stat. Soc. Series B* 36.2 (1974) 111–147.
- [186] Knut Baumann. *Trends Anal. Chem.* 22.6 (2003) 395–406.
- [187] Gus L. W. Hart and Rodney W. Forcade. *Phys. Rev. B* 77.22 (2008) 224115.

- [188] Gus L. W. Hart and Rodney W. Forcade. *Phys. Rev. B* 80.1 (2009) 014120.
- [189] Gus L.W. Hart, Lance J. Nelson, and Rodney W. Forcade. *Comput. Mater. Sci.* 59.Supplement C (2012) 101–107.
- [190] D. Reith, M. Stöhr, R. Podloucky, T. C. Kerscher, and S. Müller. *Phys. Rev. B* 86.2 (2012) 020201.
- [191] Nicholas Metropolis, Arianna W. Rosenbluth, Marshall N. Rosenbluth, Augusta H. Teller, and Edward Teller. *J. Chem. Phys.* 21.6 (1953) 1087–1092.
- [192] Tobias C. Kerscher, Stefan Müller, Quinn O. Snell, and Gus L.W. Hart. *IEEE International Parallel & Distributed Processing Symposium (IPDPS), 2011*. Piscataway, NJ: IEEE, 2011 1234–1241.
- [193] P. J. Rous. *Prog. Surf. Sci.* 39.1 (1992) 3–63.
- [194] K. Heinz, R. Döll, and M. Kottcke. *Surf. Rev. Lett.* 03.05n06 (1996) 1651–1661.
- [195] K. Heinz. *Surface and Interface Science, Volume 1*. Ed. by K. Wandelt. Berlin: Wiley–VCH Verlag GmbH & Co. KGaA, 2014 93–150.
- [196] C. Davisson and L. H. Germer. 119 (1927) 558.
- [197] G. P. Thomson and A. Reid. 119 (1927) 890.
- [198] J. B. Pendry. *J. Phys. C.: Solid State Phys.* 13.5 (1980) 937.
- [199] Pascal Ferstl et al. *Phys. Rev. Lett.* 117.4 (2016) 046101.
- [200] P. Ferstl et al. *Phys. Rev. B* 93.23 (2016) 235406.
- [201] T. Kißlinger, P. Ferstl, M. A. Schneider, and L. Hammer. *J. Phys.: Condens. Matter* 29.36 (2017) 365001.
- [202] P. J. Rous et al. *Phys. Rev. Lett.* 57.23 (1986) 2951–2954.
- [203] U. Löffler, R. Döll, K. Heinz, and J. B. Pendry. *Surf. Sci.* 301.1 (1994) 346–352.
- [204] R. Döll, M. Kottcke, and K. Heinz. *Phys. Rev. B* 48.3 (1993) 1973–1976.
- [205] V. Blum and K. Heinz. *Comput. Phys. Commun.* 134.3 (2001) 392–425.

- [206] M. Kottcke and K. Heinz. *Surf. Sci.* 376.1 (1997) 352–366.
- [207] Taku Tsuchiya and Katsuyuki Kawamura. *J. Chem. Phys.* 116.5 (2002) 2121–2124.
- [208] In-Kook Suh, H. Ohta, and Y. Waseda. *J. Mater. Sci.* 23.2 (1988) 757–760.
- [209] Stefan Grimme, Jens Antony, Stephan Ehrlich, and Helge Krieg. *J. Chem. Phys.* 132.15 (2010) 154104.
- [210] Werner Reckien, Florian Janetzko, Michael F. Peintinger, and Thomas Bredow. *J. Comput. Chem.* 33.25 (2012) 2023–2031.
- [211] N. Norman and B. E. Warren. *J. Appl. Phys.* 22.4 (1951) 483–486.
- [212] B. Schönfeld, J. Traube, and G. Kostorz. *Phys. Rev. B* 45.2 (1992) 613–621.
- [213] Z. W. Lu, B. M. Klein, and A. Zunger. *J. Phase Equilib.* 16.1 (1995) 36–45.
- [214] V. Ozoliņš, C. Wolverton, and Alex Zunger. *Phys. Rev. B* 57.11 (1998) 6427–6443.
- [215] Q. Jiang, H. M. Lu, and M. Zhao. *J. Phys.: Condens. Matter* 16.4 (2004) 521.
- [216] Ch. Wöll, S. Chiang, R. J. Wilson, and P. H. Lippel. *Phys. Rev. B* 39.11 (1989) 7988–7991.
- [217] Noboru Takeuchi, C. T. Chan, and K. M. Ho. *Phys. Rev. B* 43.17 (1991) 13899–13906.
- [218] R.J Nichols, T. Nouar, C.A Lucas, W. Haiss, and W.A Hofer. *Surf. Sci.* 513.2 (2002) 263–271.
- [219] Ari Paavo Seitsonen. *Surf. Sci.* 643 (2016) 150–155.
- [220] M. Smetanin et al. *Langmuir* 24.16 (2008) 8561–8567.
- [221] M. Smetanin, D. Kramer, S. Mohanan, U. Herr, and J. Weissmüller. *Phys. Chem. Chem. Phys.* 11.40 (2009) 9008–9012.
- [222] Jian-Min Zhang, Fei Ma, and Ke-Wei Xu. *Appl. Surf. Sci.* 229.1-4 (2004) 34–42.
- [223] H. L. Skriver and N. M. Rosengaard. *Phys. Rev. B* 46.11 (1992) 7157–7168.

- [224] L. Vitos, A. V. Ruban, H. L. Skriver, and J. Kollár. *Surf. Sci.* 411.1-2 (1998) 186–202.
- [225] J.-M. Albina, C. Elsässer, J. Weissmüller, P. Gumbsch, and Y. Umeno. *Phys. Rev. B* 85.12 (2012) 959.
- [226] Nicholas E. Singh-Miller and Nicola Marzari. *Phys. Rev. B* 80.23 (2009) 235407.
- [227] W. R. Tyson and W. A. Miller. *Surf. Sci.* 62.1 (1977) 267–276.
- [228] J. Rehr, E. Zaremba, and W. Kohn. *Phys. Rev. B* 12 (1975).
- [229] Li Guan et al. *Solid State Commun.* 149.37 (2009) 1561–1564.
- [230] V. Zólyomi, L. Vitos, S. K. Kwon, and J. Kollár. *J. Phys.: Condens. Matter* 21.9 (2009) 095007.
- [231] V.A Lubarda. *Mech. Mater.* 35.1 (2003) 53–68.
- [232] S. Hoppe and S. Müller. *J. Appl. Phys.* 122 (2017) 235303.
- [233] Neil Bartlett. *Gold Bull.* 31.1 (1998) 22–25.
- [234] Lai-Sheng Wang. *Phys. Chem. Chem. Phys.* 12.31 (2010) 8694–8705.
- [235] D. Tománek, S. Mukherjee, V. Kumar, and K. H. Bennemann. *Surf. Sci.* 114.1 (1982) 11–22.
- [236] G. A. Somorjai and M. A. van Hove. *Prog. Surf. Sci.* 30.3 (1989) 201–231.
- [237] B. C. Han, A. van der Ven, G. Ceder, and Bing-Joe Hwang. *Phys. Rev. B* 72.20 (2005) 205409.
- [238] Carl A. Menning and Jingguang G. Chen. *J. Chem. Phys.* 130.17 (2009) 174709.
- [239] M. Mavrikakis, P. Stoltze, and J. K. Nørskov. *Catal. Lett.* 64.2 (2000) 101–106.
- [240] Hongqing Shi and Catherine Stampfl. *Phys. Rev. B* 76.7 (2007) 27.
- [241] T. A. Baker, B. Xu, X. Liu, E. Kaxiras, and C. M. Friend. *J. Phys. Chem. C* 113.38 (2009) 16561–16564.
- [242] Ana M. Pessoa, José L.C. Fajín, José R.B. Gomes, and M. Natália D.S. Cordeiro. *Surf. Sci.* 606.1 (2012) 69–77.

- [243] Yohaselly Santiago-Rodríguez, Jeffrey A. Herron, María C. Curet-Arana, and Manos Mavrikakis. *Surf. Sci.* 627 (2014) 57–69.
- [244] N. Saliba, D.H Parker, and B.E Koel. *Surf. Sci.* 410.2 (1998) 270–282.
- [245] Silvia González, Konstantin M. Neyman, Shamil Shaikhutdinov, Hans-Joachim Freund, and Francesc Illas. *J. Phys. Chem. C* 111.18 (2007) 6852–6856.
- [246] Feng Tao et al. *Science* 322.5903 (2008) 932–934.
- [247] P. Welker, O. Wieckhorst, T. C. Kerscher, and S. Müller. *J. Phys.: Condens. Matter* 22.38 (2010) 384203.
- [248] J. Chevrier, L. Huang, P. Zeppenfeld, and G. Comsa. *Surf. Sci.* 355.1-3 (1996) 1–12.
- [249] J.M Gottfried, N. Elghobashi, S.L.M Schroeder, and K. Christmann. *Surf. Sci.* 523.1-2 (2003) 89–102.
- [250] Volkmar Zielasek, Bingjun Xu, Xiaoying Liu, Marcus Bäumer, and Cynthia M. Friend. *J. Phys. Chem. C* 113.20 (2009) 8924–8929.
- [251] A. E. Baber et al. *J. Phys. Chem. C* 116.34 (2012) 18292–18299.
- [252] Alexander Yu. Klyushin, Tulio C. R. Rocha, Michael Hävecker, Axel Knop-Gericke, and Robert Schlögl. *Phys. Chem. Chem. Phys.* 16.17 (2014) 7881–7886.
- [253] F. Hiebel, M. M. Montemore, E. Kaxiras, and C. M. Friend. *Surf. Sci.* 650 (2016) 5–10.
- [254] Lyudmila V. Moskaleva, Volkmar Zielasek, Thorsten Klüner, Konstantin M. Neyman, and Marcus Bäumer. *Chem. Phys. Lett.* 525-526 (2012) 87–91.
- [255] José L. C. Fajín, M. Natália D. S. Cordeiro, and José R. B. Gomes. *J. Phys. Chem. C* 111.46 (2007) 17311–17321.
- [256] José L.C. Fajín, M. Natália D.S. Cordeiro, and José R.B. Gomes. *Surf. Sci.* 602.2 (2008) 424–435.
- [257] M. Landmann, E. Rauls, and W. G. Schmidt. *J. Phys. Chem. C* 113.14 (2009) 5690–5699.
- [258] Sandra Hoppe, Yong Li, Lyudmila V. Moskaleva, and Stefan Müller. *Phys. Chem. Chem. Phys.* 19.22 (2017) 14845–14853.

- [259] Sergey M. Kozlov, Gábor Kovács, Riccardo Ferrando, and Konstantin M. Neyman. *Chem. Sci.* 6.7 (2015) 3868–3880.
- [260] Lyudmila V. Moskaleva, Theodor Weiss, Thorsten Klüner, and Marcus Bäumer. *J. Phys. Chem. C* 119.17 (2015) 9215–9226.
- [261] A. D. Becke and K. E. Edgecombe. *J. Chem. Phys.* 92.9 (1990) 5397–5403.
- [262] Richard Dronskowski and Peter E. Bloechl. *J. Phys. Chem.* 97.33 (1993) 8617–8624.
- [263] Volker L. Deringer, Andrei L. Tchougréeff, and Richard Dronskowski. *J. Phys. Chem. A* 115.21 (2011) 5461–5466.
- [264] Stefan Maintz, Volker L. Deringer, Andrei L. Tchougréeff, and Richard Dronskowski. *J. Comput. Chem.* 34.29 (2013) 2557–2567.
- [265] Stefan Maintz, Volker L. Deringer, Andrei L. Tchougréeff, and Richard Dronskowski. *J. Comput. Chem.* 37.11 (2016) 1030–1035.
- [266] S. Maintz, M. Esser, and Richard Dronskowski. *Acta Phys. Pol. B* 47 (2016).
- [267] J. Weissmüller et al. *Science* 300.5617 (2003) 312.
- [268] Florian Weigend, Ferdinand Evers, and Jörg Weissmüller. *Small* 2.12 (2006) 1497–1503.
- [269] Hai-Jun Jin et al. *Nano Lett.* 10.1 (2010) 187–194.
- [270] Eric Detsi, Marc Sànchez Sellès, Patrick R. Onck, and Jeff Th. M. de Hosson. *Scr. Mater.* 69.2 (2013) 195–198.
- [271] Chuan Cheng and Alfonso H. W. Ngan. *ACS Nano* 9.4 (2015) 3984–3995.
- [272] Wolfgang Haiss, Richard J. Nichols, Jürgen K. Sass, and Klaus P. Charle. *J. Electroanal. Chem.* 452.2 (1998) 199–202.
- [273] R. N. Viswanath, D. Kramer, and J. Weissmüller. *Langmuir* 21.10 (2005) 4604–4609.
- [274] J. Weissmüller, R. N. Viswanath, L. A. Kibler, and D. M. Kolb. *Phys. Chem. Chem. Phys.* 13.6 (2011) 2114–2117.
- [275] Y. Umeno et al. *Europhys. Lett.* 78.1 (2007) 13001.
- [276] N. D. Lang and W. Kohn. *Physical Review B* 3.4 (1971) 1215–1223.

- [277] Sergio Trasatti. *J. Electroanal. Chem. Interfacial. Electrochem.* 33.2 (1971) 351–378.
- [278] D. L. Rath and D. M. Kolb. *Surf. Sci.* 109.3 (1981) 641–647.
- [279] V. V. Levitin, S. V. Loskutov, M. I. Pravda, and B. A. Serpetzky. *Solid State Commun.* 92.12 (1994) 973–976.
- [280] V.V Levitin, O.L Garin, V.K Yatsenko, and S.V Loskutov. *Vacuum* 63.1 (2001) 367–370.
- [281] Wen Li, Y. Wang, and D. Y. Li. *Phys. Stat. Sol. a* 201.9 (2004) 2005–2012.
- [282] D. Sekiba et al. *Phys. Rev. B* 75.11 (2007) 860.
- [283] X. F. Wang, W. Li, J. G. Lin, and Y. Xiao. *Europhys. Lett.* 89.6 (2010) 66004.
- [284] R. Smoluchowski. *Phys. Rev.* 60.9 (1941) 661–674.
- [285] M. Mavrikakis, B. Hammer, and J. K. Nørskov. *Phys. Rev. Lett.* 81.13 (1998) 2819–2822.
- [286] Ludwig A. Kibler, Ahmed M. El-Aziz, Rüdiger Hoyer, and Dieter M. Kolb. *Angew. Chem. Int. Ed.* 44.14 (2005) 2080–2084.
- [287] Charlotte Stenner, Li-Hua Shao, Nadiia Mameka, and Jörg Weissmüller. *Adv. Funct. Mater.* 26.28 (2016) 5174–5181.
- [288] J. Weissmüller, H.-L. Duan, and D. Farkas. *Acta Mater.* 58.1 (2010) 1–13.
- [289] Christoph Mahr et al. *Mater. Res. Lett.* 6.1 (2018) 84–92.
- [290] Marc Winter, ed.
- [291] D. Faurie et al. *Acta Mater.* 58.15 (2010) 4998–5008.
- [292] Marc Winter, ed.
- [293] C. J. Fall, N. Binggeli, and A. Baldereschi. *J. Phys.: Condens. Matter* 11.13 (1999) 2689.
- [294] Lin-Lin Wang and Hai-Ping Cheng. *Phys. Rev. B* 69.16 (2004) 165417.
- [295] M. Chelvayohan and C. H. B. Mee. *J. Phys. C: Solid State Phys.* 15.10 (1982) 2305.

- [296] G. V. Hansson and S. A. Flodström. *Phys. Rev. B* 18.4 (1978) 1572–1585.
- [297] A. Michl, J. Weissmüller, and S. Müller. *J. Phys.: Condens. Matter* 25.44 (2013) 445012.

Curriculum vitae

Nachname	Hoppe
Vorname	Sandra
Staatsangehörigkeit	deutsch
Geburtsdatum	16.07.1987
Geburtsort	Höxter
08/1994 - 07/1997	Grundschule, Kreiensen
08/1997 - 07/1999	Orientierungsstufe, Haupt- und Realschule Kreiensen
09/1999 - 07/2006	Roswitha-Gymnasium, Bad Gandersheim Abschluss: Abitur
10/2006 - 07/2010	Bachelorstudium <i>General Engineering Science</i> Technische Universität Hamburg Abschluss: Bachelor of Science
10/2010 - 12/2012	Masterstudium <i>Joint European Master in Materials Science</i> Technische Universität Hamburg Abschluss: Master of Science
01/2013 - 12/2018	Wissenschaftliche Mitarbeiterin Institut für Keramische Hochleistungswerkstoffe Technische Universität Hamburg
seit 05/2019	Koordinatorin des SFB 986 Institut für Keramische Hochleistungswerkstoffe Technische Universität Hamburg

27. Juli 2020